

**Geology and Genesis of Hybridized Ultramafic Rocks in the
Black Label Hybrid Zone of the Black Thor Intrusive Complex,
McFaulds Lake Greenstone Belt, Ontario, Canada**

by

Charles S. Spath III

Thesis submitted in partial fulfillment
of the requirements for the degree of
Master of Science (M.Sc.) Geology

The Faculty of Graduate Studies
Laurentian University
Sudbury, Ontario, Canada

© CS Spath 2017

THESIS DEFENCE COMMITTEE/COMITÉ DE SOUTENANCE DE THÈSE
Laurentian Université/Université Laurentienne
Faculty of Graduate Studies/Faculté des études supérieures

Title of Thesis Titre de la thèse	Geology and Genesis of Hybridized Ultramafic Rocks in the Black Label Hybrid Zone of the Black Thor Intrusive Complex, McFaulds Lake Greenstone Belt, Ontario, Canada		
Name of Candidate Nom du candidat	Spath, Charles		
Degree Diplôme	Master of Science		
Department/Program Département/Programme	Geology	Date of Defence Date de la soutenance	May 23, 2017

APPROVED/APPROUVÉ

Thesis Examiners/Examineurs de thèse:

Dr. Michael Leshner
(Co-Supervisor/Co-directeur(trice) de thèse)

Dr. Michel Houlié
(Co-Supervisor/Co-directeur(trice) de thèse)

Dr. Pedro Jugo
(Committee member/Membre du comité)

Dr. James S. Scoates
(External Examiner/Examineur externe)

Approved for the Faculty of Graduate Studies
Approuvé pour la Faculté des études supérieures
Dr. David Lesbarrères
Monsieur David Lesbarrères
Dean, Faculty of Graduate Studies
Doyen, Faculté des études supérieures

ACCESSIBILITY CLAUSE AND PERMISSION TO USE

I, **Charles Spath**, hereby grant to Laurentian University and/or its agents the non-exclusive license to archive and make accessible my thesis, dissertation, or project report in whole or in part in all forms of media, now or for the duration of my copyright ownership. I retain all other ownership rights to the copyright of the thesis, dissertation or project report. I also reserve the right to use in future works (such as articles or books) all or part of this thesis, dissertation, or project report. I further agree that permission for copying of this thesis in any manner, in whole or in part, for scholarly purposes may be granted by the professor or professors who supervised my thesis work or, in their absence, by the Head of the Department in which my thesis work was done. It is understood that any copying or publication or use of this thesis or parts thereof for financial gain shall not be allowed without my written permission. It is also understood that this copy is being made available in this form by the authority of the copyright owner solely for the purpose of private study and research and may not be copied or reproduced except as permitted by the copyright laws without written authority from the copyright owner.

Abstract

The ca. 2.7 Ga Black Thor Intrusive Complex (BTIC) is a komatiitic elongate layered intrusion composed primarily of dunite, lherzolite, olivine websterite, websterite, and chromitite overlain by lesser gabbro and anorthosite. After emplacement but before complete crystallization, a Late Websterite Intrusion (LWI) reactivated the feeder conduit and intruded the base and the core of the BTIC, including the Black Label Chromitite Zone. LWI is a discordant to semi-concordant intrusion that produced marginal zones of heterogeneous, interfingering hybrid matrix and clasts defined as the Black Label Hybrid Zone (BLHZ). The clasts range from 1 to 200 cm in size (rarely > 5m), exhibit amoeboidal to subangular shapes, with sharp to diffuse margins, and varied in compositions from dunite to lherzolite to chromitite. The nature of these clasts appear to have been controlled by the compositions of the lithologies, the thickness of layering, the nature of the contacts between layers, and the initial temperatures of the lithologies being incorporated. There are two types of hybrid groundmass: 1) hybrid harzburgite containing xenocrystic olivine within a websterite, and 2) hybrid chromite harzburgite containing xenocrystic chromite and olivine within a websterite. Both types of hybrid rocks are exceptionally well preserved in terms of mineralogy and textures. The genesis of the BLHZ is extremely complex and involved five interdependent assimilative processes: (1) mechanical disaggregation of clasts resulting in dispersal of xenocrysts; (2) grain-boundary melting (clinopyroxene + plagioclase) resulting in selective assimilation via partial melt mixing; (3) mineral-reaction relation resulting in the dissolution of high-Mg olivine xenocrysts and subsequent growth of intermediate-Mg hybrid orthopyroxene; (4) Mineral-melt re-equilibration between entrained chromite and olivine xenocrysts in LWI melt resulting in diffusive chemical exchange; and (5) complete dissolution of xenocrystic phases very locally formed clast-free rocks of intermediate composition. From map- and core-scale cross-cutting relationships a

possible emplacement model can be made: 1) initial emplacement of the BTIC and primary cumulate layers; 2) LWI reactivation of the BTIC feeder, and the diking/silling, stoping and partial assimilation of BTIC wall rocks; 3) formation of heterolithic breccias, heterogeneously hybridized rocks (BLHZ), and associated sulfide mineralization; and 4) local late stage fractional crystallization of LWI magma. The intrusion of LWI magma into the BLCZ does not appear to have consumed any of the chromitite, but has locally reduced the grade of the mineralization through dilution and dispersal. Low-grade patchy disseminated to net-textured Fe-Ni-Cu-(PGE) sulfide mineralization locally occurs in clast-rich regions of the BLHZ and appears to have been generated during the hybridization process. This is the first occurrence known to us where mixing of a magma and cognate xenoliths has led to the formation magmatic sulfides. This style of mineralization is relatively restricted within the BTIC but is consistent with the limited solubility of S in mafic-ultramafic magmas and the small amounts of magma involved.

Acknowledgements

I would like to thank C.M. Leshar for his personal support and understanding, as well as for his scientific input and mentorship. I am very grateful to M.G. Houlé for his many discerning conversations and general guidance; Richard Fink, Andrew Mitchell, and Michael Orobona (Cliffs); Alan Coutts (Noront); Jack Parker (OGS); and Mike Villeneuve (GSC) for supporting the project. I am also very grateful to Ryan Weston (Cliffs/Noront) and David Shinkle (Cliffs) for helpful discussions on the geology; Rick Kruse (Cliffs) for GIS assistance; Daron Slaney, Randy Abraham, and the rest of the Cliffs “Escher Camp” crew for logistical support; and Riku Metsaranta (OGS) and Valérie Bécu (GSC) for reviews of interim reports. Additionally, I would like to thank my close colleagues and fellow graduate students Heather Carson, Naghmeh Farhangi, and Kaveh Mehrmanesh for their thoughtful dialogue and collaboration. This project was supported by grants from Cliffs Natural Resources Inc., Noront Resources Ltd. and the Natural Sciences and Engineering Research Council of Canada Collaborative Research and Development program to C.M. Leshar, and a Society of Economic Geologists Fellowship and an Ontario Graduate Scholarship to the author. Cliffs Natural Resources Inc. provided field and logistical support; and the Ontario Geological Survey and Geological Survey of Canada through the Targeted Geosciences Initiative program provided analytical support.

This thesis is devoted to my loving parents, Charlie and Susan, my grandparents Ron, Fran and Jeanne, and my much-missed, late grandfather ‘Chick’. By no means would this work have been possible without their unquestioning console.

Contents

Abstract	iii
Acknowledgments	v
Table of Contents.....	vi
List of Figures, Tables and Appendices.....	vii
1.0 CHAPTER 1: Introduction	1
1.1 Structure of Thesis.....	3
1.2 Statement of Responsibilities	3
2.0 CHAPTER 2: Geology and Genesis of Hybridized Ultramafic Rocks in the Black Label Hybrid Zone of the Black Thor Intrusive Complex, McFaulds Lake Greenstone Belt, Ontario	
2.1 Abstract	4
2.2 Introduction.....	5
2.3 Geological Setting	7
2.3.1 Footwall Rocks.....	9
2.3.2 Black Thor Intrusive Complex	9
2.3.3 Late Websterite Intrusion	12
2.4 Analytical Methods.....	15
2.4.1 Field Work.....	15
2.4.2 Petrography	15
2.4.3 Mineral Chemistry.....	16
2.4.4 Whole Rock Geochemistry	16
2.4.5 Terminology	17
2.5 Petrography.....	18
2.5.1 Unhybridized Websterite Zone	18
2.5.2 Black Label Hybrid Zone	20
2.6 Mineral Chemistry.....	22

2.7	Whole Rock Geochemistry	23
2.7.1	Major and Compatible Trace Elements.....	24
2.7.2	Incompatible lithophile elements	26
2.7.3	Chalcophile elements	27
2.8	Discussion	28
2.8.1	Nature and origin of ultramafic clasts	28
2.8.2	Contamination/hybridization.....	30
2.8.3	Hybrid geochemistry	37
2.8.4	Sulfide mineralization and economic significance.....	37
2.8.5	Emplacement of LWI and genesis of BLHZ.....	39
2.9	Conclusions	43
2.10	Acknowledgments	46
2.11	References	46
2.12	Table Captions	51
2.13	Tables	52
2.14	Figure Captions	57
2.15	Figures	62
2.16	Appendices	88

List of tables

1.	Summary of mineralogy, petrographic textures, and alteration in Black Thor Intrusive Complex clasts within the Late Websterite Intrusion.....	52
2.	Representative electron microprobe analyses of minerals from entrained clasts, the Unhybridized Websterite Zone and Black Label Hybrid Zone	53
3.	Ranges, averages and standard deviations for whole rock geochemical analyses of selected lithologies of UWZ, BLHZ, and BTIC.....	54

List of figures

1. Geologic map of the ‘Ring of Fire’ and associated occurrences.....	62
2. Simplified geologic map of the southern ‘Ring of Fire’.....	63
3. Solid rock geologic map of the Black Thor Intrusive Complex.....	64
4. Schematic stratigraphic section through the Black Thor Intrusive Complex.....	65
5. Scans of samples from the Black Thor Intrusive Complex.....	66
6. Scans of samples from unmineralized Late Websterite Intrusion.....	67
7. Scans of samples from mineralized Black Label Hybrid Zone.....	68
8. Photographs of Black Label Hybrid Zone lithologies.....	69
9. Schematic plan view map of the Black Label Hybrid Zone.....	70
10. Lithostratigraphic columns showing late websterite and hybrid lithologies.....	71
11. Lithostratigraphic columns showing late websterite and hybrid lithologies.....	72
12. W-X-Y-Z quadrilateral plot.....	73
13. Scanned thin sections of late websterite and hybrid lithologies.....	74
14. Photomicrographs of the Late Websterite Intrusion and Black Thor Intrusive Complex...	75
15. Photomicrographs of hybrid harzburgite lithologies.....	76
16. Photomicrographs of hybrid chromite harzburgite lithologies.....	77
17. Ni vs. forsterite content of olivine and Cr ₂ O ₃ vs. MgO of chromite.....	78
18. X-Y-Z pyroxene classification diagram.....	79
19. V ₂ O ₃ -ZnO-TiO ₂ ternary plots of chromite analyses.....	80
20. Major oxides and select trace elements vs. MgO for all lithologies.....	81
21. Sulfur vs. platinum group elements for all lithologies.....	82
22. Mantle normalized extended trace element diagrams for all lithologies.....	83
23. Schematic cross-section of the brecciated Black Label Chromite Zone.....	84
24. Possible mechanisms of hybridization.....	85
25. [Th/Yb] vs. [Nb/Yb] for all lithologies.....	86
26. Possible model for emplacement of the Late Websterite Intrusion.....	87

List of appendices

A. Mineral chemistry data.....	88
B. Whole rock geochemistry data.....	93

1.0 CHAPTER 1: Introduction

Common in many intrusive complexes is the presence of several co-genetic and co-eval intrusive phases that cross-cut the primary body. This complicated process of interfingering intrusions—in different stages of their crystallization and fractionation history—result in the occurrence of xenoliths with a wide range of textures. In specific, ultramafic xenoliths occur in a range of igneous rocks and many are interpreted to have been refractory, to have not reacted to a significant degree with the magmas, and to be representative of mantle source regions (see review by Pearson et al., 2003), but some have clearly been infiltrated or assimilated by the magmas and/or reacted with magmas, modifying the compositions of the xenoliths and the magmas (e.g., Bowen, 1922; Arculus et al., 1983; Kelemen, 1986; Kelemen and Ghiorso, 1986; Pearson et al., 2003). Assimilation is favoured by magmas more mafic than xenoliths in composition (i.e., hotter magma), higher temperatures of magma and/or xenoliths, longer xenolith residence times, and lower magma viscosities; whereas non-reactive transport is favoured by small compositional contrasts, lower temperatures of magma and/or xenoliths, shorter xenolith residence times, and higher magma viscosities. The magmatic breccias in the Black Thor Intrusive Complex (BTIC), part of the ‘Ring of Fire’ Intrusive Suite (RoFIS) in the James Bay Lowlands of northern Ontario, provide an important, well-constrained example of assimilation and hybridization in a system where a number of co-eval intrusions interacted, a more evolved magma had a strong geochemical contrast with more primitive ultramafic, chromite-bearing xenoliths, and where residence times were very short (i.e., narrow temperature interval on orthopyroxene-clinopyroxene cotectic). To our knowledge, this is the first reported example of sulfide saturation being induced by incorporation of cognate, S-poor *ultramafic* xenoliths. This occurrence also highlights the fundamental problem with models involving

derivation of S by mixing more evolved and less evolved magmas or incorporation of more evolved rocks into more primitive magmas.

The general aim of this thesis is to understand the mode and mechanism of emplacement of the late websterite intrusion in the BTIC with secondary aims of: 1) characterize the hybrid rocks in the Black Label Hybrid Zone, including the cognate ultramafic wall rocks, the late intrusive magma, and the hybridized xenoliths, 2) establish the mineralogical and textural history of the refractory components of the clasts, 3) establish the petrogenesis of the Black Label Hybrid Zone, and 4) constrain the mechanism(s) of magma emplacement, hybridization, and this unique Fe-Ni-Cu-(PGE) sulfide mineralization. The results provide important constraints on little studied magma-xenolith hybridization processes in chromite-bearing, sulfide-mineralized systems.

1.1 Structure of Thesis

The contents of this thesis are in two separate chapters: Chapter 1, an introduction, description of structure and statement of responsibilities of the thesis; and Chapter 2, a manuscript to be submitted in *Economic Geology*, an internationally-circulated, peer-reviewed geoscience journal. All text, figures, tables, reference styles and electronic appendices conform to *Economic Geology* standards. Mineral and whole-rock chemical data with precision and accuracy values are provided in **Appendix A** (mineral chemistry) and **Appendix B** (whole-rock chemistry) with electronic appendices provided for the journal.

1.2 Statement of Responsibilities

The candidate was responsible for all of the research, field and analytical work, and wrote the first draft of the thesis. Fieldwork for this project was carried out during June and July 2013 at the Cliffs Natural Resources “Esker Camp” in the James Bay Lowland region of Northern Ontario. Selected intervals of 39 drill cores were re-logged and 314 samples were taken, of which 124 samples were selected for thin sectioning, 12 representative samples were selected for mineral analysis, and 75 representative samples were selected for whole-rock geochemical analysis.

Drs. C.M. Leshner and M.G. Houllé defined the scope and purpose of this thesis and provided supervision and guidance in both field and analytical work. Dr. Leshner edited several drafts of the thesis, and Dr. Houllé edited the final version of the thesis.

2.0 CHAPTER 2: Geology and Genesis of Hybridized Ultramafic Rocks in the Black Label Hybrid Zone of the Black Thor Intrusive Complex, McFaulds Lake Greenstone Belt, Ontario

C. S. Spath III¹, C.M. Leshner¹, and M.G. Houlé^{2,1}

¹ Mineral Exploration Research Centre, Harquail School of Earth Sciences and Goodman School of Mines, 935 Ramsey Lake Road, Laurentian University, Sudbury, Ontario, P3E 2C6

² Geological Survey of Canada, Lands and Minerals Sector, Natural Resources Canada, 490 rue de la Couronne, Québec, Quebec, G1K 9A9

2.1 Abstract

The ca. 2.7 Ga Black Thor Intrusive Complex (BTIC) is a komatiitic elongate layered intrusion composed primarily of dunite, lherzolite, olivine websterite, websterite, and chromitite overlain by lesser gabbro and anorthosite. After emplacement but before complete crystallization, a Late Websterite Intrusion (LWI) reactivated the feeder conduit and intruded the base and the core of the BTIC, including the Black Label Chromitite Zone. LWI is a discordant to semi-concordant intrusion that produced marginal zones of heterogeneous, interfingering hybrid matrix and clasts defined as the Black Label Hybrid Zone (BLHZ). The clasts range from 1 to 200 cm in size (rarely > 5m), exhibit amoeboidal to subangular shapes, with sharp to diffuse margins, and varied in compositions from dunite to lherzolite to chromitite. The nature of these clasts appear to have been controlled by the compositions of the lithologies, the thickness of layering, the nature of the contacts between layers, and the initial temperatures of the lithologies being incorporated. There are two types of hybrid groundmass: 1) hybrid harzburgite containing xenocrystic olivine within a websterite, and 2) hybrid chromite harzburgite containing xenocrystic chromite and olivine within a websterite. Both types of hybrid rocks are exceptionally well preserved in terms of mineralogy and textures. The genesis of the BLHZ is extremely complex and involved five interdependent assimilative processes: (1) mechanical

disaggregation of clasts resulting in dispersal of xenocrysts; (2) grain-boundary melting (clinopyroxene + plagioclase) resulting in selective assimilation via partial melt mixing; (3) mineral-reaction relation resulting in the dissolution of high-Mg olivine xenocrysts and subsequent growth of intermediate-Mg hybrid orthopyroxene; (4) Mineral-melt re-equilibration between entrained chromite and olivine xenocrysts in LWI melt resulting in diffusive chemical exchange; and (5) complete dissolution of xenocrystic phases very locally formed clast-free rocks of intermediate composition. From map- and core-scale cross-cutting relationships a possible emplacement model can be made: 1) initial emplacement of the BTIC and primary cumulate layers; 2) LWI reactivation of the BTIC feeder, and the diking/silling, stoping and partial assimilation of BTIC wall rocks; 3) formation of homo-heterolithic breccias, heterogeneously hybridized rocks (BLHZ), and associated sulfide mineralization; and 4) local late stage fractional crystallization of LWI magma. The intrusion of LWI magma into the BLCZ does not appear to have consumed any of the chromitite, but has locally reduced the grade of the mineralization through dilution and dispersal. Low-grade patchy disseminated to net-textured Fe-Ni-Cu-(PGE) sulfide mineralization locally occurs in clast-rich regions of the BLHZ and appears to have been generated during the hybridization process. This is the first occurrence known to us where mixing of a magma and cognate xenoliths has led to the formation magmatic sulfides. This style of mineralization is relatively restricted within the BTIC but is consistent with the limited solubility of S in mafic-ultramafic magmas and the small amounts of magma involved.

2.2 Introduction

Common in many intrusive complexes is the presence of several co-genetic and co-eval intrusive phases that cross-cut the primary body. This complicated process of interfingering intrusions—in different stages of their crystallization and fractionation history—result in the

occurrence of xenoliths with a wide range of textures. In specific, ultramafic xenoliths occur in a range of igneous rocks and many are interpreted to have been refractory, to have not reacted to a significant degree with the magmas, and to be representative of mantle source regions (see review by Pearson et al., 2003), but some have clearly been infiltrated or assimilated by the magmas and/or reacted with magmas, modifying the compositions of the xenoliths and the magmas (e.g., Bowen, 1922; Arculus et al., 1983; Kelemen, 1986; Kelemen and Ghiorso, 1986; Pearson et al., 2003). Assimilation is favoured by magmas more mafic than xenoliths in composition (i.e., hotter magma), higher temperatures of magma and/or xenoliths, longer xenolith residence times, and lower magma viscosities; whereas non-reactive transport is favoured by small compositional contrasts, lower temperatures of magma and/or xenoliths, shorter xenolith residence times, and higher magma viscosities. The magmatic breccias in the Black Thor Intrusive Complex (BTIC), part of the ‘Ring of Fire’ Intrusive Suite (RoFIS) in the James Bay Lowlands of northern Ontario, provide an important, well-constrained example of assimilation and hybridization in a system where a number of co-eval intrusions interacted, a more evolved magma had a strong geochemical contrast with more primitive ultramafic, chromite-bearing xenoliths, and where residence times were very short (i.e., narrow temperature interval on orthopyroxene-clinopyroxene cotectic). To our knowledge, this is the first reported example of sulfide saturation being induced by incorporation of cognate, S-poor *ultramafic* xenoliths. This occurrence also highlights the fundamental problem with models involving derivation of S by mixing more evolved and less evolved magmas or incorporation of more evolved rocks into more primitive magmas.

The general aim of this paper is to understand the mode and mechanism of emplacement of the late websterite intrusion in the BTIC with secondary aims of: 1) characterize the hybrid

rocks in the Black Label Hybrid Zone, including the cognate ultramafic wall rocks, the late intrusive magma, and the hybridized xenoliths, 2) establish the mineralogical and textural history of the refractory components of the clasts, 3) establish the petrogenesis of the Black Label Hybrid Zone, and 4) constrain the mechanism(s) of magma emplacement, hybridization, and this unique Fe-Ni-Cu-(PGE) sulfide mineralization. The results provide important constraints on little studied magma-xenolith hybridization processes in chromite-bearing, sulfide-mineralized systems.

2.3 Geological Setting

The BTIC is located within the McFaulds Lake greenstone belt (MLGB), which is a part of the WNW-ESE trending Oxford-Stull domain of the western Superior Province that stretches from western Manitoba to the James Bay Lowlands in Ontario (Rayner and Stott, 2005; Stott et al., 2010). The Oxford-Stull domain consists of juvenile oceanic crust (2.9-2.7 Ga) with platformal sequences of iron formation, arkose, and quartzite, which are interpreted to have developed along a passive margin from the input of adjacent older terranes (Stott et al., 2010). In some regions mafic to ultramafic volcanic and subvolcanic rocks have been emplaced onto/into thinned segments of the passive margin.

The McFaulds Lake greenstone belt (MLGB) occurs on the eastern limit of the Oxford-Stull domain as a >200 km long, arcuate belt that records episodic volcanism, sedimentation, and felsic-ultramafic plutonism between 2.83 and 2.66 Ga (Metsaranta et al., 2015; **Fig. 1**). Two distinct mafic-ultramafic suites have been defined by airborne magnetic and gravimetric geophysical surveys supplemented by local diamond drilling, mapping of sparse outcrops, and U-Pb geochronology (Metsaranta et al., 2015; **Fig. 2**). The magnetic surveys define a 60 km diameter arc of magnetic highs within the MLGB associated with mafic and ultramafic rocks

known colloquially as the ‘Ring of Fire’. Two discrete suites of mafic-ultramafic intrusive rocks have intruded into the supracrustal rocks of the MLGB: 1) Mesoarchean (ca. 2808 Ma) rocks of the Highbank-Fishtrap Intrusive Suite and 2) Neoproterozoic (ca. 2734 Ma) rocks of the Ring of Fire Intrusive Suite (RoFIS; Metsaranta et al., 2015; **Fig. 1**).

The RoFIS can be subdivided into two layered subsuites: 1) the Butler Lake subsuite, a volumetrically significant, mafic-dominated ‘ferrogabbro’ that is composed of gabbro and rare pyroxenite (Kuzmich et al., 2015), and 2) the Koper Lake subsuite, an economically significant ultramafic-dominated subsuite that is composed of variable amounts of dunite, peridotite, chromitite, pyroxenite, and gabbro (**Fig 1**; Carson et al., 2015). The ultramafic-dominated subsuite is up to 500m thick and semi-continuous for at least 15 km along strike, and has been dated by Metsaranta and Houlé (2017) at ca. 2734 Ma.

Two mineralization main deposit types occur within the ultramafic-dominated subsuite (**Fig. 2**): 1) world-class conduit-style magmatic Cr-(PGE) deposits (e.g., Black Thor, Black Label, Black Creek, Big Daddy, Black Horse, and Blackbird) and 2) economically significant Fe-Ni-Cu-(PGE) magmatic sulfide deposits (e.g., Eagle’s Nest). The former are up to 100m in aggregate thickness and appear to extend semi-continuously along strike for up to 10 km or more. The latter are more restricted, as the type example is the Eagle’s Nest, and occur as pipe-like bodies approximately 200 m long, up to 50 m thick, and at least 1600 m deep (Mungall et al., 2010; Zuccarelli-Pegoraro et al., 2017). Subeconomic Fe-Ti-V-(P) mineralization (e.g., Butler and Thunderbird) occurs within intrusive components of the mafic-dominated Butler Lake subsuite (Kuzmich et al., 2015), and volcanic-associated “massive” Cu-Zn-Au sulfide mineralization occurs within associated volcanic rocks (e.g., Butler and McFaulds: **Fig. 1**).

The Black Thor and Blackbird areas appear to be underlain by feeders that host the Blue Jay Ni-Cu-(PGE) occurrence and Eagle's Nest Ni-Cu-PGE deposits, respectively. The ultramafic-dominated subsuite has been informally subdivided into the Black Thor intrusive complex (containing the Black Thor, Black Label, Big Daddy and Blue Jay deposits) and Double Eagle intrusive complex (DEIC; containing the Black Horse, Blackbird and Eagle's Nest deposits) by Houlé and co-workers, although it is likely that they are both part of the same large ultramafic to mafic intrusive system (**Fig. 2**; Houlé et al., 2017).

The major lithologies in the area of the BTIC are described below, from oldest to youngest:

2.3.1 Footwall Rocks

The primary footwall lithology to the BTIC is a light grey, medium-grained, equigranular granodiorite-tonalite suite that is composed of large plagioclase phenocrysts (0.5-1.5 cm) surrounded by interstitial quartz, biotite, and minor hornblende. Equivalent rocks in the Blackbird – Eagle's Nest area have been dated at 2773.4 ± 0.9 Ma (Mungall et al., 2010). The rocks have undergone minor sericite-epidote-chlorite alteration and some contacts with the BTIC are locally sheared, but most retain primary igneous textures with grain sizes remaining constant at the contact with the BTIC, which clearly transgresses and contact metamorphoses the granodiorite-tonalite suite. Locally, the footwall granitoids contain stringers of chalcopyrite + pentlandite \pm pyrrhotite mobilized from BTIC contact mineralization.

2.3.2 Black Thor Intrusive Complex

The BTIC is a semi-conformable, layered, sill/feeder-shaped intrusion that, in its current structurally-rotated orientation, is exposed in cross section with a strike length of at least 4 km (extending as much as 10 km southwest to Blackbird), a maximum thickness of 1.3 km, and a

down-dip extent of at least 800m (**Fig. 3**). Layering in the BTIC strikes dominantly $\sim 223^\circ$ with a sub-vertical dip, and youngs to the ESE. Carson et al. (*in prep*) have shown that the BTIC can be subdivided into three main ultramafic to mafic stratigraphic series (**Fig. 4**): 1) a Basal Series, 2) an Ultramafic Series, and 3) a Mafic Series.

All rocks have been metamorphosed to lower greenschist facies, cross-cut by antigorite \pm lizardite, magnetite, magnesite, and iowaite veinlets (**Fig. 5**), shear zones, faults, felsic to mafic dikes, and two intrusions (a late websterite and biotite gabbro). Unless otherwise stated, relict igneous chromite and pyroxene are normally preserved, but olivine in these rocks has been normally replaced by serpentine \pm magnetite \pm brucite. Despite this, most rocks contain well-preserved igneous textures and the ‘meta’ prefix has been omitted for convenience and clarity.

2.3.2.1 Basal Series (BS)

The Marginal Zone of the BS is dominated by a dark-grey, medium grained ortho- to mesocumulate marginal olivine websterite and lherzolite in unconformable (transgressive, contact metamorphic) or locally sheared contact with footwall granodiorite. The Feeder Zone of the series is now dominated by a late websterite and associated breccia. Intersections at Blue Jay Extension and Contact Zone contain 2-10% patchy disseminated, patchy net, and blebby Ni-Cu (PGE) sulfide mineralization (**Fig. 3**) with intervals along the footwall contact (e.g., BT-09-98/345-349; **Fig. 11A**) containing sporadic semi-massive (30%) mineralization (**Fig. 3**; Farhangi et al., 2013).

2.3.2.2 Ultramafic Series (US)

The Ultramafic Series is the most abundant component of the BTIC and could be further subdivided into the Lower, Middle, and Upper Ultramafic Series:

The Lower Zone of the US is dominated by apple-green to black, fine to medium-grained dunite containing minor interstitial chromite (**Fig. 5A**), which is commonly interlayered with dark-grey, oikocrystic lherzolite and lherzolite (**Figs. 5B-C**) and less commonly with olivine websterite and websterite (**Figs. 5D-E**).

The Middle Zone of the US is defined by the Black Label Chromite Zone (BLCZ), a stratiform chromitiferous zone with an aggregate thickness of ~25m (Mehrmanesh et al., 2013; **Fig. 4**) that contains intercalations of very thinly laminated (<1 mm) to very-thickly bedded (>60 cm) lightly disseminated (<10 modal%) chromite hosted in peridotite/dunite to massive (>90 modal) chromitite (Mehrmanesh et al., 2013) interbedded with barren olivine pyroxenite (rare), lherzolite, and dunite layers. Bedding contacts range from sharp through graded to diffuse and may be straight, flame and load, or irregular (Mehrmanesh et al., 2013; **Figs. 5F-H**). In the NW and SE parts of the BTIC groups of chromite layers are semi-continuous and can be broadly correlated along strike (Mehrmanesh et. al, 2013), however, in the core of the intrusion the BLCZ has been magmatically brecciated by a late websterite (**Figs. 4 and 8**). The Middle Zone also contains interlayered dunite, lherzolite, and lesser olivine websterite and websterite (**Fig. 4**).

The Upper Zone of the US is defined by the Black Thor Chromite Zone (BTCZ), a stratiform chromitiferous zone with an aggregate thickness up to 100m (Tuchscherer et al., 2009; Weston and Shinkle, 2013; Carson et al., 2013, 2015). Similar to the BLCZ in many respects, the BTCZ is characterized by disseminated to massive chromitite interbedded with dunite, lherzolite, and lesser olivine pyroxenite. It does not appear that the late websterite has transgressed the BTCZ. The Upper zone also contains websterite in the upper sections.

2.3.2.3 Mafic Series (MS)

The MS is comprised of an upward fractionating sequence of feldspathic pyroxenite, gabbro, and less commonly anorthosite dated at 2734.1 ± 0.6 Ma by Houlé et al. (*in prep*). Many contacts are gradational, but some gabbros (i.e., ‘ferrogabbro’) have sheared contacts with underlying pyroxenites and appear to have intruded into the overlying intermediate to mafic volcanic rocks (Carson et al., 2015; **Figs. 3** and **4**).

A 2728.7 ± 2.4 Ma biotite gabbro (Houlé et al., *in prep*) has intruded the upper part of the US and MS in the SW part of the BTIC (**Fig. 3**).

2.3.3 Late Websterite Intrusion

A 2733.6 ± 1.0 Ma Late Websterite Intrusion (LWI; Houlé et al., *in prep*) transgresses the BS, and the Lower and Middle Zone of the US (**Fig. 4**). The intrusion is ~ 1 km² in surface extent (**Fig. 3**) with the thickest intersections (>200m) at depth in the central part and the thinnest intersections (<5m) at the margins. The intrusion created a variety of breccias whose characteristics were used to divide the LWI into two zones:

2.3.3.1 i. Unhybridized Websterite Zone

The Unhybridized Websterite Zone (UWZ) composes 30-50 vol% of the LWI and contains up to 10% clasts, but not hybridized websteritic matrix. 80-85 vol% of UWZ is comprised of websterite. It is light grey, medium-grained, and contains abundant orthopyroxene and varying amounts of interstitial clinopyroxene and plagioclase (**Fig. 6A**). Only the core of the LWI contains extensive (>100m) intervals of clast-free, unhybridized websterite. 15-20 vol% of UWZ is comprised of evolved feldspathic websterite to gabbronorite. Feldspathic websterite is light grey, medium- to coarse-grained, and contains abundant orthopyroxene and equal proportions of plagioclase and clinopyroxene. Gabbronorite is blue-grey, coarse-grained to pegmatitic, and

contains abundant plagioclase and equal proportions of pyroxenes. LWI feldspathic websterite occurs in small (0.5-10m) discrete pods within typical websterite (**Figs. 6B** and **10B**), whereas gabbro-norite occurs in the centers of feldspathic websterite pods and as pegmatitic dikes (<20 cm thick) that transect UWZ websterite, BTIC country rock, and hybrid rocks (**Figs. 6C-D**).

Rare intersections of websterite (e.g., BT-09-98/330-345; **Fig. 11A**), with minor clast content (<5%), are present along the basal contact that contain up to 5% disseminated to blebby Fe-Ni-Cu-(PGE) sulfide mineralization (**Fig. 7F**). UWZ websterite can generally be distinguished from BTIC websterite (**Fig. 5E**) by: a) field relationships (no major intersections of BTIC pyroxenite occur in the basal portion), b) near absence of alteration in UWZ, and c) common presence of ultramafic clasts in UWZ. Isolated dunite clasts within UWZ are relatively unaltered with only minor sulfide-serpentine-magnetite veinlets. The degree of alteration increases with clast abundance and at footwall contacts (**Figs. 7C-D**).

2.3.3.2 ii. Black Label Hybrid Zone

The Black Label Hybrid Zone (BLHZ) composes 50-70 vol% of the LWI and contains up to 60 vol% BTIC clasts with hybridized websteritic matrix. The BLHZ is a complex dm-m scale intercalation of homolithic and heterolithic breccias associated with heterogeneously hybridized rocks (i.e., the matrix), which commonly contain modified clasts and websterite intervals (**Fig. 8**). They occur as 1-10s m-thick intervals marginal to the LWI, as <10m thick sills extending laterally into the BTIC, and as <5m thick isolated pods surrounding stoped blocks (**Fig. 9**). Some “clasts” within the BLHZ are up to 20m thick and have layering oriented parallel to that of adjacent BTIC, so they are likely still attached. 5-10 % of BLHZ exhibits patchy disseminated to net-textured (5-20%) Fe-Ni-Cu-(PGE) sulfide mineralization in the Northeast, Central, and Southwest Breccia Zones (**Fig. 9**).

Two hybrid rock types can be subdivided based on dominant clast lithology: 1) hybrid harzburgites contains more dunite-lherzolite clasts than chromitite clasts (**Figs. 7A-D**), whereas 2) hybrid chromite harzburgites contains more chromitite clasts than dunite-lherzolite clasts (**Figs. 7E and G-H**). Hybrid harzburgite comprises 90-95 vol% of hybrid rocks and occurs proximal to brecciated dunite-lherzolite intervals in the Lower and Middle Zone of US. Hybrid chromite harzburgite comprises 5-10 vol% of hybrid rocks and occurs proximal to brecciated chromitite intervals in the BLCZ. Both hybrid rock types contain varying proportions of olivine and/or chromite xenocrysts (**Fig. 12**). Both lithologies are extremely heterogeneous and vary on dm to m-scales, but are depicted on deposit-scale maps in terms of the dominant rock type (i.e., hybrid harzburgite versus chromite harzburgite: **Figs. 3 and 9**).

2.3.3.3 Clast Variability in LWI

From increasing to decreasing abundance: lherzolite, dunite, chromitite, and rare olivine pyroxenite clasts make up to 10 and 60 vol% of UWZ and BLHZ, respectively. There are no systematic differences in clast shape, size, or lithology between the UWZ and BLHZ, only the relative proportions of clasts are different. Clasts are variably sized (0.01-2m, rarely >5m) with subangular to amoeboidal geometries and sharp to diffuse contacts and are heterogeneously distributed throughout (**Table 1; Fig. 7**). Some intervals may exhibit evidence of magmatic flow with preferential alignment of clasts (**Fig. 7B**), whereas some have bedding orientations similar to adjacent unbrecciated BLCZ (**Fig. 8B**, see figure caption). Clast geometries vary systematically: subangular to subrounded clasts are dominant along the basal contact, whereas rounded to amoeboidal clasts are dominant in the core and upper margin of the LWI. Thin (<5 cm) dikelets of websterite occur in BTIC wall rocks, commonly in association with subangular clasts in the basal sections. The sizes of clasts and the sharpness of their contacts vary, but show

no regular distribution. Mineralogy, textures, and a brief description of each clast lithology are presented in **Table 1**.

2.4 Analytical Methods

2.4.1 Field Work

Fieldwork for this project was carried out during the months of June and July 2013 at the Cliffs Natural Resources “Esker Camp” in the James Bay Lowland region of Northern Ontario. Selected intervals of 39 drill cores were relogged at variable scales depending on interval heterogeneity to establish the igneous stratigraphy, structure, mineralogy, grain sizes, and other mineralogical-structural-textural attributes relevant to the petrogenesis of the lithologies of interest in this study. In text and figures drill core intervals are referred to by location (in this case BT), year drilled (YY), sequential number (XXX), and depth in metres (/XXX; e.g., BT-11-177/230). A total of 314 representative samples were taken for microscopic and petrographic study, mineral analysis, and whole-rock geochemical analysis, including 123 UWZ websterites, 19 UWZ feldspathic websterites and gabbronorites, 139 BLHZ olivine websterites and harzburgites, 10 BTIC lherzolites and dunites, and 23 BLCZ chromitites. Representative half-core NQ (47.6 mm diameter) and lesser HQ (63.5 mm diameter) core samples were slabbed, ground on 165 μm Buehler Apex diamond grinding discs, optically scanned, and examined under a binocular microscope to establish relevant mesoscopic textures.

2.4.2 Petrography

A total of 124 representative samples were examined in thin section, including eighty-one 26x46 mm polished thin sections, seventeen 26x46 mm unpolished thin sections, twenty-one 37x74 mm thin sections, and five 50x74 mm thin sections, using transmitted and reflected light on a Nikon Eclipse E600 POL polarizing petrographic microscope equipped with a Leica DFC-

480 digital camera. Petrography was done to establish mineralogy and microscopic textures relevant to the petrogenesis of the BLHZ, and to select representative, least-altered minerals and samples for mineral and whole rock geochemistry, respectively.

2.4.3 Mineral Chemistry

Five polished thin sections (385 total spots) were analyzed by energy-dispersive X-ray emission spectrometry using a JOEL 6400 scanning electron microscope in the Solid-Phase Section of the Laurentian University Central Analytical Facility in the Willet Green Miller Centre on the LU campus to establish the nature of zoning of silicates and oxides. Operating conditions were 15kV accelerating potential and 15 nA beam current for all phases.

Twelve polished thin sections (399 total spots) were analyzed by wavelength-dispersive X-ray emission spectrometry using a Cameca SX-100 electron probe microanalyzer at the Ontario Geoscience Laboratories (Geo Labs) in the Willet Green Miller Centre to determine the compositions and zoning of olivine, pyroxene, chromite, and plagioclase. Operating conditions for major elements were 20kV accelerating potential and 35 nA beam current, and for minor elements 20 kV accelerating potential and 200 nA beam current. Counting times ranged from 10-40 seconds on both peaks and backgrounds. A suite of natural and synthetic mineral and oxide standards was used to monitor accuracy and precision (**Electric Appendix A**).

2.4.4 Whole Rock Geochemistry

A total of 75 representative samples, including 20 UWZ websterite, 9 UWZ feldspathic websterite and gabbronorite, 30 BLHZ olivine websterite and harzburgite rocks, and 10 BTIC dunite-lherzolite and 6 BLCZ chromitite clasts, were selected for whole-rock geochemical analysis. All samples were a minimum of 20 cm length of quarter-core (~0.2 kg) to ensure sample homogeneity. With every 15 samples a spinifex-textured komatiite rock standard (ALX-

1: from the Alexo area of the Abitibi greenstone belt, ON, Canada; Arndt, 1986) and a blind duplicate were analyzed. Sample preparation and analysis were done at Geo Labs. Crushing was done using a low-Cr roll crusher that was opened and cleaned with a brush and compressed air between samples. Pulverization done in agate ball mills that were cleaned with a brush, compressed air, and methyl alcohol between samples. Major, minor, and trace elements were analyzed by wavelength-dispersive X-ray fluorescence spectrometry: major and minor elements were analyzed on fused glass disks and selected trace elements (V, Cr, Co, Ni, Cu, Zn) on pressed powder pellets. High-Cr samples were analyzed using a low sample:flux (1:25) and significant dilution (7-40x: Burnham et al., 2010). Rare-earth and additional lithophile trace elements were analyzed by inductively-coupled plasma mass spectrometry (ICP-MS) following a 10-day mixed-acid HF-HClO₄-HNO₃-HCl digestion (Burnham, 2008). Sulfur was determined using Leco® inductive combustion and infrared detection. All data have been recalculated to 100% volatile-free to compensate for variable degrees of post-magmatic hydration.

Selected Fe-Ni-Cu sulfide-bearing samples were dissolved in aqua regia and analyzed for Ni, Co, Pb, Zn, and Cu by flame atomic absorption spectroscopy and for As, Sb, Bi, Cd, Co, Cu, Pb, Mo, Ni, Se, Ag, Te, Tl, Sn, W, and Zn by solution ICP-MS. The same samples were analyzed for Au, Pt, Pd, Rh, Ru, and Ir by ICP-MS following NiS fire assay pre-concentration and Te co-precipitation (Burnham, 2008). Accuracy and precision data are given in **Electronic Appendix B**.

2.4.5 Terminology

In this paper we use several terms to describe the processes by which silicate melts or magmas (silicate melt ± phenocrysts ± autoliths ± xenocrysts ± xenoliths) incorporate other materials:

dissolution and *assimilation* (used interchangeably) are the chemical incorporation process that produces a contaminated or hybrid *melt*

contamination and *hybridization* (used interchangeably) are the physical ± chemical incorporation processes that produce a contaminated or hybrid *magma*

We also make distinctions between xenoliths, cognate xenoliths, and autoliths:

Xenoliths and *clasts* are inclusions derived from *unrelated rocks*

cognate xenoliths are inclusions derived from rocks formed from a *related magma*, but not necessarily the same magma

autoliths are inclusions derived from the *same magma*

And between xenocrysts and cognate xenocrysts, and phenocrysts:

xenocrysts are phenocrysts derived from *unrelated rocks*

cognate xenocrysts are phenocrysts derived from rocks formed from a *related magma*, but not necessarily the same magma

phenocrysts are the first crystals to crystallize from a cooling magma, and therefore have sufficient room to grow to a large size

2.5 Petrography

2.5.1 Unhybridized Websterite Zone

2.5.1.1 Websterite

The dominant rock type in the UWZ is a medium-grained (1-5 mm), meso-accumulate websterite containing 70-95 modal% orthopyroxene (Opx), 5-20% clinopyroxene (Cpx), <10% plagioclase (Pl), <2% sulfide, <3% olivine (Ol), and <2% chromite (Chr; **Fig. 12**). While the websterite contains significant proportions of both pyroxenes, the ‘websterite’ is trending toward

an orthopyroxenite (**Fig. 12**). Samples with greater Opx:Cpx ratios (up to 95:5) exhibit more idiomorphic textures (**Fig. 13A**); whereas samples with lower Opx:Cpx ratios (down to 80:20) exhibit more hypidiomorphic textures (**Fig. 14A**). Medium to coarse-grained (>5 mm) Opx is present as a cumulus phase (subhedral-euhedral) with fine to medium-grained Cpx and Pl only as an intercumulus phase (interstitial-subhedral). Opx is unzoned but contains extensive exsolution blebs, grain boundary accumulations, and granular exsolutions of Cpx. Cpx contains markedly finer exsolution lamellae than Opx (**Fig. 14B**).

Limited intervals (e.g., BT-09-28/220-235) of websterite contain 5-15% oikocrystic Cpx (4-20 mm) and up to 5% pyrrhotite-pentlandite-chalcopyrite that is commonly blebby and bounded at high dihedral angles (72-110°) to unaltered pyroxene grains with no apparent connecting veinlets, suggesting a primary magmatic origin. Both websterite and isolated clasts show remarkable preservation of primary igneous phases with alteration generally occurring only along grain boundaries. Pl is more often altered to sericite and Cpx is more often altered to actinolite - tremolite - talc - chlorite ± hornblende; whereas Opx is less commonly altered to actinolite - talc - chlorite - tremolite ± “bastite”.

2.5.1.2 Feldspathic Websterite and Gabbronorite

Feldspathic websterite and gabbronorite show a range in mineralogy and texture with tandem increases in Cpx, Pl, and sulfide contents with grain size (**Fig. 12**). Alteration in UWZ feldspathic websterite and gabbronorite is similar to that in ‘typical’ websterite.

Feldspathic websterite is a light grey, medium- to coarse-grained ortho-mesocumulate rock with 40-80% cumulus Opx, 15-50% cumulus Cpx, 5-20% intercumulus Pl, and <5% intercumulus Fe-Ni-Cu-(PGE) sulfides (**Fig. 14C**).

Gabbronorite is a bluish-grey, coarse-grained subophitic to pegmatitic orthocumulate rock with 20-70% cumulus Pl, 10-60% cumulus Opx, and 20-50% oikocrystic Cpx, and 5-10% blebby Fe-Ni-Cu-(PGE) sulfides (**Fig. 14D**). Cpx contains fine exsolution lamellae of Ca-poor pyroxene.

2.5.2 Black Label Hybrid Zone

Detailed descriptions of the mineralogy, texture, and alteration of separate clast lithologies are given in **Table 1**. Described below are the two main hybrid rock types, hybrid harzburgite and hybrid chromite harzburgite.

2.5.2.1 BLHZ Harzburgite

BLHZ harzburgite *sensu lato* (**Figs. 8A and 13B-C**) comprises 30-75% Opx, 5-60% Ol, and 2-15% Cpx (**Fig. 12**) with up to 10% Chr and/or up to 20% Fe-Ni-Cu-(PGE) sulfides. Thus, it ranges from Ol websterite (BLHZ-OW) with 5-40% Ol (**Figs. 7A-B**) to harzburgite *sensu stricto* (BLHZ-H) with 40-60% Ol (**Figs. 7C-D**). Ol occurs in heterogeneously dispersed patches of crystals or aggregates that increase in abundance toward clasts. Ol appears to be disaggregated from once-larger clasts and thus is considered xenocrystic (**Figs. 15E-F and 16A**). No xenocrystic (matrix) Opx has been observed; Opx on the margins of BTIC clasts exhibit corrosive contacts with UWZ Opx.

There are two textural types of hybrid harzburgite. 1) Most harzburgites exhibit coarse to very coarse-grained, poikilitic textures with 2-9 mm chadacrysts of cumulus Ol within 0.5-2 cm Opx oikocrysts (**Figs. 13C and 15A-B**). 2) Harzburgite less commonly exhibits a medium- to coarse-grained, ad- to mesocumulate texture with intercumulus crystals or clusters of Ol impinged by euhedral Opx (**Figs. 13B and 15C-D**). Matrix Ol exhibits corrosive margins with blebby, irregular shapes, and exhibits no undulatory extinction, kink bands, or sub-grain

boundaries (**Fig. 15B**). Locally, Ol is partially or completely serpentinized, Chr is replaced by magnetite along rims, and pyroxenes exhibit similar alteration to the UWZ, but many hybrid rocks are fresh with more significant alteration as Ol content increases.

2.5.2.2 BLHZ Chromite Harzburgite

BLHZ chromite harzburgite *sensu lato* comprises varying proportions of 20-70% Opx, 10-40% Chr, 5-60% Ol, and 5-20% Cpx (**Figs. 8B and 13D**) with some intervals containing up to 20% Fe-Ni-Cu-(PGE) sulfides. It also ranges from Chr Ol websterite (BLHZ-CW) with 5-40% modal Ol (**Fig. 7E**) to Chr harzburgite *sensu stricto* (BLHZ-CH) with 40-60% Ol (**Figs. 7G-H**). Alteration is similar to BLHZ harzburgite.

BLHZ-CH exhibits very coarse to coarse-grained poikilitic textures with 2-9 mm cumulus Ol and 0.2-3 mm Chr occurring as chadacrysts within 0.5-2 cm Opx oikocrysts (**Figs. 16A-B**). Xenocrystic Chr exhibits no evidence of consumption, whereas xenocrystic Ol exhibits the same corrosive textures as in BLHZ-H. Both Ol and Chr occur in patches of crystals or aggregates within the hybridized matrix that increase in abundance toward clasts (**Fig. 16A**). Along clast margins partially digested Ol grains are enveloped by poikilitic Opx that occupies Chr-free haloes surrounded by Chr. This texture is interpreted to represent replacement of once-larger Ol grains by Opx (**Fig. 16B**). This process may aid in the incorporation of interstitial Chr (to Ol) into the LWI matrix because as Ol is replaced by UWZ Opx the ‘framework’ Chr is disaggregated and surrounded by the newly formed crystals (**Figs. 16C-E**).

2.5.2.3 BLHZ Ni-Cu-PGE Mineralization

BLHZ locally contains up to 20% patchy disseminated to patchy net-textured Fe-Ni-Cu-(PGE) sulfides (pyrrhotite >> pentlandite > chalcopyrite) in the Northeast, Central and Southwest Brecciated Zones (**Fig. 9**; Farhangi et al., 2013). Sulfides most commonly occur interstitial to

aggregates of Ol \pm Chr and dunite/chromitite clasts in the hybrid matrix. The patchy mineralization style is an effect of Ol and Chr being “wetted” (dihedral angles = 15-70°, median = 43°) with no affinity for Opx (65-105°, median= 85° **Fig. 16F**). The large range in dihedral angles may be an effect of different fO_2 conditions from the three distinct mineralized zones (see Rose and Brenan, 2001).

2.6 Mineral Chemistry

Representative electron probe microanalyses of major and selected minor elements in Ol, Opx, Cpx, Pl, and Chr in UWZ, BLHZ, and BTIC clasts are presented in **Table 2**. The full set of mineral analytical data is given in **Electronic Appendix A**.

Ol ranges Fo₆₂₋₅₉ in UWZ, Fo₇₃₋₆₄ in BLHZ (xenocrysts and marginal crystals), and Fo₇₈₋₇₀ in BTIC clasts. The lower Fo contents of analyzed BTIC Ol compared to the nearby Eagle’s Nest area (Fo₆₈: Mungall et al., 2010) probably reflects the sampling locations; all analyzed dunite-lherzolite clasts are adjacent to the Ultramafic Series not the more primitive Basal Series (Carson et al., 2013, 2015). Ca ranges <0.10% in UWZ Ol, 0.01-0.13% in BLHZ Ol, and 0.01-0.04% in BTIC Ol; Mn ranges 0.26-0.29% in UWZ Ol, 0.20-0.28% in BLHZ Ol, and 0.16-0.23% in BTIC Ol; and Cr ranges <0.01% in UWZ Ol, <0.02% in BLHZ Ol, and <0.03% in BTIC Ol. The Ca and Mn contents are lower than komatiitic Ol in rapidly-cooled volcanic environments (e.g., Leshner, 1989; Arndt et al., 2008), but higher than komatiitic Ol in more slowly-cooled subvolcanic environments (e.g., Donaldson et al., 1986). Ni decreases slightly with decreasing Fo content in UWZ and BTIC Ol and more strongly in BLHZ Ol (**Fig. 17A**). Transects across several silicate grains reveal no discernible chemical zonations.

Opx ranges En₈₄₋₇₈ in UWZ, En₈₅₋₈₂ in BLHZ (both hybrid lithologies), and En₈₇₋₈₃ in BTIC clasts. Exsolutions, ‘granules’, and grain boundary accumulations of Cpx in Opx range

Wo₄₇₋₄₁ En₅₂₋₄₈ Fs₇₋₅ (**Fig. 18A**). Exsolution, migration, and coalescence of high-Ca pyroxene into discrete marginal grains from parental low-Ca pyroxene is common in high-temperature, slowly-cooled plutonic environments, which makes it difficult to reconstruct primary compositions (e.g., Lindsley, 1983) and complicates the application of two-pyroxene thermometry.

Isolated Cpx ranges Wo₄₇₋₄₁ En₅₂₋₄₈ Fs₇₋₅ in UWZ (**Fig. 18A**), Wo₄₆₋₄₀ En₅₂₋₄₉ Fs₈₋₅ in BLHZ (both lithologies; **Fig. 18B**), and Wo₄₇₋₄₅ En₅₁₋₄₈ Fs₅₋₄ in BTIC precursor clasts (**Fig. 18C**). Cpx in UWZ gabbronorite commonly contains fine exsolutions of Ca-poor pyroxene (**Fig. 14C**). See **Figure 18D** for a comparison of pyroxene analyses in all rock types.

Chr varies widely in major element composition depending on stratigraphic location, provenance (xenocrysts versus clasts), degree of reequilibration with trapped liquid, and alteration. Within the same sample, xenocrystic (matrix) Chr has lower Mg-Cr and higher Fe than clast Chr (**Fig. 17B**). BLCZ and BLHZ Chr (**Figs. 19A-B**) have similar Ti-V-Zn contents and are higher in Ti and lower in V-Zn than BTCZ Chr (**Fig. 19C**). This reflects the provenance of BLHZ Chr, as all hybrid rocks are adjacent to BLCZ not BTCZ. See **Figure 19D** for a comparison of Chr analyses in all rock types. Cores were analyzed to avoid secondary magnetite alteration along margins. Transects across several Chr grains reveal no discernible chemical zonations.

Pl ranges An₈₈₋₈₀ in UWZ websterite, An₈₅₋₇₉ in UWZ feldspathic websterite, and An₈₂₋₇₅ in UWZ gabbronorite (**Table 2**).

2.7 Whole Rock Geochemistry

Compositional ranges and averages of UWZ, BLHZ, and selected BTIC lithologies are given in **Table 3**. MgO variation diagrams are shown in **Figure 20**, S versus PGE variation diagrams in **Figure 21**, and selected trace and rare earth element (REE) variation diagrams are

shown in **Figure 22**. The full whole-rock geochemical dataset is given in **Electronic Appendix B**.

Degrees of alteration range from pristine magmatic rocks (UWZ websterite) to pervasively talc-serpentine altered rocks (BTIC ‘dunite’). Almost all of the Ol is pseudomorphed by serpentine-magnetite, with the exception of clasts within UWZ. There is no systematic variation in whole rock geochemistry due to alteration except for variations in LOI (**Fig. 20** and **Table 3**).

2.7.1 Major and Compatible Trace Elements

UWZ lithologies have compositions that vary with abundances of primary Opx-Cpx-Pl cumulus phases (**Fig. 12**) and trace element abundances that vary in the order websterite < feldspathic websterite < gabbronorite. UWZ websterites (clast-free) are dominated by Opx and contain more Si-Ca-Na-Sr-Sc-Zr-Mo, similar Ti-Cr-Zn-V-Mg-Al-Fe, and less Ni-Co-LOI than non-hybrid BTIC clasts (**Figs. 20A-H**); and contain more Si-Mg-Ca-Na-Sr-Sc-Zr, similar Mo, and less Zn-Ni-Cu-Al-Ti-Cr-Fe-V than non-hybrid, chromiferous BTIC clasts. UWZ feldspathic websterites are dominated by Cpx and contain more Si-Ca-Na-Al-Sc-Cu-Zr-Mo-V and less Fe-Mg-Zn-Co than UWZ websterites. UWZ gabbronorite are dominated by Pl and contain the same elemental increases and decreases as the former lithology with significant increases in Sr-Cs-Rb-Na-Al (**Table 3**).

Chr-poor BTIC clasts have compositions that overlap those of adjacent non-hybrid BTIC wall rocks that vary with the abundances of primary Ol-Opx cumulus phases (see **Table 1** for clast mineralogy), and trace element abundances that vary in the order dunite < lherzolite < Ol pyroxenite (**Figs. 20A-H**). BTIC dunite clasts are dominated by Ol and contain more Mg-Fe-Ni-Zn-Cr-Co-S-LOI and less Si-Ca-Al-V-Ti-Na-Sc-Cu than UWZ lithologies. BTIC lherzolite clasts

are dominated by Opx-Ol and contain more Si-Al-Ti-Ca-Cu and less Mg-Fe-Zn-Co-Cr-Ni-S-LOI than BTIC dunite. BTIC Ol pyroxenite clasts are dominated by Opx-Cpx and exhibit similar but less intense enrichments/depletions than UWZ lithologies (**Table 3**).

Chr-rich BTIC clasts have compositions that overlap those of adjacent non-hybrid Chr-rich BTIC wall rocks that vary with the abundances of primary Chr-Ol-Opx cumulus phases, and trace element abundances that vary in the order massive < matrix-textured < net-textured chromitite. BTIC massive chromitite clasts contain more Ti-Al-Cr-Fe-Cu-Ni-V-Zn-Co-S, similar Sc-Mo-LOI, and less Si-Mg-Ca-Na-Sr-LOI than clast-free UWZ lithologies. BTIC matrix-textured chromitite clasts are dominated by Chr-Ol-Opx \pm Cpx and contain more Si-Mg-Ca-Cu-Ni-LOI, similar Co-Mo, and less Ti-Al-Cr-Fe-Zn-V than massive chromitite (**Table 3**). BTIC net-textured chromitite clasts are dominated by Ol-Opx-Chr and contain the same elemental increases and decreases as the former lithology (**Table 3**).

Chr-poor hybrid lithologies have compositions that are intermediate between clast-free UWZ websterite and Chr-free dunite-lherzolite clasts, and vary with the abundances of xenocrystic Ol and primary Opx \pm Cpx. BLHZ harzburgites exhibit intermediate Si-Al-Mg-Fe-Ca-Na-Ni-Zn-Co-S-LOI (**Figs. 20A-H; Table 3**). BLHZ Ol websterites contain more Si-Ca-Al-Na and less Mg-Fe-Ti-Ni-LOI than BLHZ harzburgites. Trace element abundances vary in the order harzburgite < Ol websterite.

Chromitiferous hybrid rocks have compositions that are intermediate between clast-free UWZ lithologies and BLCZ clasts, and vary with the abundances of xenocrystic Ol \pm Chr and primary Opx \pm Cpx. BLHZ Chr harzburgites exhibit intermediate Si-Ti-Al-Cr-Mg-Fe-Ca-Ni-V-Cu-Zn-Co-LOI. BLHZ Chr Ol Websterites contain more Si-Al-Ca-Fe-Cu-Sr-S and less Mg-Ni-

LOI than BLHZ Chr harzburgites. Trace element abundances vary in the order Chr harzburgite < Chr Ol websterite.

2.7.2 Incompatible lithophile elements

Clast-free UWZ lithologies have the highest abundances of highly to moderately incompatible lithophile elements (HILE-MILE), clast-bearing hybrid lithologies have intermediate abundances, and BTIC clasts have the lowest abundances (**Table 3; Fig. 22F**).

UWZ websterites are slightly enriched in Th-LREE and HREE relative to MREE with variably positive U ± Sr anomalies and variably negative Nb-Ta anomalies. UWZ feldspathic websterites and gabbronorites have similar patterns (i.e., positive U and negative Nb-Ta anomalies), but progressively higher abundances of HILE-MILE and stronger positive Eu-Sr anomalies in the order websterite < feldspathic websterite < gabbronorite (**Fig. 22A**). Zr-Hf appear to be anomalously enriched relative to elements of similar compatibility, but are at or near lower limits of detection (LLD).

Chr-poor BTIC clasts exhibit broadly similar patterns as the above lithologies, but have lower abundances of HILE-MILE (**Fig. 22B**), exhibit HILE-MILE abundances in the order Ol pyroxenite > lherzolite > dunite, and are more strongly enriched in HREE than in MREE in the order dunite > lherzolite > Ol websterite, consistent with komatiitic Ol housing HREE more than MREE (Rollinson, 1993). Chr-rich BTIC clasts are broadly similar in pattern and abundance as the above lithologies, but are strongly enriched in Ti-Sr and exhibit HILE-MILE abundances in the order net-textured > matrix-textured > massive chromitite.

Chr-poor BLHZ lithologies exhibit intermediate patterns and abundances of HILE-MILE with most samples falling within the fields of websterite and/or dunite-lherzolite (pink and green shaded regions respectively; **Fig. 22D**). These lithologies exhibit HILE-MILE abundances and

elevated LREE over HREE in the order BLHZ Ol websterite > harzburgite with a strong Sr depletion, reflecting the addition of Ol.

Chr-rich BLHZ lithologies exhibit intermediate patterns and abundances of HILE-MILE, with most samples falling within the fields of websterite and/or chromitite (pink and grey shaded regions respectively; **Fig. 22E**). These lithologies exhibit HILE-MILE abundances in the order BLHZ Chr websterite > Chr harzburgite with strong Ti enrichment, reflecting addition of Chr.

2.7.3 Chalcophile elements

Clast-free UWZ websterite lithologies contain less Au-Ir-Rh-Ru-S but similar amounts of Pd-Pt as other lithologies (**Table 3; Fig. 21**). Chalcophile element abundances vary in the order websterite > feldspathic websterite > gabbronorite, which reflects the greater abundance of sulfide mineralization in websterite.

Chr-poor BTIC clasts contain less Au-Ir-Rh-Ru but similar amounts of Pd-Pt-S as other lithologies. Chalcophile element abundances vary in the order Ol websterite > lherzolite > dunite, inversely proportional to S content (**Table 3; Fig. 21**).

Chr-rich BTIC clasts contain less S (see *mass. chromitite*, **Table 3**), similar Au-Pd, and much more Pd-Pt-Ir-Rh-Ru (**Fig. 21**) than other lithologies. Chalcophile element abundances vary in the order massive > matrix-textured > net-textured, inversely proportional to S contents. Au appears to be decoupled from Pd-Pt-Ir-Rh-Ru in BLCZ lithologies. Net-textured chromitite has S contents similar to Chr-poor clasts with high chalcophile element abundances similar to other chromitite clasts (**Fig. 21**).

Hybrid lithologies have lower Ru, similar Pt-Ir-Rh, and higher S-Au-Pd than other lithologies. Chromitiferous hybrid rocks generally show the greatest enrichment in chalcophile elements of the hybrid lithologies (**Fig. 21 and Table 3**), reflecting the high PGE contents in

BLCZ clasts. There is a weak positive correlation between S and PGE, but still considerable scatter.

2.8 Discussion

The most important problems to understand are 1) the nature and origin of the ultramafic clasts, 2) the mechanisms of assimilation and hybridization, 3) the geochemistry of the hybrid rocks, 4) the economic significance of the hybridization process, and 5) the emplacement of the LWI and genesis of the BLHZ. Each of these is discussed below.

2.8.1 Nature and origin of ultramafic clasts

The clasts in the BLHZ include only lithologies that are structurally, texturally, and mineralogically identical to those in the adjacent BTIC and lithologies that are very clearly modified versions of the same lithologies, so they are all cognate xenoliths. No exotic xenoliths of granodiorite, tonalite, gabbro, or oxide-silicate iron formation have been observed in the BLHZ. Oxide-silicate iron formation xenoliths are present in the feeder and along the basal contact, but their absence in the BLHZ suggest that those are parts of the BTIC not parts of the UWZ.

The sizes, shapes, sharpness of margins, and compositions of the clasts appear to have been controlled by the compositions of the lithologies, the thickness of layering, the nature of the contacts between layers, and the initial temperatures of the lithologies being incorporated. The margins of clasts vary from sharp to diffuse, and likely depended at least in part on the nature of the contact of the original beds in the BLCZ, which also vary from sharp to diffuse (Mehrmanesh et al., 2013). Field relationships suggest preferential injection along bedding planes, likely due to differences in rheology, degree of consolidation, and/or degree of dissolution of Ol-rich layers versus Chr-rich layers (**Figs. 6F-G and 23D**). Many clast margins appear to have been originally

bedding contacts along which magma intrusion was injected. Because clast margins should undergo post-entrainment modification by dissolution and disaggregation, margins should become more diffuse with time, so the presence of sharp margins is also consistent with many clasts having relatively short residence times before LWI solidification.

The sizes of clasts vary widely (0.01-2m, rarely >5m) and show no regular distribution, but may correspond to the thickness of the primary bedding in the BLCZ (**Figs. 23A-C**; Mehrmanesh et al., 2013). Due to preferential injection along bedding planes many clasts, particularly more refractory chromitite clasts, exhibit sizes within the same range as primary bed thicknesses. This is also consistent with the clasts being derived locally and short residence time within LWI magma. There is no recognizable grading of clast sizes immediately adjacent to wall rocks.

The lithologies of clasts vary in abundance lherzolite > dunite > chromitite > Ol pyroxenite, but clast lithology depends on the lithology and scale of layering in adjacent BTIC wall rocks. For example, heterolithic breccias occur adjacent to thinly layered chromitite-dunite-lherzolite intervals (**Figs. 5G and 8B**) and homolithic breccias occur adjacent to thickly layered lherzolite-dunite intervals (**Fig. 7A**). Chromitite clasts occur almost exclusively adjacent to BLCZ wall rocks or stoped blocks. The trace element compositions of chromitite clasts are similar to the unbrecciated portions of the BLCZ, rather than the BTCZ (**Fig. 19B**). Based on this and field relationships, it appears that all chromitite clasts are derived from the BLCZ.

The shapes of the clasts vary from subangular to amoeboidal with chromitite clasts commonly exhibiting more angular and tabular shapes than silicate clasts. This is consistent with 1) chromitite clasts retaining their original layered (tabular) geometry and 2) chromitite being more refractory than dunite-lherzolite. The layering in most chromitite clasts is planar indicating

solidification before entrainment in the LWI magma (**Fig. 23B**), however, the margins of stoped chromitite blocks, particularly within the LWI core, exhibit wavy layering indicating syn-crystallization modification suggesting that they were partially consolidated at the time (e.g., BT-09-26/110; **Fig. 10B**). The presence of both angular to amoeboidal clasts within UWZ and BLHZ rocks suggests different degrees of consolidation at the time of emplacement and/or different residence times (longer for amoeboidal clasts, shorter for angular). The greater abundance of rounded clasts in the upper parts of the BLHZ and greater abundance of subangular clasts (with associated LWI dikelets) in the lower parts of the BLHZ suggest that the degree of consolidation was most likely the major control (**Fig. 11A**). Systematic variations in clast shape with location suggest that the US was less consolidated, whereas the BS was more consolidated (**Fig. 4**).

2.8.2 Contamination/hybridization

Contamination/hybridization processes involving incorporation of mafic-ultramafic rocks are common in many geological settings (e.g., Arculus et al., 1983; Kelemen, 1986; Kelemen and Ghiorso, 1986; Glazner et al., 1991; Bédard, 1993). Depending on the initial temperature and degree of consolidation of the wall rocks, the temperature and viscosity of the magma, the fluid dynamic regime, and other extensive and intensive factors, hybridization may involve several processes, including:

- 1) *Mechanical disaggregation* without dissolution, forming a hybrid magma comprising an unhybridized melt and xenoliths \pm xenocrysts
- 2) Partial melting/selective dissolution, forming a hybridized melt containing restitic xenoliths \pm xenocrysts

- 3) Mineral-melt reaction with resorption of disequilibrium phases and crystallization of hybrid peritectic phases
- 4) *Re-equilibration* of xenoliths/xenocrysts through ionic exchange with the melt
- 5) *Complete dissolution*, forming a hybridized melt

The result is a hybrid magma intermediate in composition between the original magma and the assimilated(s) that comprises a homogenous or heterogeneous melt phase with or without xenoliths or xenocrysts that may retain original compositions or be re-equilibrated (e.g., Bowen, 1922; Sparks and Marshall, 1985). Assimilation in the BLHZ appears to have involved all 5 processes.

2.8.2.1 Mechanical disaggregation

Mechanical disaggregation of cumulate clasts will hybridize the host magma by physical incorporation of foreign phases, changing the bulk composition of the magma if the phase is compositionally different from the original magma (e.g., Dungan and Davidson, 2004; Glazner, 2007; **Fig. 24A1**). In the absence of partial melting (below) this process involves thermal stress-induced fracturing (e.g., Clarke et al., 1998). This process enhances other hybridization mechanisms by increasing the surface area of foreign material (McLeod and Sparks, 1998).

Mechanical disaggregation without dissolution is suggested by the following petrographic features in the BLHZ: 1) disaggregated margins of Ol + Chr cumulate clasts that grade from clasts to Ol + Chr xenocrysts (**Figs. 13B-D**); 2) disaggregated/fractured margins of massive, adcumulate chromitite clasts with no interstitial phases (**Figs. 13D and 16E**); 3) the absence of significant (<2 modal %) Chr in uncontaminated websterite, but its presence (up to 40%) in hybrid lithologies; and 4) the lack of disequilibrium textures in Chr xenocrysts (i.e., euhedral grains with no corrosive margins; **Fig. 16E**). This has locally hybridized websteritic groundmass

through the disaggregation of ultramafic wall rocks (**Fig. 7C**) resulting in small multigrain clasts, patches, and schlieren, and in rare cases complete disaggregation of BLCZ xenoliths leaving homogeneously dispersed xenocrysts. Mechanical disaggregation without dissolution has physically (not chemically) assimilated BLCZ intervals, forming Chr-rich hybrid rocks and has formed rock with intermediate whole-rock major element (**Figs. 20A-E**), PGE (**Figs. 21B-C**) and incompatible trace element (**Fig. 22E**) compositions.

2.8.2.2 Partial melting/selective dissolution

Partial melting and selective dissolution are hybridization processes involving congruent or incongruent melting of entrained xenoliths/xenocrysts and dissolution of xenomelts (**Fig. 24T2**). The incipient partial melt of low temperature phases in the xenolith mixes with the host melt to create hybrid melt (e.g., Perhugini and Poli, 2012; **Fig. 24B1**), leaving higher temperature residual phases. The blending of incompatible trace element-rich partial melts with the host magma can produce higher-than-expected incompatible trace element contents without shifting major element concentrations outside expected ranges (e.g., Dungan and Davidson, 2004). Because low temperature phases are typically interstitial to cumulus phases, partial melting generates incipient intracrystalline melts that are preferentially localized along grain boundaries, enhancing mechanical disaggregation due to over-pressurization, resulting in the loosening of the cumulate framework (e.g., Huber et al., 2010).

Selective melting of Cpx + Pl + primary hydrous phases \pm Opx within BTIC clasts appears to have produced partial melts that mixed with the parental LWI melt to form a hybrid melt. This process is recorded in the following petrographic features: 1) corrosive textures exhibited by BTIC Opx and Cpx at clast margins (**Figs. 16A-C**); and 2) increased Chr content at the margins of matrix-textured chromitite clasts (suggesting that Cpx oikocrysts hosting Chr are

being melted). Experimental studies of komatiites (see review in Arndt et al., 2008) indicate that Cpx will melt at temperatures above 1190°C. Partially digested BTIC Opx may exist in the LWI matrix, but would only be identifiable if the composition was different from that being crystallized by the LWI magma. The above reasons may explain why no pyroxenite and very few Ol websterite clasts have been found, even in areas laterally adjacent to pyroxenitic BTIC wall rocks. Partial melting of oikocrystic Cpx within semi-massive chromitite clasts (see **Table 1** for clast mineralogy) would aid in mechanical incorporation of xenocrystic Chr. The expected mixing of BTIC clast partial melts does not show a systematic increase in BLHZ trace element concentrations (**Table 2**). This is likely because Cpx + Pl + primary hydrous phases are not of a sufficient volume in the re-equilibrated clasts to effect the abundances of incompatible elements in the hybrid rocks.

2.8.2.3 Mineral-melt reaction

Mineral-melt reaction involves dissolution of high-temperature phases by interaction with a disequilibrium melt that crystallizes a lower-temperature phase of different composition (Maury and Didier, 1991). The incongruent melting in this *reaction-pair* takes a primary early-crystallizing phase and produces a hybrid peritectic phase (Erdmann et al., 2010; **Fig. 24T3**).

Such a reaction relation exists between xenocrystic Ol and BLHZ Opx. Early crystallized Ol is not in equilibrium with more evolved silica-rich LWI melt, resulting in the formation of low-temperature orthopyroxene rims with the inferred reaction (Bowen, 1922):



This interpretation is supported by the 1) irregular, blebby geometries and corrosive margins of Ol xenocrysts, and 2) embayed margins of Ol-rich clasts associated with hybrid or

peritectic Opx (**Figs. 15A-D**). This is apparent in matrix-textured chromitite where Chr-free, Opx halos formed around residual Ol cores or no cores (**Fig. 16B**). This texture resulted from LWI melt invading into the margins of the clast lithologies, dissolving Ol, forming hybrid Opx, and leaving refractory Chr (**Figs. 16D** and **24C1**). This process is likely also a process for producing diffuse chromitite clast margins, whereas in massive chromitite clasts sharp interfaces are almost always present because there are no silicate phases to aid in the entrainment of Chr into the LWI matrix. In this case, mechanical disaggregation of Chr is the only possible process for xenocryst entrainment (**Fig. 16E**). Lherzolite and dunite clasts typically have the more diffusive, embayed contacts as the reactive nature of Ol makes removal relatively efficient.

BLHZ Opx (77-74 Mg#) is less magnesian than BTIC Opx (82-78 Mg#) but more magnesian than UWZ Opx (74-69 Mg#), suggesting that significant amounts of Ol were resorbed to locally increase the Mg# of the LWI melt crystallizing Opx (**Table 2; Fig. 18**). Hybrid Opx formation both aids and inhibits assimilation: the creation of peritectic Opx from precursor Ol involves hybridization; but the Opx armour retards further reaction between Ol and Si-rich melt (McLeod and Sparks, 1998; Bédard, 1991).

2.8.2.4 Ionic exchange/re-equilibration

Ionic exchange in magmatic systems occurs when an ion of one species in the melt exchanges with an ion of another species in a solid residue or melt (Leshner, 1990). The effect of this exchange is a re-equilibration of early-crystallized solid phases within the host magma and subsequent chemical hybridization. This process is most efficient when the magma temperature is only slightly lower than the solidus of the xenocryst (refractory phases facilitate ionic diffusion without melting) and where there is a strong compositional gradient (Clarke, 2007).

Xenocrystic BLHZ Ol compositions (F_{073-64}) are between those of UWZ Ol (F_{062-59}) and

BTIC Ol (F_{O78-70} ; **Table 2**). Ol that is present in the matrix and margins of clasts have lower Ni-Mg compared to Ol within adjacent clasts (e.g., sample BT-09-32, **Fig. 17A**), even where the clasts are unambiguously the source of the xenocrystic Ol (e.g., **Fig. 13B**). The xenocryst composition may change as they equilibrated with the less magnesian liquid (e.g., Klügel, 1998; **Fig. 24D1**). Some BLHZ Ol is depleted in Ni, but this is likely a result of partitioning into sulfide melts, which were present in significant abundances in the hybrid rocks (**Figs. 7D and 20F**).

Chromite shows no corrosive textures, but there are significant chemical differences between matrix and clast Chr. There is variation between samples because they were taken from different locations in the BLHZ (i.e., different BLCZ wall rock stratigraphy) and because of different trapped liquid shifts (see Barnes, 1986; Schulte et al., 2012). However, within individual samples (e.g., GT-13-13, **Fig. 17B**), xenocrystic Chr has lower Mg-Cr than clast Chr. Diffusive ion exchange between the compositionally distinct xenocrystic Chr and the LWI melt may explain this (e.g., Spandler et al., 2007) and has resulted in chemical (not physical) assimilation.

2.8.2.5 Dissolution

Complete dissolution is recorded geochemically by the absence of significant Chr (<2%) and Ol (<3%) in contaminated websterite samples, forming clast/xenocryst-free rocks of intermediate whole-rock major element (**Fig. 20**), PGE (**Fig. 21**), and incompatible trace element geochemistry (**Figs. 22C-D**). However, this process is minor as almost all hybrid rocks contain xenoliths/xenocrysts; it is likely that the magma would have become quickly saturated in these phases and could not dissolve them.

2.8.2.6 *Integrated model of hybridization*

The data and interpretation presented thus far support an integrated, interdependent model of xenolith assimilation and host magma hybridization that is similar to models suggested by other authors (Dungan and Davidson, 2004; Beard et al., 2005; Clarke, 2007). At the onset of hybridization, large (>5m) blocks of BTIC country rock were entrained into the LWI magma, which likely fragmented due to shear flow and thermal stress-induced fracturing (**Fig. 24T1**). Physical integrity was further compromised by partial melting of the intercumulus phases (Cpx + Pl \pm Opx \pm primary hydrous phases) of the clasts (**Fig. 24 T2**). Clast-derived xenomelts mixed with the host melt and dissolved (**Fig. 24B1**). Overpressurization of the cumulate framework due to intergranular partial melt accumulation, coupled with mechanical disaggregation, disintegrated polymineralic clasts and generated xenocrysts that were incorporated into the matrix of the LWI (**Fig. 24A1**). The increase in surface area/volume from xenoliths (310-126000 cm³) to disaggregated xenocrysts (0.13-2.54 cm³) greatly enhanced the efficiency of hybridization. In most parts of the BLHZ, local heterogeneities were retained in the form of polygrain aggregates, larger intact clasts, and patches or schlieren of xenocrysts (**Fig. 24T3**). In some areas dispersal was enough to reduce heterogeneities to a crystal-scale and resulted in complete hybridization (**Fig. 24T4**). When physically incorporated, xenocrystic Ol dissolved in the silica-rich melt to form hybrid Opx (**Fig. 24T3**). Very locally, dissolution of xenocrystic Ol was great enough to form clast/xenocryst-free websterite rocks of intermediate whole-rock major element compositions. The Ol-Opx reaction, where ‘framework’ Chr is present interstitially to Ol, allowed for the physical dispersion of Chr grains at clast margins into the matrix (**Fig. 24C1**). The LWI melt does not appear to have consumed any of the chromitite, but it has locally reduced the grade of the mineralization through dilution and dispersal. Lastly, refractory Chr and partially-retained Ol xenocrysts re-equilibrated with the melt (**Fig. 24D1**). The interdependent

assimilative mechanisms of 1) mechanical disaggregation, 2) partial melting of low temperature phases, 3) Ol-Opx reaction-relation, 4) xenocryst re-equilibration, and – very locally – 5) complete dissolution, resulted in the physical and chemical hybridization of the LWI magma and formation of the BLHZ.

2.8.3 Hybrid geochemistry

The whole-rock major and trace element geochemistry of the hybrid rocks is intermediate between the websteritic magma, which crystallized Opx + Cpx ± Pl, and BTIC xenoliths/xenocrysts, which contain Ol ± Chr ± Opx ± Cpx (**Figs. 20 and 21**). UWZ contains <3 modal % Ol and <2% Chr whereas BTIC xenoliths contain 5-98% and 5-98%, respectively-(**Fig. 12**). These data and modal Ol and Chr contents indicate that the degree of *hybridization* by dunite ± chromite xenoliths and Ol ± Chr xenocrysts ranges up to 60% Ol and up to 40% Chr.

The amount of *assimilation* is more difficult to estimate, as the UWZ is composed mainly of cumulate rocks. However, comparing Th/Yb and Nb/Yb ratios of UWZ (0.2 and 0.7), most strongly hybridized BLHZ (0.3 and 0.8), and most strongly hybridized clast-free BLHZ (0.3 and 0.7), it appears that there has been up to 60% assimilation (**Fig. 25**).

2.8.4 Sulfide mineralization and economic significance

The Ni-Cu-(PGE) mineralization is being studied by Farhangi et al. (*in prep*) and was not a focus of this study, but this study places important constraints not only on the origin of the low-grade Ni-Cu-(PGE) mineralization in the BLHZ, but also the low-grade mineralization at Blue Jay Extension and in the Contact Zone, as well as the higher-grade mineralization at Blue Jay and Eagle's Nest. The majority of the BTIC, including the BTCZ and especially the BLCZ contain little if any sulfides (**Table 3**; Farhangi et al., 2013; Weston and Shinkle, 2013). None of these occurrences are economic, but there is economic mineralization in what appears to be the feeder

of the nearby Double Eagle Intrusive Complex (Eagle' s Nest Mine, 11,131 Mtonnes at 1.7% Ni, 0.9% Cu, and 4.0 gpt Pd+Pt: Burgess et al., 2012; Mungall et al., 2010).

The strong spatial association of minor Fe-Ni-Cu-(PGE) sulfides with the BLHZ (NE, Central, and SW breccia zones) and the absence of significant amounts of sulfides elsewhere in the BTIC except along or near the basal contact (Blue Jay, Blue Jay Extension, Contact zone) indicates that the hybridization process induced sulfide saturation. Although the correlations between Ni-Cu-Au-PGE and S in the hybrid zones are weak, Au-Pt-Pd-Ir-Rh-Ru correlate well (**Fig. 21**), which indicates that the collector was sulfide, which would collect all PGE in more-or-less equal proportions, and not PGE alloys, which would collect some PGE but not all PGE (Farhangi et al., *in prep*). The lack of correlation with S can probably be attributed to variable loss of S, as deduced in many other studies (e.g., Peregoedova et al., 2004; Barnes et al., 2008).

All other parts of UWZ contain only very small amounts of Fe-Ni-Cu-(PGE) sulfides, so it seems likely that the in those areas the UWZ incorporated basal BTIC mineralization. Taken together, this means that the abundant (up to 20%) patchy disseminated to patchy net-textured Fe-Ni-Cu-(PGE) sulfides in the upper and marginal zones of the BLHZ (Northeast, Central and Southwest Brecciated Zones: **Fig. 9**) formed during emplacement of the LWI into the PGE-enriched BLCZ. The segregation of sulfides could have been caused by at least two processes:

- 1) Incorporation of Chr, which contains significant amounts of Fe_2O_3 , would have oxidized the magma; however, there is not much evidence that much Chr was dissolved and this would have also added Fe to the magma, increasing sulfide solubility (see e.g., Haughton et al., 1974; Wendtlandt, 1982; Mavrogenes and O'Neill, 1999).
- 2) Dissolution of trapped silicate melt \pm Ol would have modified the composition of the magma and depending on the abundances of S and the solubility of sulfide for that composition might

have driven the magma to sulfide saturation. The compositions of the LWI magma and the melted components of the BLCZ are not well enough known for us to be able to calculate the solubility of sulfide in the hybrid magma, but the field relationships indicate quite strongly that the Fe-Ni-Cu-(PGE) sulfide mineralization is associated exclusively with BLHZ rocks, so it seems almost certain that it formed during the hybridization process.

There are many examples of sulfide saturation being induced by incorporation of S-rich xenoliths (e.g., Duluth: Ripley, 1986; Samalens et al., 2017); Voisey's Bay: Li and Naldrett, 1999; Lightfoot et al., 2010; Noril'sk: Lightfoot and Keays, 2005), and there are many models for inducing sulfide saturation by "felsification" (e.g., Irvine, 1975; Li and Naldrett, 1993; Lightfoot and Hawkesworth, 1997), but, if the above interpretations are correct, then this is the first example known to us where significant amounts of Fe-Ni-Cu-(PGE) sulfide mineralization have been generated through the interaction of a mafic magma with S-poor ultramafic *cognate* xenoliths.

This occurrence highlights the fundamental problem with models involving derivation of S by mixing more evolved and less evolved magmas or incorporation of more evolved rocks into more primitive magmas: the solubility of S in mafic-ultramafic magmas is very low, always <0.3% (e.g., Shima and Naldrett, 1975) and often <2% (see review by Li and Ripley, 2005) and such a process will not quantitatively remove all of the S, so the amount of S that can be produced will be small, as observed here at the margin of the LWI and others (e.g., River Valley: James et al., 2002).

2.8.5 Emplacement of LWI and genesis of BLHZ

The relative timing of emplacement of the LWI and BTIC MS is not clear. The current U-Pb single zircon TIMS dates are 2733.6 ± 1.0 Ma for the LWI gabbro and 2734.1 ± 0.6 Ma

for MS gabbro (Houlé et al., *in prep*), which are the same within errors. The Upper Zone of the US are composed of Ol websterite and websterite, so they may be related to the LWI, but there is no evidence that the LWI intruded the US, that the Upper Zone of the US intruded the LWI or evidence of any LWI higher in the section, so it seems most likely at this stage that the LWI intruded after the majority of the BTIC and simply did not reach the Upper Zone of the US or BTCZ.

The similar incompatible trace element and REE signatures of the LWI and BTIC (**Figs. 22F and 25**) suggest that they were derived from the same source. Mungall et al. (2010) estimated the parental magma for the Eagle's Nest deposit (5 km SW of BTIC; **Fig. 3**) was a low-Mg komatiite with ~22 wt% MgO; and Carson et al. (2015) inferred that the BTIC was derived from a similar parental magma. Although many of the rocks are ad- to mesocumulates and some diagnostic trace elements scatter because several values trace elements approach their LLDs (**Table 3**), they exhibit no systematic differences between BLHZ, UWZ, or BTIC. All appear to be systematically enriched in HILE and less enriched in Nb-Ta-Ti (**Figs. 22F and 25**), which is a signature of crustal contamination in komatiitic, cumulate rocks (e.g., Lesher and Arndt, 1995; Lesher et al., 2001; Sproule et al., 2002; Layton-Matthews et al., 2003). Some dunitic samples are less enriched in HILE, but this is likely an effect of them containing abundant Ol, which concentrates HREE relative LREE (Arndt and Lesher, 1992).

Extensive (>100m) intervals of clast-free, UWZ occur in the core of the LWI, and the feeder zone contains smaller (>30m) but similar intervals of UWZ. As it intruded, the LWI entrained, disaggregated, and partially assimilated dunite, lherzolite, and chromitite clasts to form homo-heterolithic breccias and heterogeneously hybridized rocks that occur in marginal zones to the UWZ, as isolated pods surrounding stoped blocks, and as hybridized sills associated at the

margins of UWZ sills. Some large (>20m) stoped blocks have layering oriented similar to that in adjacent BTIC indicating they are likely still connected and are not isolated blocks. The UWZ likely propagated as scattered injections of magma between septa of host rock and then grew as individual dikes amalgamated explaining the interdigitation of UWZ dikes, clasts, and juxtaposed zones of hybrid rocks (**Figs. 8 and 10**).

Map- and core-scale cross-cutting relationships indicate that the emplacement of the UWZ involved reactivation of the feeder with diking/silling, stoping, and partial assimilation of BS and US wall rock, but did not cut the Upper Zone of the US or BTCZ (**Fig. 4**). The intrusion may have lost momentum through the injection into the more refractory chromite-rich layers of the BLCZ. The BS is more massive than the US and is more likely to have been consolidated at the time of emplacement of the LWI, so initial reactivation may have involved more diking. The US is more finely layered than the BS and is more likely to have been less consolidated at the time of emplacement of the LWI, so the later stages of emplacement may have involved more semi-conformable silling (**Figs. 9 and 11B**). This is especially apparent at the level of the BLCZ (**Fig. 4**), the magma silled/injected along well-defined bedding planes and into silicate-dominated layers (**Figs. 6F-G**). Further evidence for differences in consolidation is shown in the systematic changes in clast shape (i.e., more abundant rounded clasts in US whereas subangular clasts with associated LWI dikelets in BS).

There are rare zones of chromitite clasts adjacent to the underlying BS (**Fig. 11A**), suggesting that some gravitational settling took place, but most of these features suggest that the clasts remained relatively close to where they were incorporated and did not settle very far. The composition of the magma that crystallized the LWI is not known precisely, but in order to have crystallized (Ol)-Opx-Cpx-Plag it would have been similar in composition to a flood basalt, and

would have had a density of the order of 2.8 g cm^{-3} and a viscosity of the order of 3.1 Pa s . Massive dunite clasts containing Fo_{75} olivine would have had densities of the order of 3.4 g cm^{-3} . Massive chromitite clasts would have had densities of the order of 4.8 g cm^{-3} . Settling velocities would vary with clast sizes, but common $\sim 3 \text{ cm}$ -diameter chromitite clasts should have settled at rates of the order of 150 cm sec^{-1} . This means that the LWI magma must have crystallized more rapidly than the chromite clasts could settle, which is consistent with it crystallizing over a fairly narrow temperature interval along the Opx-Cpx cotectic, near the Opx-Cpx-Plag eutectic.

The small amounts of residual silicate liquid are represented by local feldspathic websterite pods and gabbroic dikes and unlike the BTIC, which appears to have been a more open system and to have accumulated significant amounts of Ol and Chr, the LWI appears to have remained a relatively closed system with $\sim 80\text{-}85\%$ cumulate websterites and hybrid harzburgites, and $\sim 15\text{-}20 \text{ vol}\%$ evolved feldspathic websterites and gabbroic dikes. The LWI appears to be the last phase of magma emplaced into the feeder, as the biotite gabbro is a late, cross-cutting intrusion in the SW of US (**Figs. 3 and 4**).

Based on field, petrographic, and geochemical observations of the emplacement of LWI, the genesis of the BLHZ appears to have been as follows:

- 1) The initial emplacement of the BTIC dated at $\sim 2734 \text{ Ma}$ (Houlé et al., *in prep*) through a lower feeder conduit, and formation of Ol-Chr-Opx cumulate layers (**Fig. 26, T1**).
- 2) Reactivation of BTIC feeder zone by the LWI (**Fig. 26, T2**) along the footwall-BTIC contact, a lithological weakness. The mineralogical composition of the LWI (Opx-Cpx \pm Pl \pm Ol) indicates that it was more evolved than the magma that generated the rocks of the BS, US (Ol-Chr \pm Opx-Cpx), and some of the lower parts of the MS, which suggests fractionation in a deeper chamber or greater assimilation-fractionation as the magma heated up underlying

upper crustal rocks (see discussion by Lesher and Arndt, 1995). (**Fig. 26, T2**). Greenschist facies metamorphism of all rock types, and the presence of overlying volcanic rocks and basement granitoids indicate that this occurred in a shallow, subvolcanic (<3 km) setting in the crust (**Fig. 3**).

Once the LWI magma breached the conduit, it migrated – through a combination of diking, stoping, and bedding-parallel injection – into surrounding lherzolite and dunite rocks of the BS and US. As discussed above, at the time of injection the BTIC appears to have been incompletely crystallized with a hotter, less consolidated core and cooler, more consolidated margins, whereas at the level of the BLCZ the magma silled/injected along well-defined bedding planes and into silicate-dominated layers.

- 3) The LWI emplacement created pervasive breccias the hybrid rocks of BLHZ with 5% exhibiting 5-20% Fe-Ni-Cu-(PGE) sulfide mineralization in three zones (**Figs. 9 and 26, T3**). Mineralization is typically occurring in clast-rich intervals adjacent to the PGE-enriched BLCZ.
- 4) The last stage (**Fig. 26, T4**) involved local fractional crystallization of LWI magma, producing feldspathic websterite and gabbro-norite pods, patches, and veinlets that cross cut UWZ, BLHZ, and BTIC wall rocks.

2.9 Conclusions

- The sizes, shapes, sharpness of margins, and compositions of the clasts appear to have been controlled by the compositions of the lithologies, the thickness of layering, the nature of the contacts between layers, and the initial temperature of the lithologies being incorporated. The margins of clasts vary from sharp to diffuse, and likely depended in part on the nature of the

contact of the original beds. The sizes of clasts vary widely and may correspond to the thickness of the primary bedding. The lithologies of clasts vary greatly, but clast lithology depends locally on the lithology and scale of layering in adjacent wall rocks. The shapes of the clasts vary from subangular to amoeboidal, and show some systematic distribution with location. Systematic variations in clast shape with location suggest that the US were less consolidated (i.e., more rounded clasts), whereas the BS was more consolidated (i.e., more angular clasts).

- Based on meso-microscopic observations the genesis of the BLHZ involved five interdependent assimilative processes: 1) mechanical disaggregation, 2) partial melting of low temperature phases, 3) Ol-Opx reaction-relation, 4) xenocryst re-equilibration, and – very locally – 5) complete dissolution. This resulted in the genesis of two distinct hybrid rock types in the BLHZ: hybrid Chr harzburgite and hybrid harzburgite.
- The whole rock geochemistry of the hybrid rocks is intermediate in composition between websteritic magma, which crystallized Opx + Cpx ± Pl, and BTIC xenoliths, which contain Ol ± Chr ± Opx ± Cpx. This allows the workers to use Ol and Chr contents to estimate the degree of hybridization.
- Intrusion of LWI magma into the BLCZ does not appear to have consumed any of the chromitite, but has locally reduced the grade of the mineralization through dilution and dispersal.
- The strong spatial association of minor Fe-Ni-Cu-(PGE) sulfides with the BLHZ and the absence of significant amounts of sulfides elsewhere (except BTIC basal accumulations)

indicates the LWI transgression into the PGE-rich BLCZ and subsequent hybridization induced sulfide saturation.

- The saturation/segregation of sulfides could have been caused by at least two processes: 1) incorporation of Chr, which contains significant amounts of Fe_2O_3 , would have oxidized the magma, and/or 2) dissolution of trapped silicate melt \pm Ol would have modified the composition of the magma and depending on the abundances of S and the solubility of sulfide for that composition might have driven the magma to sulfide saturation. If the above interpretations are correct, then this is the first example known to us where significant amounts of Fe-Ni-Cu-(PGE) sulfide mineralization have been generated through the interaction of a mafic magma with cognate, S-poor, *ultramafic* xenoliths.
- The similar incompatible trace element and REE signatures of the LWI and BTIC suggest that they were derived from the same source. All appear to be systematically enriched in HILE and less enriched in Nb-Ta-Ti, which is a signature characteristic of crustal contamination in komatiitic, cumulate rocks. Unlike the BTIC, which appears to have been a more open system and to have accumulated significant amounts of Ol + Chr, the LWI appears to have remained a relatively closed system with Opx + Cpx + Pl.
- From map- and core-scale cross-cutting relationships a possible LWI emplacement model can be made: 1) initial emplacement of the BTIC and primary cumulate layers; 2) LWI reactivation of the BTIC feeder, and the diking/silling, stoping and partial assimilation of BS and US wall rocks; 3) formation of homo-heterolithic breccias, heterogeneously hybridized rocks (BLHZ), and associated sulfide mineralization; and 4) local late stage fractional crystallization of LWI magma.

2.10 Acknowledgments

This project was supported by grants from Cliffs Natural Resources Inc. and the Natural Sciences and Engineering Research Council of Canada Collaborative Research and Development program to CML, and a Society of Economic Geologists Fellowship and an Ontario Graduate Scholarship to CSS. Cliffs Natural Resources Inc. provided field and logistical support; and the Ontario Geological Survey and Targeted Geosciences Initiative Program of the Geological Survey of Canada provided analytical support. We are grateful to Richard Fink, Andrew Mitchell, and Michael Orobona (Cliffs); Alan Coutts and Ryan Weston (Noront); Jack Parker (OGS); and Mike Villeneuve (GSC) for their interest in the project. We are grateful to Ryan Weston (Cliffs/Noront) and David Shinkle (Cliffs) for helpful discussions on the geology; Rick Kruse (Cliffs) for GIS assistance; and Daron Slaney, Randy Abraham, and other members of the Cliffs “Esker Camp” crew for logistical support. Riku Metsaranta (OGS) and Valérie Bécu (GSC) provided helpful comments on an interim report.

2.11 References

- Arndt, N., 1986, Differentiation of komatiite flows: *Journal of Petrology*, v. 27, p. 279-301.
- Arndt, N., and Lesher, C.M., 1992, Fractionation of REEs by olivine and the origin of kambalda komatiites, Western Australia: *Geochimica et Cosmochimica Acta*, v. 56, p. 4191-4204.
- Arndt, N., Lesher, C.M., and Barnes, S.J., 2008, *Komatiite*: Cambridge, UK, University Press, 467 p.
- Arculus, R.J., Johnson, R.W., Chappell, B.W., McKee, C.O., and Sakai, H., 1983, Ophiolite-contaminated andesites, trachybasalts, and cognate inclusions of Mount Lamington, Papua New Guinea: anhydrite-amphibole-bearing lavas and the 1951 cumulodome: *Journal of Volcanology and Geothermal Research*, v. 18, p. 215-247.
- Barnes, S.J., 1986, The effect of trapped liquid crystallization on cumulus mineral compositions in layered intrusions: *Contributions to Mineralogy and Petrology*, v. 93, p. 524-531.
- Barnes, S.J., Prichard, H.M., Cox, R.A, Fisher, P.C., and Godel, B., 2008, The location of the chalcophile and siderophile elements in platinum-group element ore deposits (a textural, microbeam and whole rock geochemical study): *Chemical Geology*, v. 248, p. 295-317.
- Beard, J.S., Ragland, P.C., and Crawford, M.L., 2005, Reactive bulk assimilation: A model for crust-mantle mixing in silicic magmas: *Geology*, v. 33, p. 681-684.

- Bédard, J.H., 1991, Cumulate Recycling and Crustal Evolution in the Bay of Islands Ophiolite: *Journal of Geology*, v. 99, p. 225-249.
- Bédard, J.H., 1993, Oceanic crust as a reactive filter: Synkinematic intrusion, hybridization, and assimilation in a ophiolitic magma chamber, western Newfoundland: *Journal of Geology*, v. 21, p. 77-80.
- Bowen, N. L., 1922, The behavior of inclusions in igneous magmas: *Journal of Geology*, v. 30, p. 513-570.
- Burgess, H., Gowans, R., Jacobs, C., Murahwi, C., Damjanović, B., 2012, National Instrument 43-101 Technical Report: feasibility study McFaulds Lake Property Eagle's Nest Project, James Bay Lowlands Ontario, Canada: NTS 43D16 Mineral Resource Estimation Technical Report Prepared For Noront Resources Ltd., 210 p.
- Burnham, O.M., 2008, Trace element analysis of geological samples by inductively coupled plasma mass spectrometry (ICP-MS) at the Geoscience Laboratories: revised capabilities due to method improvements: Summary of Field Work and Other Activities 2008, Ontario Geological Survey, v. 6226, p. 38-1-38-10.
- Burnham, O.M., Hechler, J., and Chrétien, N., 2010, Improvements to the analysis of chromite-rich samples by X-ray fluorescence spectrometry at the Geoscience Laboratories: effect of sample:flux ratios during fused disk preparation: Summary of Field Work and Other Activities 2010, Ontario Geological Survey, v. 6260, p. 41-1-41-6.
- Carson, H.J.E., Leshner, C.M., Houlé, M.G., Weston, R.J., and Shinkle, D.A., 2013, Stratigraphy, geochemistry and petrogenesis of the Black Thor intrusive complex and associated chromium and nickel-copper-platinum group element mineralization, McFaulds Lake greenstone belt, Ontario: Summary of Field Work and Other Activities 2013, Ontario Geological Survey, v. 6290, p. 52-1-52-15.
- Carson, H.J.E., Leshner, C.M., and Houlé, M.G., 2015, Geochemistry and petrogenesis of the Black Thor intrusive complex and associated chromite mineralization, McFaulds Lake greenstone belt, Ontario: Targeted Geoscience Initiative 4, Geological Survey of Canada, v. 7856, p. 87-102.
- Clarke, D.B., Henry, A.S., and White, M.A., 1998, Exploding xenoliths and the absence of "elephants graveyards" in granite batholiths: *Journal of Structural Geology*, v. 20, p. 1325-1343.
- Clarke, D.B., 2007, Assimilation of xenocrysts in granitic magmas; principles, processes, proxies, and problems: *Canadian Mineralogist*, v. 45, p. 5-30.
- Donaldson, M.J., Leshner, C.M., Groves, D.I., and Gresham, J.J., 1986, Comparison of Archean dunites and komatiites associated with nickel mineralisation in Western Australia: implications for dunite genesis: *Mineralium Deposita*, v. 21, p. 296-305.
- Droop, G.T.R., 1987, A general equation for estimating Fe³⁺ concentrations in ferromagnesian silicates and oxides from microprobe analyses, using stoichiometric criteria: *Mineralogical Magazine*, v. 51, p. 431-435.
- Dungan, M.A., and Davidson, J., 2004, Partial assimilative recycling of the mafic plutonic roots of arc volcanoes: An example from the Chilean Andes: *Geology*, v. 9, p. 773-776.
- Erdmann, S., Scaillet, B., Kellett, D.A., 2010, Xenocryst assimilation and formation of peritectic crystals during magma contamination: An experimental study: *Journal of Volcanology and Geothermal Research*, v. 198, p. 355-367.

- Farhangi, N., Leshner, C.M., and Houlié, M.G., 2013, Mineralogy, geochemistry and petrogenesis of nickel-copper-platinum group element mineralization in the Black Thor intrusive complex, McFaulds Lake greenstone belt, Ontario: Ontario Geological Survey, v. 6290, p. 55-1-55-7.
- Glazner, A.F., Farmer, G.L., Hughes, W.T., Wooden, J.L., and Pickthorn, W., 1991, Contamination of basaltic magma by mafic crust at Amboy and Pisgah Craters, Mojave Desert, California: *Journal of Geophysical Research*, v. 96, p. 13673-13691.
- Glazner, A.F., 2007, Thermal limitations on incorporation of wall rock into magma: *Geology*, v. 35, p. 319-322.
- Houghton, D.R., Roeder, P.L., and Skinner, B.J., 1974, Solubility of sulfur in mafic magmas: *Economic Geology*, v. 69, p. 451-467.
- Houlié, M.G., Leshner, C.M., Schetselaar, E., Metsaranta, R.T., and McNicoll, V., 2017, Architecture of magmatic conduits in Cr-PGE/Ni-Cu-PGE Ore Systems, in Rogers, N., ed., TGI Phase 5: Ore systems from source to deposit – 2016 Activity Report and Synthesis: Geological Survey of Canada Open File 8199, p. 55-58.
- Huber, C., Bachmann, O., and Dufek, J., 2010, Thermo-mechanical reactivation of locked crystal mushes: Melting-induced internal fracturing and assimilation processes in magmas: *Earth and Planetary Science Letters*, v. 304, p. 443-454.
- Irvine, T.N., 1975, Crystallization sequences of the Muskox Intrusion and other layered intrusions: II. Origin of the chromitite layers and similar deposits of other magmatic ores: *Geochimica et Cosmochimica Acta*, v. 39, p. 991-1020.
- James, R.S., Easton, R.M., Peck, D.C., and Hrominchuk, J.L., 2002, The East Bull Lake Intrusive Suite: remnants of a ~2.48 Ga large igneous and metallogenic province in the Sudbury area of the Canadian Shield: *Economic Geology*, v. 97, p. 1577-1606.
- Kelemen, P.B., 1986, Assimilation of ultramafic rock in subduction-related magmatic arcs: *Journal of Geology*, v. 94, p. 829-843.
- Kelemen, P.B., and Ghiorso, M.S., 1986, Assimilation of peridotite in calc-alkaline plutonic complexes: evidence from the Big Jim complex, Washington Cascades: *Contributions to Mineralogy and Petrology*, v. 94, p. 12-28.
- Klügel, A., 1998, Reactions between mantle xenoliths and host magma beneath La Palma (Canary Islands): constraints on magma ascent rates and crustal reservoirs: *Contributions to Mineralogy and Petrology*, v. 131, p. 237-257.
- Kuzmich, B., Hollings, P., and Houlié, M.G., 2015, Petrogenesis of the ferrogabbroic intrusions and associated Fe-Ti-V-(P) mineralization within the McFaulds greenstone belt, Superior Province, northern Ontario: Targeted Geoscience Initiative 4, Geological Survey of Canada, v. 7856, p. 115-123.
- Layton-Matthews, D., Burnham, O.M., and Leshner, C.M., 2003, Trace element geochemistry of ultramafic intrusions in the Thompson Nickel Belt: relative roles of contamination and metasomatism: *The Gangue*, Geological Survey of Canada, v. 76, p. 1-9.
- Le Maitre, R.W. (Ed.), Streckeisen, H., Zanettin, B., Le Bas, M.J., Bonin, B., Bateman, P., Bellieni, G., Efremova, S., Dudek, A., Keller, J., Lameyre, J., Sabine, P.A., Schmid, R., Sorensen, A., and Woolley, A.R., 2002, *Igneous Rocks: A Classification and Glossary of Terms*: New York, Cambridge, 256 p.

- Leshner, C.E., 1990, Decoupling of chemical and isotopic exchange during magma mixing: *Nature*, v. 344, p. 235-237.
- Leshner, C.M., 1989, Komatiite-associated nickel sulfide deposits, in Whitney, J.A, and Naldrett, A.J., ed., *Ore deposition associated with magmas: El Paso, The Economic Geology Publishing Company*, p. 45-101.
- Leshner, C.M., Burnham, O.M., and Keays, R.R., 2001, Trace-element geochemistry and petrogenesis of barren and ore-associated komatiites: *Canadian Mineralogist*, v. 39, p. 673-696.
- Leshner, C.M., and Arndt, N.T., 1995, 'REE and Nd isotope geochemistry, petrogenesis and volcanic evolution of contaminated komatiites at Kambalda, Western Australia: *Lithos*, v. 34, p. 127-157.
- Li, C., and Naldrett, A.J., 1993, Sulfide capacity of magma: a quantitative model and its application to the formation of sulfide ores at Sudbury, Ontario: *Economic Geology*, v. 88, p. 1253–1260.
- Li, C., and Naldrett, A.J., 1999, Geology and petrology of the Voisey's Bay intrusion: reaction of olivine with sulfide and silicate liquids: *Lithos*, v. 47, p. 1-31.
- Lightfoot, P.C., and Keays, R.R., 2005, Siderophile and chalcophile metal variations in flood basalts from the Siberian Trap, Noril'sk region: implications for the origin of the Ni-Cu-PGE sulfide ores: *Economic Geology*, v. 100, p. 439-462.
- Lightfoot, P.C., Keays, R.R., Evans-Lamswood, D., and Wheeler, R., 2010, S-saturation history of Nain Plutonic Suite mafic intrusions: origin of the Voisey's Bay deposit, Labrador, Canada: *Mineralium Deposita*, v. 47, p. 23-50.
- Lightfoot, P.C., and Hawkesworth, C.J., 1997, Flood basalts and magmatic Ni, Cu, and PGE sulphide mineralization: comparative geochemistry of the Noril'sk (Siberian Traps) and West Greenland sequences, in Mahoney, J.J., and Coffin, M.F., ed., *Large igneous provinces: American Geophysical Union Monograph*, p. 357–380.
- Lindsley, D.H., 1983, Pyroxene thermometry: *American Mineralogist*, v. 68, p. 477-493.
- Mavrogenes, J.A., and O'Neill, H.S.C., 1999, The relative effects of pressure, temperature and oxygen fugacity on the solubility of sulfide in mafic magmas: *Geochimica et Cosmochimica Acta*, v. 63, p. 1173–1180.
- Maury, R.C., and Didier, J., 1991, Xenoliths and the role of assimilation, in Didier, J., and Barbarin, B, ed., *Enclaves and Granite Petrology: New York, Elsevier*, p. 265-275.
- McDonough W.F., and Sun S.S., 1995, Composition of the Earth: *Chemical Geology*, v. 120, p. 223–253.
- McLeod, P., and Sparks, R.S.J, 1998, The dynamics of xenolith assimilation: *Contributions to Mineralogy and Petrology*, v. 132, p. 21-33.
- Mehrmanesh, K., Carson, H.J.E., Leshner, C.M., and Houllé, M.G., 2013, Stratigraphy, geochemistry and petrogenesis of the Black Label chromite horizon, Black Thor intrusive complex, McFaulds Lake greenstone belt, Ontario: Summary of field work and other activities 2013, Ontario Geological Survey, v. 6290, p. 53.1—53.6.
- Metsaranta, R.T., Houllé, M.G., McNicoll, V.J., and Kamo, S.L., 2015, Revised geological framework for the McFaulds Lake greenstone belt, Ontario: Targeted Geoscience Initiative 4, Geological Survey of Canada, v. 7856, p. 61-73.

- Metsaranta, R.T., and Houlé, M.G., 2017, Precambrian geology of the McFaulds Lake area, “Ring of Fire” region, Ontario— central sheet: Ontario Geological Survey, Preliminary Map P .3805; Geological Survey of Canada, Open File 8201.
- Mungall, J.E., Harvey, J.D., Balch, S.J., Azar, B., Atkinson, J., and Hamilton, M. A., 2010, Eagle’s Nest: The discovery and geology of a magmatic Ni-sulfide deposit under overburden in the James Bay Lowlands of Ontario, Canada: *Economic Geology*, Special Publication, v. 15, p. 539–557.
- Pearson, D.G., Canil, D., and Shirey, S.B., 2003, Mantle samples included in volcanic rocks: xenoliths and diamonds, Carlson, R.W., Holland, H.D., and Turekian, K.K., ed., *Treatise on Geochemistry*: Oxford, Elsevier-Pergamon, v. 2, p. 171-275.
- Peregoedova, A., Barnes, S.J., and Baker, D.R., 2004, The formation of Pt–Ir alloys and Cu–Pd-rich sulfide melts by partial desulfurization of Fe–Ni–Cu sulfides: results of experiments and implications for natural systems: *Chemical Geology*, v. 208, p. 247-264.
- Perugini, D., and Poli, G., 2012, The mixing of magmas in plutonic and volcanic environments: Analogies and differences: *Lithos*, v. 153, p. 261-277.
- Rayner, N., and Stott, G.M., 2005, Discrimination of Archean domains in the Sachigo subprovince: A progress report on the geochronology: Summary of Field Work and Other Activities 2005, Ontario Geological Survey, v. 6172, p. 10-1–10-21.
- Ripley, E.M., 1986, Origin and concentration mechanisms of copper and nickel in Duluth Complex sulfide zones—a dilemma: *Economic Geology*, v. 81, p. 974-978.
- Rollinson, H., 1993, *Using geochemical data: evaluation, presentation, interpretation*: London, Longman, 352 p.
- Rose, L.A., and Brenan, J.M., 2001, Wetting properties of Fe-Ni-Co-Cu-O-S melts against olivine: implications for Sulfide Melt Mobility: *Economic Geology* 2001 96:145-157.
- Rudnick, R.L., and Fountain, D.M., 1995, Nature and composition of the continental crust—a lower crustal perspective: *Reviews of Geophysics*, v. 33, p. 267–309.
- Rudnick, R.L., and Gao, S., 2003, Composition of the continental crust, in Rudnick, R.L., Holland, H.D., and Turekian, K.K., ed., *Treatise on Geochemistry*: Oxford, Elsevier-Pergamon, v. 3, p. 593–659.
- Samalens, N., Barnes, S-J., and Sawyer, E.W., 2017, The role of black shales as a source of sulfur and semimetals in magmatic nickel-copper deposits: Example from the Partridge River Intrusion, Duluth Complex, Minnesota, USA: *Ore Geology Reviews*, v. 81, p. 173-187.
- Schulte, R.F., Taylor, R.D., Piatak, N.M., and Seal II, R.S., 2012, Stratiform chromite deposit model, chap. E of Mineral deposit models for resource assessment: U.S. Geological Survey Scientific Investigations Report 2010–5070, 131 p.
- Shima, H., and Naldrett, A.J., 1975, Solubility of sulfur in an ultramafic melt and the relevance of the system Fe-S-O: *Economic Geology*, v. 70, p. 960-967.
- Spandler, C., O’Neill, C., and Kamenetsky, V.S., 2007, Survival times of anomalous melt inclusions from element diffusion in olivine and chromite: *Nature*, v. 447, p. 303-306.
- Sparks, R.S.J., and Marshall, L.A., 1985, Thermal and mechanical constraints on mixing between mafic and silicic magmas: *Journal of Volcanology and Geothermal Research*, v. 29, p. 99-124.

- Spath III, C.S., Leshner, C.M., and Houlié, M.G., 2015, Hybridized ultramafic rocks in the Black Label hybrid zone of the Black Thor intrusive complex, McFaulds Lake greenstone belt, Ontario: Targeted Geoscience Initiative 4, Geological Survey of Canada, v. 7856, p. 103-114.
- Sproule, R.A., Leshner, C.M., Ayer, J.A., Thurston, P.C., and Herzberg, C.T., 2002, Spatial and temporal variations in the geochemistry of komatiites and komatiitic basalts in the Abitibi greenstone belt: *Precambrian Research*, v. 115, p. 153–186.
- Stott, G.M., Corkery, M.T., Percival, J.A., Simard, M., and Goutier, J., 2010, A revised terrane subdivision of the Superior Province: Summary of Field Work and Other Activities 2010, Ontario Geological Survey, v. 6260, p. 20-1—20-10.
- McDonough, W.F., and Sun, S.S., 1989, Chemical and isotopic systematics of oceanic basalts: implications for mantle composition and processes: Geological Society London Special Publication, v. 42, p. 313–345.
- Tuchscherer, M.G., Hoy, D., Johnson, M., Shinkle, D., Kruze, R., and Holmes, M., 2009, Fall 2008 to winter 2009 technical drill report on the Black Thor Chromite Deposit, Black Label Chromite Deposit, and associated Ni-Cu-PGEs McFaulds property, James Bay Lowlands, Northern Ontario: Freewest Resources Canada Inc., 48 p.
- Wendtlandt, R.F., 1982, Sulfide saturation of basalt and andesite melts at high pressures and temperatures: *American Mineralogist*, v. 67, p. 877-885.
- Weston, R., and Shinkle, D.A., 2013, Geology and stratigraphy of the Black Thor and Black Label chromite deposits, James Bay Lowlands, Ontario, Canada; [ext. abs.]: Society for Geology Applied to Minerals, 12th, Uppsala, Sweden, 2013, Proceedings, v. 3, p. 1069-1071.
- Zuccarelli, N., Leshner, C.M., Houlié, M.G., and Weston, R., 2017, Sulfide textural variations and multiphase ore emplacement in the Eagle’s Nest Ni-Cu-PGE deposit, McFaulds Lake greenstone belt, Ontario, Canada; [abs.]: Proceeding of the Biennial SGA Meeting, 14th, Quebec City, Canada, p. XXXX-XXXX.

2.12 Table Captions

Table 1. Petrographic features of BTIC clasts. Increasing modal abundance of Chr toward bottom. Cumulate phase: O and C= olivine and chromite respectively; Cumulate texture: hac=heteradcumulate, ac=adcumulate, mc=mesocumulate, oc=orthocumulate. Grain size: vfg, fg, mg, cg, vcg = very fine, fine, medium, coarse, very coarse-grained; bi=bimodal. For mineral abbreviations see Figure 12 and 13. Alteration mineralogy after Carson et al. (2015).

Table 2. Representative electron microprobe (wavelength dispersive spectrometry) analyses of minerals from the UWZ, BLHZ, and BTIC clasts. Abbreviations are the same as Table 1 and the order is consistent for comparison, with more mafic minerals at left. Mineral modal abundance in text. N/A designates that oxide was not analyzed in mineral. FeO* total Fe expressed as FeO. See Appendix A for lower limit of detection (LLD), precision and accuracy values. Chr structural formulae are calculated using the method of Droop (1987).

Table 3. Table 3: Ranges, averages and standard deviations for whole-rock geochemical analyses of selected lithologies from the UWZ, HWZ and BTIC rocks.. Fsp=Feldspathic, Ol=Olivine, Chr=Chromite, Txt=Textured. Samples taken from this study, ¹Carson et al., *in prep* and ²Mehrmanesh et al., *in prep*.

Table 1: Petrographic features of Black Thor Intrusive Complex clasts within the UWZ and BLHZ

Lithology	Chromite			Mineralogy	Alteration	Description	
	Color	Modal %	Texture				
Dunite	dark grey, green	0-10%	Oac	fg-eg	Ol (90-98%)-Opx-Chr	Antigorite/lizardite + talc + magnetite ± iowaite/iddingsite	Cumulus Ol ± Chr with intercumulus Opx; fg-mg Ol but also eg (up to 9 mm), fg-mg Opx, and vf-eg Chr (Figs 14E-F and 15G); typically exhibits more rounded shapes than chromitite clasts.
Herzoltite	dark grey-green	0-10%	Omc to Ooc	fg-eg	Ol (40-90%)-Opx-Cpx-Chr	Actinolite + (magneso)-hornblende + chlorite	Cumulus Ol and Chr with intercumulus Opx/Cpx; fg-mg Ol, mg-eg Opx; locally oikocrystic Herzoltite with >30 % eg lensoidal Opx. (Fig. 15E). Most common clast in BLHZ.
Heavy disseminated to net-textured chromitite	dark grey-green	10-50%	OChac to OCoc	bi	1) Chr-Ol/Opx 2) Chr-Cpx +/- Ol/Opx	Antigorite/lizardite + talc + kámmereerite + magnetite ± magnesite	Ol, Chr, Opx cumulus with Cpx intercumulus; fg Chr, mg Ol and Opx, and eg-veg Cpx; Refractory chromitite inclusions typically exhibit more angular shapes. Chr occurs either: 1) locally within interstices of cumulus Ol and/or Opx (i.e., net-texture); 2) patchy disseminated within oikocrystic Cpx with minor cumulus Ol/Opx. (Fig. 15F)
Matrix to semimassive chromitite	dark grey	50-90%	OChac to OCoc	bi	1) Chr-Ol/Opx 2) Chr-Cpx +/- Ol/Opx	Same as above	Same description as heavy disseminated to net-textured chromitite. Most common <i>chromitite</i> inclusion in BLHZ (Fig. 15C).
Massive chromitite	black	90-98%	OChac	vf-eg	Chr +/- (Ol/Opx/Cpx)	Same as above	Cumulus Chr, with minor cumulus Ol, Opx, and intercumulus Cpx; fg Chr, mg Ol and Opx, and eg-veg Cpx; Massive chromitite occurs with either: a) round aggregates of Ol/Opx; b) mono- to polymineralic layering (<1 cm thickness) of Ol/Opx (Fig. 15H); c) negligible intercumulus Cpx phase (Fig. 15D-E);

Table 2: Representative electron microprobe analyses of minerals from BTIC clast, UWZ and BLHZ lithologies

Lithology	LWI Websterite			LWI Fsp Websterite			LWI Gabbroiorite			BLHZ Harzburgite			BLHZ Chromite			BLCZ Semi-Mass Chrnrt			Dunite Clast																											
	Sample Loc.	OI	Opx	Cpx	Pl	Opx	Cpx	Pl	Opx	Cpx	Pl	OI	Opx	Cpx	Chr	OI	Opx	Cpx	OI	Opx																										
SiO ₂	BT-11-180/171	BT-09-34/121	BT-09-32/119	BT-11-179/87	BT-11-177/108	BT-11-182/276	BT-11-199A/46	38.8	55.0	52.0	46.4	55.4	52.0	47.6	54.4	51.9	48.9	39.5	55.9	52.7	0.11	40.0	54.9	52.2	<0.006	40.5	56.2	53.2	40.4	56.2																
TiO ₂								<0.007	0.08	0.24	0.01	0.07	0.27	0.01	0.12	0.20	0.01	<0.007	0.09	0.22	0.89	<0.007	0.10	0.22	0.8	<0.007	0.08	0.14	<0.007	0.05																
Al ₂ O ₃								<0.006	1.49	2.83	33.5	1.25	3.09	32.6	1.79	2.90	31.8	<0.006	1.53	2.69	17.6	<0.006	1.64	2.69	15.9	0.01	1.59	1.99	<0.006	1.37																
V ₂ O ₅								N/A	N/A	N/A	N/A	N/A	N/A	N/A	N/A	N/A	N/A	N/A	N/A	N/A	0.23	N/A	N/A	N/A	0.2	N/A	N/A	N/A	N/A	N/A																
Cr ₂ O ₃								<0.01	0.49	0.89	N/A	0.42	0.96	N/A	0.56	0.96	N/A	0.01	0.41	0.90	41.0	<0.01	0.46	1.05	45.7	0.02	0.57	1.07	0.02	0.32																
FeO								20.4	10.9	5.46	0.26	11.7	5.47	0.36	12.1	5.83	0.27	14.8	9.45	4.16	24.8	13.7	10.3	4.57	20.2	11.7	8.19	3.18	13.0	8.47																
MnO								0.27	0.27	0.17	<0.03	0.26	0.17	<0.03	0.28	0.18	0.01	0.23	0.25	0.15	0.33	0.21	0.25	0.16	0.3	0.18	0.22	0.11	0.21	0.22																
CoO								0.03	<0.01	<0.01	N/A	0.01	<0.01	N/A	<0.01	0.01	N/A	0.03	0.01	<0.01	0.03	0.02	<0.01	<0.01	0.03	0.03	0.01	<0.01	0.02	<0.01																
NiO								0.22	0.02	0.03	N/A	0.06	0.01	N/A	0.05	0.04	N/A	0.19	0.05	0.03	0.03	0.17	0.05	0.02	0.04	0.27	0.06	0.03	0.03	0.26	0.07															
ZnO								N/A	N/A	N/A	N/A	N/A	N/A	N/A	N/A	N/A	N/A	N/A	N/A	N/A	0.09	N/A	N/A	N/A	0.07	N/A	N/A	N/A	N/A	N/A																
MgO								40.5	29.6	15.9	0.05	29.9	16.3	0.03	28.6	16.9	0.02	44.6	31.4	16.4	6.96	45.7	30.7	16.8	9.43	47.7	32.2	17.5	46.5	32.4																
CaO								0.03	2.04	22.0	17.3	1.27	21.4	16.3	2.15	20.3	15.3	0.02	1.00	22.5	N/A	0.02	1.29	22.0	N/A	0.03	1.41	22.3	0.01	0.82																
SiO								N/A	N/A	N/A	<0.16	N/A	N/A	<0.16	N/A	N/A	<0.16	N/A	N/A	N/A	N/A	N/A	N/A	N/A	N/A	N/A	N/A	N/A	N/A	N/A	N/A															
Na ₂ O								<0.005	0.02	0.39	1.75	0.02	0.37	2.31	0.04	0.30	2.93	<0.005	0.03	0.41	N/A	<0.005	<0.005	0.3	N/A	<0.005	0.03	0.31	<0.005	<0.005																
K ₂ O								<0.012	<0.005	0.01	0.04	<0.005	<0.005	0.04	<0.005	<0.005	0.05	<0.012	<0.005	<0.005	N/A	<0.012	<0.005	<0.005	N/A	<0.012	<0.005	<0.005	<0.012	<0.005																
Total	100.26	99.92	99.98	99.33	100.38	99.92	99.25	100.12	99.40	99.23	99.26	100.06	100.12	99.82	99.73	99.74	99.93	99.57	100.41	100.48	99.82	100.28	99.88	100.26	99.92	99.98	99.33	100.38	99.92	99.25	100.12	99.40	99.23	99.26	100.06	100.12	99.82	99.73	99.74	99.93	99.57	100.41	100.48	99.82	100.28	99.88
Mg*,Fe,An	60.6	73.1	74.5	87.4	71.9	74.8	82.9	70.2	74.3	77.9	70.1	76.9	79.8	N/A	72.2	74.9	78.6	N/A	76.0	87.7	84.6	73.6	79.2	60.6	73.1	74.5	87.4	71.9	74.8	82.9	70.2	74.3	77.9	70.1	76.9	79.8	N/A	76.0	87.7	84.6	73.6	79.2				

Table 2.

Lithology	LLD	Unhybridized Websterite Zone				Hybridized Websterite Zone				Black Thor Intrusive Complex Proper											
		Websterite		Fsp Websterite		Harzburgite		OI Websterite		Dunite		Lherzoltite		OI		Massive Chromitite		Matrix Txt-Chromitite		Net Txt-Chromitite	
		Websterite	Websterite	Websterite	norite	Harzburgite	Websterite	Harzburgite	Websterite	Chromitite	Chromitite	Chromitite	Pyroxenite	Chromitite	Chromitite	Chromitite	Chromitite	Chromitite	Chromitite	Chromitite	
Major Elements (wt. %)		n=9	n=5	n=4	n=9	n=8	n=4	n=4	n=18 ¹²	n=11 ¹²	n=2 ¹	n=9 ²	n=10 ²	n=7 ²							
SiO₂	<i>Min-Max</i> <i>Avg(StD)</i>	50.5-54.0 52.2 (1.21)	51.8-53.3 52.7 (0.68)	51.1-55.2 52.8 (1.72)	41.1-50.8 44.5 (3.09)	45.3-52.3 48.1 (2.76)	30.4-45.2 37.6 (6.85)	22.4-31.6 27.2 (4.69)	38.5-45.2 42.1 (1.66)	42.2-48.4 44.3 (1.66)	49.5-55.5 52.5 (4.28)	3.86-16.9 9.40 (4.47)	14.5-23.5 17.8 (2.51)	21.7-33.8 28.0 (4.10)							
TiO₂	<i>Min-Max</i> <i>Avg(StD)</i>	0.08-0.16 0.13 (0.02)	0.11-0.34 0.21 (0.09)	0.26-0.38 0.33 (0.06)	0.08-0.28 0.15 (0.06)	0.10-0.24 0.15 (0.05)	0.21-0.37 0.30 (0.06)	0.45-0.50 0.47 (0.02)	0.05-0.19 0.09 (0.04)	0.06-0.15 0.11 (0.02)	0.10-0.10 0.10 (0.00)	0.29-0.41 0.34 (0.03)	0.30-0.58 0.41 (0.11)	0.19-0.76 0.41 (0.15)							
Al₂O₃	<i>Min-Max</i> <i>Avg(StD)</i>	2.88-5.82 4.89 (1.16)	4.03-10.4 7.72 (2.66)	9.08-18.3 12.3 (4.08)	2.11-5.24 3.89 (1.13)	1.77-5.78 3.91 (1.42)	5.26-7.65 6.36 (1.10)	9.09-10.7 9.91 (0.74)	0.94-4.46 2.01 (0.86)	1.04-4.16 2.47 (0.94)	2.30-3.00 2.60 (0.47)	12.8-16.6 14.3 (1.36)	9.07-14.5 11.7 (2.08)	5.85-11.3 9.36 (2.01)							
Cr₂O₃	<i>Min-Max</i> <i>Avg(StD)</i>	0.33-1.26 0.63 (0.29)	0.24-0.42 0.36 (0.08)	0.11-0.64 0.39 (0.24)	0.43-4.64 1.83 (1.38)	0.37-2.16 1.18 (0.64)	6.52-15.2 10.9 (4.46)	16.0-24.2 20.3 (4.08)	0.64-4.75 1.64 (1.23)	0.46-2.17 0.97 (0.54)	0.70-1.70 1.20 (0.71)	33.1-44.0 38.2 (4.73)	26.4-30.8 29.4 (1.42)	14.5-24.3 19.6 (3.42)							
FeOT	<i>Min-Max</i> <i>Avg(StD)</i>	7.83-12.5 10.8 (1.66)	7.91-10.8 8.98 (1.35)	4.27-8.40 7.23 (1.98)	10.1-13.8 12.5 (1.25)	9.33-15.1 13.1 (1.84)	14.4-19.5 16.8 (2.56)	19.7-25.2 21.6 (2.46)	11.1-18.1 13.7 (1.71)	9.93-14.9 12.9 (1.76)	10.4-11.2 10.8 (0.54)	18.1-25.3 21.8 (2.56)	17.6-27.6 23.1 (3.53)	15.4-25.2 20.1 (2.59)							
MgO	<i>Min-Max</i> <i>Avg(StD)</i>	20.6-30.2 26.3 (2.97)	16.4-28.3 20.8 (5.21)	11.2-18.0 15.4 (2.95)	33.0-41.5 36.1 (3.15)	29.7-32.7 31.4 (0.94)	25.3-29.3 26.6 (1.85)	16.2-21.0 18.6 (2.23)	32.4-44.1 40.8 (2.87)	34.8-41.3 38.4 (2.42)	29.8-33.5 31.7 (2.66)	15.4-19.3 16.9 (1.41)	15.2-22.1 18.3 (2.49)	16.3-25.7 21.1 (3.31)							
CaO	<i>Min-Max</i> <i>Avg(StD)</i>	3.17-12.3 5.36 (2.92)	3.30-12.4 9.02 (4.22)	7.35-11.6 9.77 (1.87)	0.36-3.81 2.06 (1.34)	2.02-5.03 3.37 (0.91)	2.07-3.23 2.66 (0.55)	2.21-5.95 3.42 (1.74)	0.01-4.25 0.63 (1.13)	0.71-2.89 1.43 (0.83)	1.90-1.90 1.90 (0.01)	0.08-2.04 0.65 (0.67)	0.03-3.53 1.15 (1.21)	0.15-5.14 2.80 (2.21)							
NiO	<i>Min-Max</i> <i>Avg(StD)</i>	0.04-0.20 0.07 (0.05)	0.02-0.09 0.06 (0.02)	0.02-0.05 0.04 (0.01)	0.10-0.30 0.20 (0.06)	0.07-0.36 0.16 (0.09)	0.12-0.20 0.16 (0.03)	0.06-0.56 0.22 (0.22)	0.01-0.40 0.20 (0.12)	0.01-0.39 0.18 (0.12)	0.10-0.10 0.10 (0.01)	0.05-0.25 0.11 (0.06)	0.09-0.22 0.16 (0.04)	0.03-0.41 0.22 (0.13)							
Na₂O	<i>Min-Max</i> <i>Avg(StD)</i>	0.13-0.54 0.36 (0.16)	0.39-1.10 0.70 (0.32)	1.59-2.03 1.80 (0.19)	0.02-0.52 0.14 (0.18)	0.02-0.42 0.19 (0.13)	0.03-0.06 0.05 (0.01)	0.03-0.33 0.11 (0.15)	0.02-0.03 0.025 (0.01)	<0.02-0.46 0.09 (0.13)	0.21-0.40 0.30 (0.01)	<0.02-0.08 0.03 (0.02)	<0.02-0.21 0.05 (0.06)	0.02-0.17 0.12 (0.11)							
S	<i>Min-Max</i> <i>Avg(StD)</i>	0.03-1.02 0.19 (0.34)	0.01-0.57 0.20 (0.24)	0.02-0.05 0.04 (0.01)	0.10-1.27 0.36 (0.39)	0.03-1.68 0.42 (0.54)	0.12-1.34 0.57 (0.53)	0.65-1.73 1.15 (0.48)	0.01-2.24 0.39 (0.53)	0.03-1.06 0.33 (0.39)	<0.003-0.40 0.20 (0.26)	0.03-0.15 0.09 (0.04)	0.04-0.95 0.40 (0.31)	0.06-1.40 0.64 (0.47)							
LOI	<i>Min-Max</i> <i>Avg(StD)</i>	0.54-3.84 1.63 (1.14)	0.69-2.49 1.79 (0.87)	1.51-3.31 2.21 (0.77)	6.05-14.7 9.84 (2.98)	2.48-7.53 5.81 (1.52)	4.03-6.65 5.29 (1.13)	1.03-3.09 1.93 (0.85)	9.25-15.0 12.9 (1.51)	8.28-13.8 10.8 (1.81)	6.80-10.7 8.70 (2.76)	<0.05-2.93 1.38 (1.14)	0.55-3.99 2.75 (1.28)	<0.05-5.67 3.44 (2.31)							
Mg#	<i>Min-Max</i> <i>Avg(StD)</i>	66.4-75.9 70.8 (3.43)	66.4-72.4 69.5 (3.08)	66.5-72.4 68.5 (2.74)	71.0-79.6 74.3 (2.54)	66.3-77.4 70.7 (3.41)	57.5-67.1 61.4 (4.53)	40.7-50.8 46.2 (4.35)	68.4-79.7 74.9 (3.12)	73.2-79.7 74.8 (30.1)	74.0-75.0 74.5 (0.64)	39.5-48.3 43.7 (3.28)	37.3-55.7 44.3 (5.89)	44.3-60.3 51.1 (4.91)							

Table 3.

Select Trace Elements (ppm)	LLD	Websterite	Fsp Websterite	Gabbro	Harzburgite	O1 Websterite	Chr Harzburgite	Chr O1 Websterite	Dunite	Lherzofite	O1 Pyroxenite	Massive Chromitite	Matrix Txt-Chromitite	Net Txt-Chromitite
Cs Mtn-Max Avg(SD)	0.013	<0.013-0.44 0.14 (0.13)	0.04±0.23 0.15 (0.07)	<0.013-0.42 0.27 (0.13)	0.04±0.32 0.17 (0.10)	0.07±0.36 0.19 (0.09)	0.09±0.27 0.15 (0.08)	0.09±0.23 0.15 (0.05)	<0.013-0.19 0.03 (0.04)	<0.02±0.16 0.07 (0.05)	<0.013-0.10 0 (0.01)	<0.013-1.30 0.28 (0.49)	<0.013-0.45 0.12 (0.15)	0.02±0.41 0.12 (0.12)
Rb Mtn-Max Avg(SD)	0.11	0.49-10.81 3.75 (3.27)	2.99±6.67 5.01±25.4	5.01±25.4 13.0 (9.07)	0.44±10.6 3.65 (3.33)	0.82±4.94 2.47 (1.49)	1.33±2.36 2.01 (0.46)	1.22±7.01 3.57 (2.49)	0.27±10.5 1.13 (2.41)	<0.56±2.37 0.99 (0.66)	0.50±0.70 0.60 (0.11)	1.11±58.7 1.11±58.7	0.77±17.0 3.97 (5.26)	0.68±14.03 3.43 (4.36)
Sr Mtn-Max Avg(SD)	0.6	7.10-50.2 24.2 (14.2)	5.44±7.67 58.2 (23.6)	13.1±39.4 227 (115)	2.68±25.6 10.6 (9.93)	3.81±38.8 15.2 (10.0)	5.05±8.85 6.93 (1.90)	5.03±18.5 10.2 (6.22)	<0.69±10.8 2.08 (3.27)	<3.3±55.4 12.3 (16.1)	10.7±12.0 11.3 (0.91)	3.2±15.3 7.89 (3.81)	2.87±26.2 9.79 (7.03)	1.71±23.8 11.33 (9.17)
Cd Mtn-Max Avg(SD)	0.013	0.02±0.27 0.11 (0.08)	0.04±0.58 0.22 (0.25)	0.05±2.91 0.83 (1.38)	0.02±1.57 0.45 (0.62)	0.03±2.72 0.36 (0.88)	0.03±0.10 0.05 (0.03)	0.03±0.08 0.05 (0.02)	<0.013-0.71 0.06 (0.16)	<0.02±0.18 0.06 (0.05)	<0.013-0.01 0.01 (0.00)	<0.013-1.44 0.22 (0.53)	<0.013-0.03 0.02 (0.01)	<0.013-0.10 0.05 (0.03)
Cu Mtn-Max Avg(SD)	1.4	14.0-73.1 136 (242)	18.6±76.7 396 (376)	17.3±33.9 134 (141)	<1.4±84.1 261 (280)	23.4±11.91 366 (457)	106±120.4 533 (473)	418±145.0 931 (446)	1.61±70.7 60.3 (17.0)	1.70±87.8 126 (260)	3.00±29.8 151 (208)	20.7±28.4 90.3 (87.8)	33.7±31.46 638 (986)	51.5±109.4 561 (463)
Sn Mtn-Max Avg(SD)	0.16	<0.16-0.41 0.16 (0.1)	<0.16-0.71 0.29 (0.27)	<0.16-0.87 0.60 (0.34)	<0.16-0.34 0.18 (0.09)	<0.16-0.22 0.15 (0.04)	<0.16 n.d.	<0.16±0.26 0.19 (0.05)	0.14±0.08 0.14 (0.11)	<0.16±0.39 0.14 (0.11)	<0.16 n.d.	<0.16 n.d.	<0.16±0.98 0.21 (0.27)	<0.16-0.24 0.15 (0.04)
Zn Mtn-Max Avg(SD)	1.8	36.6±123 77.9 (30.4)	24.9±79.6 49.0 (22.7)	24.8±42.4 34.7 (7.69)	37.6±35.5 140 (131)	35.9±13.4 81.8 (34.0)	89.6±27.3 170 (78.0)	42.0±50.1 208 (216)	50.9±89.7 109 (202)	45.1±94.0 58.7 (31.7)	39.0±12.2 80.4 (38.5)	303±82.6 560 (229)	257±119.1 517 (279)	175±57.4 332 (130)
Y Mtn-Max Avg(SD)	0.05	1.47±4.63 2.33 (1.00)	1.84±10.2 4.86 (3.79)	8.26±13.5 10.6 (2.73)	1.41±5.32 3.08 (1.11)	1.64±5.38 2.55 (1.22)	1.87±3.32 2.67 (0.62)	1.85±5.27 3.15 (1.48)	0.46±2.50 0.96 (0.83)	0.97±2.74 1.62 (0.94)	1.60±1.60 1.60 (0.03)	0.19±3.03 1.06 (1.15)	0.30±4.62 1.80 (1.44)	0.55±4.85 2.75 (1.71)
Sc Mtn-Max Avg(SD)	1.1	11.5±48.1 21.8 (11.9)	12.5±54.5 31.3 (19.2)	24.6±36.6 30.0 (5.28)	3.9±20.9 9.86 (5.36)	6.64±26.1 14.9 (5.99)	6.12±23.9 17.0 (8.40)	16.1±22.5 18.7 (2.80)	6.93±11.7 6.55 (3.78)	3.87±17.7 9.08 (6.59)	25.2±28.3 26.7 (2.22)	5.03±11.8 7.75 (2.46)	6.53±18.0 10.6 (3.43)	5.58±16.1 9.21 (3.81)
Ga Mtn-Max Avg(SD)	0.04	3.76±5.35 4.56 (0.53)	4.19±7.57 6.30 (1.46)	8.21±12.2 9.68 (1.77)	2.59±6.20 5.04 (1.53)	2.41±6.79 4.86 (1.47)	10.7±19.3 14.5 (3.73)	21.5±26.1 23.3 (2.50)	1.73±4.52 2.35 (1.57)	1.61±4.25 2.44 (1.49)	2.60±3.20 2.90 (0.43)	29.5±36.6 34.0 (2.96)	20.9±35.9 28.4 (4.76)	14.7±22.2 21.4 (4.22)
Hf Mtn-Max Avg(SD)	0.14	<0.14±0.24 0.16 (0.05)	0.15±1.05 0.47 (0.39)	0.14±1.54 0.83 (0.57)	<0.14±0.66 0.28 (0.18)	<0.14±0.64 0.21 (0.17)	<0.14±0.31 0.18 (0.09)	<0.14±0.23 0.16 (0.06)	0.15 (0.09) 4.93±11.6	0.17 (0.11) 4.24±23.0	0.20 (0.02) 6.7±2.0	0.16 (0.08) 6.7±2.0	0.24 (0.09) 6.7±2.0	0.24 (0.08) 6.7±2.0
Zr Mtn-Max Avg(SD)	6	<6-11.5 6.21 (2.76)	10.3±49.8 27.5 (19.0)	6.19±35.7 19.8 (12.54)	<6-24.5 9.26 (6.60)	<6-18.8 8.44 (5.15)	<6-11.4 7.27 (3.30)	<6-7.35 5.13 (1.48)	6.05 (3.75) 6.05 (3.75)	7.29 (6.48) 7.29 (6.48)	6.30 (1.14) 6.30 (1.14)	6.55 (3.18) 6.55 (3.18)	8.67 (3.81) 8.67 (3.81)	8.11 (2.49) 8.11 (2.49)
Th Mtn-Max Avg(SD)	0.018	0.02±0.08 0.04 (0.01)	0.07±0.58 0.22 (0.23)	0.50±1.54 0.90 (0.48)	0.02±0.23 0.10 (0.07)	0.03±0.35 0.07 (0.10)	<0.018±0.18 0.06 (0.08)	0.03±0.05 0.04 (0.01)	0.02±0.10 0.04 (0.03)	0.08±0.23 0.08 (0.07)	<0.018±0.10 0.10 (0.02)	0.03±0.15 0.07 (0.04)	0.02±0.17 0.08 (0.04)	0.02±0.13 0.05 (0.02)
Pb Mtn-Max Avg(SD)	0.18	0.21±20.9 3.70 (7.05)	0.21±2.45 1.25 (1.06)	0.72±3.82 2.16 (1.47)	0.91±13.9 6.43 (4.80)	0.53±10.4 3.79 (2.99)	0.83±6.75 19.4 (32.1)	1.93±16.5 1.73 (6.39)	0.23±6.02 1.32 (1.64)	0.20±10.7 1.69 (3.03)	0.20±1.60 0.90 (0.99)	0.31±5.20 1.13 (1.79)	0.43±13.2 3.93 (4.33)	0.21±14.8 5.01 (5.42)
Co Mtn-Max Avg(SD)	0.13	53.3±164 90.4 (33.2)	52.7±82.7 67.5 (14.0)	35.1±55.6 46.9 (8.82)	98.9±226 141 (39.2)	82.1±171 131 (33.5)	158±231 186 (34.6)	74.3±248 213 (48.7)	102.9±250 108 (67.4)	90.4±164 112 (58.8)	72.3±102 87.3 (21.2)	182±238 211 (23.6)	151±313 221 (43.3)	113±268 197 (51.1)
Ta Mtn-Max Avg(SD)	0.007	<0.007 0.06 (0.04)	0.01±0.11 0.06 (0.04)	0.01±0.08 0.05 (0.03)	0.01±0.06 0.01 (0.01)	<0.007±0.03 0.01 (0.01)	0.01±0.03 0.01 (0.01)	<0.007 n.d.	<0.007 n.d.	<0.007±0.03 0.01 (0.01)	<0.007 n.d.	<0.007 n.d.	<0.007 n.d.	<0.007 n.d.
Nb Mtn-Max Avg(SD)	0.028	0.10±0.60 0.22 (0.16)	0.18±1.19 0.51 (0.46)	1.05±2.53 1.60 (0.65)	0.05±0.90 0.33 (0.27)	0.08±0.80 0.19 (0.23)	0.11±0.44 0.22 (0.14)	0.20±0.36 0.27 (0.07)	0.13±1.05 0.34 (0.33)	0.07±1.03 0.31 (0.33)	0.20±0.20 0.20 (0.02)	0.31±0.60 0.42 (0.09)	0.25±1.06 0.45 (0.23)	0.20±1.12 0.46 (0.34)
W Mtn-Max Avg(SD)	0.05	<0.05±0.24 0.08 (0.06)	0.06±0.33 0.20 (0.13)	0.16±0.95 0.44 (0.35)	<0.05±0.85 0.21 (0.27)	<0.05±0.38 0.09 (0.11)	<0.05±0.38 0.14 (0.16)	<0.05±0.11 0.06 (0.03)	0.90±1.19 0.25 (0.31)	0.05±0.24 0.08 (0.06)	0.10±0.20 0.10 (0.04)	0.21±1.64 0.72 (0.50)	0.05±4.47 0.71 (1.35)	<0.05±0.72 0.20 (0.21)
U Mtn-Max Avg(SD)	0.011	<0.011±0.07 0.03 (0.01)	0.03±0.20 0.09 (0.07)	0.15±0.41 0.26 (0.11)	<0.011±0.12 0.37±0.66	0.02±0.13 0.04 (0.03)	<0.011±0.06 0.04 (0.02)	0.02±0.03 0.02 (0.01)	0.02±0.09 0.09±0.75	0.02±0.12 0.04 (0.03)	<0.011±0.10 0 (0.02)	0.02±0.09 0.05 (0.02)	0.02±0.14 0.05 (0.02)	0.04±0.10 0.04 (0.03)
Mo Mtn-Max Avg(SD)	0.08	0.47±1.22 0.81 (0.23)	0.52±1.38 0.96 (0.37)	0.85±3.17 1.62 (1.04)	0.03±0.93 1.30 (2.29)	0.34±0.84 0.52 (0.15)	0.40±0.82 0.63 (0.17)	0.49±0.91 0.71 (0.18)	0.09±0.75 0.20 (0.21)	0.10±0.91 0.35 (0.27)	0.10±0.10 0.10 (0.00)	0.41±1.94 0.93 (0.64)	0.46±1.14 0.81 (0.22)	0.61±2.67 1.02 (0.63)
V Mtn-Max Avg(SD)	8	117±184 135 (21.9)	106±225 154 (55.9)	106±204 161 (49.0)	71.3±204 131 (40.8)	83.7±223 146 (47.7)	353±639 459 (136)	451±757 647 (134)	37.4±98.9 34.3 (34.0)	68.4±157 88.2 (51.2)	<8-107 53.3 (75.3)	73.6±108.4 901 (125)	561±105.4 779 (148)	408±75.3 533 (121)
La/Sm Mtn-Max Avg(SD)	N/A	1.26±3.76 2.81 (0.74)	1.89±4.39 3.05 (1.10)	2.59±3.56 3.08 (0.51)	2.49±6.54 3.81 (1.43)	2.30±5.53 2.32 (1.01)	2.20±4.54 3.63 (1.00)	2.46±3.23 2.41 (0.81)	5.43±14.2 4.43 (4.09)	2.75±7.71 3.32 (2.15)	3.30±3.00 3.30 (0.09)	4.87±8.26 4.64 (2.69)	1.55±16.8 5.17 (4.51)	1.40±16.6 4.26 (4.89)
La/Ta Mtn-Max Avg(SD)	N/A	25.8±135 78.4 (33.1)	6.33±100 45.3 (39.3)	37.6±800 270 (338)	35.3±35.4 161 (108)	25.7±43.6 135 (125)	25.0±24.0 128 (93.0)	66.7±148 103 (35.1)	69.3±321 69.3 (74.0)	33.6±24.2 83.9 (70.3)	85.7±93.3 89.5 (5.38)	32.3±11.5 68.8 (32.4)	25.6±135 81.2 (37.5)	16.5±17.4 108 (55.0)
Hf/Ta Mtn-Max Avg(SD)	N/A	5.21±30.3 22.2 (8.57)	1.28±35.6 15.3 (14.4)	5.60±29.8 81.03 (14.4)	11.6±50.0 27.0 (11.65)	8.42±11.6 28.8 (11.6)	10.7±21.3 18.0 (4.89)	20.3±44.0 26.3 (11.8)	16.6 (10.6) 0.27±1.63	21.0 (17.3) 1.60±5.66	22.5±22.9 6.70±7.40	24.2 (8.42) 2.12±51.1	31.2 (10.9) 2.20±22.5	35.8 (18.1) 1.27±7.65
Sr/Y Mtn-Max Avg(SD)	N/A	3.36±24.6 11.9 (8.29)	7.16±31.8 16.1 (10.9)	10.52±47.72 23.69 (16.6)	0.84±7.61 3.23 (2.23)	2.05±4.5 6.37 (4.05)	2.12±2.97 2.60 (0.30)	1.96±6.10 3.40 (1.93)	2.16 (3.86) 1.08±13.7	8.41 (16.2) 1.15±5.65	7.00 (0.41) 2.40±3.40	22.5 (20.5) 2.18±11.1	8.79 (7.44) 1.80±12.9	3.96 (2.00) 1.40±13.2
La/Yb Mtn-Max Avg(SD)	N/A	1.55±3.21 2.19 (0.63)	1.69±3.42 2.78 (0.77)	3.19±5.43 4.16 (0.93)	2.11±6.51 4.06 (1.66)	1.73±4.16 2.93 (0.88)	2.02±5.17 3.27 (1.38)	1.47±2.15 1.85 (0.32)	3.59 (3.49) 2.72 (1.72)	1.15±5.65 2.72 (1.72)	2.40±3.40 2.90 (0.70)	5.72 (3.13) 2.90 (0.70)	3.74 (3.31) 3.19 (3.79)	1.40±13.2 3.19 (3.79)

Table 3 Continued.

Rare Earth Elements (ppm)	LLD	Websterite	Fsp	Gabbro	Harzburgite	OI	Chr	Chr-OI	Dunite	Lherzovite	OI	Massive Chromitite	Matrix Chromitite	Net Txt-Chromitite
La	<i>Min-Max</i> 0.1	0.35-0.72 <i>Avg(SD)</i> 0.57 (0.12)	0.72-3.39 <i>Avg(SD)</i> 1.51 (1.25)	3.14-5.02 <i>Avg(SD)</i> 4.12 (0.76)	0.39-2.01 <i>Avg(SD)</i> 1.34 (0.54)	0.38-2.40 <i>Avg(SD)</i> 0.94 (0.62)	0.72-1.29 <i>Avg(SD)</i> 0.90 (0.27)	0.44-0.77 <i>Avg(SD)</i> 0.61 (0.13)	<0.1-1.83 <i>Avg(SD)</i> 0.59 (0.51)	<0.1-1.21 <i>Avg(SD)</i> 0.66 (0.37)	0.60-0.80 <i>Avg(SD)</i> 0.70 (0.14)	0.17-0.90 <i>Avg(SD)</i> 0.46 (0.25)	0.22-1.00 <i>Avg(SD)</i> 0.58 (0.24)	0.34-1.41 <i>Avg(SD)</i> 0.70 (0.33)
Ce	<i>Min-Max</i> 0.12	0.61-2.08 <i>Avg(SD)</i> 1.28 (0.47)	1.40-7.41 <i>Avg(SD)</i> 3.21 (2.81)	7.68-10.97 <i>Avg(SD)</i> 9.04 (1.39)	0.76-4.30 <i>Avg(SD)</i> 2.81 (1.16)	0.81-4.59 <i>Avg(SD)</i> 1.88 (1.27)	1.43-2.89 <i>Avg(SD)</i> 1.88 (0.68)	0.93-2.19 <i>Avg(SD)</i> 1.45 (0.54)	0.49-4.17 <i>Avg(SD)</i> 1.18 (1.17)	1.09-2.71 <i>Avg(SD)</i> 1.43 (0.84)	1.30-1.70 <i>Avg(SD)</i> 1.50 (0.25)	0.26-2.17 <i>Avg(SD)</i> 0.93 (0.66)	0.40-2.15 <i>Avg(SD)</i> 1.19 (0.55)	0.64-3.36 <i>Avg(SD)</i> 1.60 (0.81)
Pr	<i>Min-Max</i> 0.014	0.08-0.31 <i>Avg(SD)</i> 0.18 (0.08)	0.16-1.06 <i>Avg(SD)</i> 0.45 (0.41)	1.11-1.36 <i>Avg(SD)</i> 1.2 (0.11)	0.09-0.56 <i>Avg(SD)</i> 0.34 (0.14)	0.09-0.58 <i>Avg(SD)</i> 0.23 (0.16)	0.17-0.30 <i>Avg(SD)</i> 0.22 (0.06)	0.10-0.35 <i>Avg(SD)</i> 0.20 (0.11)	0.05-0.46 <i>Avg(SD)</i> 0.13 (0.12)	0.12-0.28 <i>Avg(SD)</i> 0.17 (0.09)	0.20-0.20 <i>Avg(SD)</i> 0.20 (0.02)	0.03-0.30 <i>Avg(SD)</i> 0.12 (0.09)	0.04-0.32 <i>Avg(SD)</i> 0.16 (0.08)	0.07-0.42 <i>Avg(SD)</i> 0.22 (0.12)
Nd	<i>Min-Max</i> 0.06	0.32-1.42 <i>Avg(SD)</i> 0.78 (0.36)	0.66-4.68 <i>Avg(SD)</i> 1.98 (1.83)	4.76-5.7 <i>Avg(SD)</i> 5.08 (0.44)	0.32-2.43 <i>Avg(SD)</i> 1.43 (0.62)	0.40-2.52 <i>Avg(SD)</i> 1.00 (0.72)	0.71-1.13 <i>Avg(SD)</i> 0.91 (0.21)	0.89 (0.55) <i>Avg(SD)</i> 0.89 (0.55)	0.15-1.64 <i>Avg(SD)</i> 0.48 (0.45)	0.40-1.27 <i>Avg(SD)</i> 0.72 (0.44)	0.70-0.90 <i>Avg(SD)</i> 0.80 (0.15)	0.08-1.36 <i>Avg(SD)</i> 0.50 (0.45)	0.15-1.62 <i>Avg(SD)</i> 0.69 (0.45)	1.03 (0.60) <i>Avg(SD)</i> 1.03 (0.60)
Sm	<i>Min-Max</i> 0.026	0.11-0.45 <i>Avg(SD)</i> 0.22 (0.10)	0.16-1.38 <i>Avg(SD)</i> 0.58 (0.54)	1.21-1.53 <i>Avg(SD)</i> 1.34 (0.15)	0.11-0.67 <i>Avg(SD)</i> 0.37 (0.16)	0.11-0.63 <i>Avg(SD)</i> 0.26 (0.17)	0.19-0.33 <i>Avg(SD)</i> 0.25 (0.06)	0.14-0.55 <i>Avg(SD)</i> 0.29 (0.18)	0.03-0.36 <i>Avg(SD)</i> 0.13 (0.09)	0.08-0.31 <i>Avg(SD)</i> 0.18 (0.11)	<0.026-0.20 <i>Avg(SD)</i> 0.20 (0.03)	0.03-0.36 <i>Avg(SD)</i> 0.15 (0.11)	0.03-0.51 <i>Avg(SD)</i> 0.19 (0.16)	0.05-0.55 <i>Avg(SD)</i> 0.30 (0.21)
Eu	<i>Min-Max</i> 0.0031	0.05-0.16 <i>Avg(SD)</i> 0.09 (0.03)	0.10-0.44 <i>Avg(SD)</i> 0.22 (0.15)	0.41-0.54 <i>Avg(SD)</i> 0.48 (0.06)	0.04-0.24 <i>Avg(SD)</i> 0.13 (0.05)	0.05-0.24 <i>Avg(SD)</i> 0.11 (0.06)	0.07-0.09 <i>Avg(SD)</i> 0.08 (0.01)	0.05-0.25 <i>Avg(SD)</i> 0.11 (0.09)	0.01-0.09 <i>Avg(SD)</i> 0.03 (0.02)	0.05-0.12 <i>Avg(SD)</i> 0.06 (0.03)	0.05-0.06 <i>Avg(SD)</i> 0.05 (0.01)	0.01-0.12 <i>Avg(SD)</i> 0.04 (0.05)	0.06 (0.05) <i>Avg(SD)</i> 0.06 (0.05)	0.11 (0.08) <i>Avg(SD)</i> 0.11 (0.08)
Gd	<i>Min-Max</i> 0.009	0.16-0.61 <i>Avg(SD)</i> 0.30 (0.14)	0.25-1.72 <i>Avg(SD)</i> 0.77 (0.66)	1.38-1.91 <i>Avg(SD)</i> 1.59 (0.24)	0.16-0.90 <i>Avg(SD)</i> 0.46 (0.21)	0.18-0.81 <i>Avg(SD)</i> 0.35 (0.21)	0.27-0.40 <i>Avg(SD)</i> 0.33 (0.05)	0.19-0.74 <i>Avg(SD)</i> 0.40 (0.24)	0.04-0.41 <i>Avg(SD)</i> 0.11 (0.11)	0.10-0.37 <i>Avg(SD)</i> 0.22 (0.13)	0.20-0.30 <i>Avg(SD)</i> 0.20 (0.04)	0.01-0.42 <i>Avg(SD)</i> 0.14 (0.15)	0.03-0.69 <i>Avg(SD)</i> 0.24 (0.21)	0.06-0.74 <i>Avg(SD)</i> 0.40 (0.29)
Tb	<i>Min-Max</i> 0.0023	0.03-0.11 <i>Avg(SD)</i> 0.05 (0.02)	0.05-0.30 <i>Avg(SD)</i> 0.14 (0.11)	0.23-0.33 <i>Avg(SD)</i> 0.27 (0.04)	0.03-0.15 <i>Avg(SD)</i> 0.08 (0.03)	0.03-0.14 <i>Avg(SD)</i> 0.06 (0.03)	0.05-0.07 <i>Avg(SD)</i> 0.06 (0.01)	0.04-0.13 <i>Avg(SD)</i> 0.07 (0.04)	0.01-0.05 <i>Avg(SD)</i> 0.02 (0.01)	0.02-0.06 <i>Avg(SD)</i> 0.04 (0.02)	0.04-0.05 <i>Avg(SD)</i> 0.04 (0.01)	0.01-0.08 <i>Avg(SD)</i> 0.03 (0.03)	0.01-0.12 <i>Avg(SD)</i> 0.04 (0.03)	0.01-0.13 <i>Avg(SD)</i> 0.07 (0.04)
Dy	<i>Min-Max</i> 0.009	0.26-0.77 <i>Avg(SD)</i> 0.40 (0.16)	0.35-1.95 <i>Avg(SD)</i> 0.92 (0.73)	1.50-2.25 <i>Avg(SD)</i> 1.81 (0.36)	0.20-1.01 <i>Avg(SD)</i> 0.52 (0.23)	0.25-0.93 <i>Avg(SD)</i> 0.42 (0.22)	0.33-0.54 <i>Avg(SD)</i> 0.42 (0.09)	0.29-0.90 <i>Avg(SD)</i> 0.51 (0.26)	0.06-0.35 <i>Avg(SD)</i> 0.13 (0.11)	0.13-0.44 <i>Avg(SD)</i> 0.26 (0.15)	0.31-0.36 <i>Avg(SD)</i> 0.34 (0.01)	0.03-0.52 <i>Avg(SD)</i> 0.18 (0.19)	0.05-0.79 <i>Avg(SD)</i> 0.31 (0.25)	0.07-0.87 <i>Avg(SD)</i> 0.49 (0.32)
Ho	<i>Min-Max</i> 0.0025	0.06-0.17 <i>Avg(SD)</i> 0.09 (0.03)	0.07-0.40 <i>Avg(SD)</i> 0.19 (0.14)	0.31-0.47 <i>Avg(SD)</i> 0.38 (0.07)	0.05-0.22 <i>Avg(SD)</i> 0.11 (0.04)	0.06-0.20 <i>Avg(SD)</i> 0.19-0.60	0.07-0.11 <i>Avg(SD)</i> 0.09 (0.01)	0.07-0.19 <i>Avg(SD)</i> 0.11 (0.05)	0.02-0.09 <i>Avg(SD)</i> 0.03 (0.01)	0.03-0.10 <i>Avg(SD)</i> 0.12-0.42	0.06-0.08 <i>Avg(SD)</i> 0.22-0.29	0.01-0.11 <i>Avg(SD)</i> 0.03-0.32	0.01-0.17 <i>Avg(SD)</i> 0.02 (0.01)	0.02-0.18 <i>Avg(SD)</i> 0.05-0.55
Er	<i>Min-Max</i> 0.007	0.14-0.32 <i>Avg(SD)</i> 0.25 (0.06)	0.24-1.15 <i>Avg(SD)</i> 0.57 (0.41)	0.88-1.38 <i>Avg(SD)</i> 1.11 (0.25)	0.16-0.63 <i>Avg(SD)</i> 0.34 (0.14)	0.19-0.60 <i>Avg(SD)</i> 0.29 (0.13)	0.21-0.36 <i>Avg(SD)</i> 0.28 (0.06)	0.22-0.56 <i>Avg(SD)</i> 0.34 (0.15)	0.11 (0.09) <i>Avg(SD)</i> 0.11 (0.09)	0.12-0.42 <i>Avg(SD)</i> 0.19 (0.12)	0.20 (0.02) <i>Avg(SD)</i> 0.20 (0.02)	0.12 (0.12) <i>Avg(SD)</i> 0.12 (0.12)	0.21 (0.15) <i>Avg(SD)</i> 0.21 (0.15)	0.32 (0.19) <i>Avg(SD)</i> 0.32 (0.19)
Tm	<i>Min-Max</i> 0.0019	0.02-0.05 <i>Avg(SD)</i> 0.04 (0.01)	0.04-0.16 <i>Avg(SD)</i> 0.08 (0.05)	0.13-0.20 <i>Avg(SD)</i> 0.16 (0.03)	0.02-0.09 <i>Avg(SD)</i> 0.05 (0.02)	0.03-0.09 <i>Avg(SD)</i> 0.04 (0.01)	0.03-0.06 <i>Avg(SD)</i> 0.04 (0.01)	0.04-0.08 <i>Avg(SD)</i> 0.05 (0.02)	0.01-0.05 <i>Avg(SD)</i> 0.02 (0.01)	0.02-0.09 <i>Avg(SD)</i> 0.03 (0.02)	0.04-0.04 <i>Avg(SD)</i> 0.04 (0.01)	0.01-0.05 <i>Avg(SD)</i> 0.02 (0.01)	0.01-0.07 <i>Avg(SD)</i> 0.03 (0.02)	0.01-0.08 <i>Avg(SD)</i> 0.05 (0.02)
Yb	<i>Min-Max</i> 0.009	0.19-0.35 <i>Avg(SD)</i> 0.27 (0.05)	0.25-0.99 <i>Avg(SD)</i> 0.53 (0.33)	0.77-1.29 <i>Avg(SD)</i> 1.02 (0.28)	0.18-0.62 <i>Avg(SD)</i> 0.34 (0.12)	0.21-0.58 <i>Avg(SD)</i> 0.30 (0.11)	0.21-0.36 <i>Avg(SD)</i> 0.29 (0.06)	0.26-0.52 <i>Avg(SD)</i> 0.34 (0.12)	0.12-0.39 <i>Avg(SD)</i> 0.15 (0.11)	0.16-0.73 <i>Avg(SD)</i> 0.23 (0.19)	0.26-0.27 <i>Avg(SD)</i> 0.26 (0.01)	0.03-0.33 <i>Avg(SD)</i> 0.13 (0.12)	0.05-0.46 <i>Avg(SD)</i> 0.22 (0.13)	0.07-0.54 <i>Avg(SD)</i> 0.32 (0.16)
Lu	<i>Min-Max</i> 0.002	0.03-0.06 <i>Avg(SD)</i> 0.04 (0.01)	0.04-0.14 <i>Avg(SD)</i> 0.08 (0.04)	0.11-0.19 <i>Avg(SD)</i> 0.15 (0.04)	0.03-0.09 <i>Avg(SD)</i> 0.05 (0.01)	0.03-0.09 <i>Avg(SD)</i> 0.05 (0.01)	0.03-0.06 <i>Avg(SD)</i> 0.05 (0.01)	0.04-0.08 <i>Avg(SD)</i> 0.05 (0.01)	0.02-0.06 <i>Avg(SD)</i> 0.03 (0.01)	0.02-0.14 <i>Avg(SD)</i> 0.04 (0.03)	0.04-0.04 <i>Avg(SD)</i> 0.04 (0.01)	0.01-0.05 <i>Avg(SD)</i> 0.02 (0.02)	0.01-0.07 <i>Avg(SD)</i> 0.03 (0.01)	0.01-0.08 <i>Avg(SD)</i> 0.05 (0.02)
Noble Metals (ppb)														
Ir	<i>Min-Max</i> 0.01	5.13-10.2 <i>Avg(SD)</i> 7.31 (2.12)	1.30-2.78 <i>Avg(SD)</i> 2.04 (1.04)	1.30-3.83 <i>Avg(SD)</i> 2.64 (1.69)	3.31-13.5 <i>Avg(SD)</i> 7.51 (4.30)	8.10-21.7 <i>Avg(SD)</i> 12.8 (7.66)	12.9-24.6 <i>Avg(SD)</i> 18.8 (8.27)	12.0-29.2 <i>Avg(SD)</i> 20.6 (12.2)	0.31-8.42 <i>Avg(SD)</i> 4.24 (4.06)	3.30-23.7 <i>Avg(SD)</i> 9.56 (7.50)	N/A	56.9-273 <i>Avg(SD)</i> 117 (74.6)	30.6-90.7 <i>Avg(SD)</i> 55.8 (17.9)	32.3-92.8 <i>Avg(SD)</i> 47.9 (19.6)
Ru	<i>Min-Max</i> 0.08	5.20-18.4 <i>Avg(SD)</i> 10.5 (5.87)	3.04-7.04 <i>Avg(SD)</i> 5.04 (2.83)	2.32-5.44 <i>Avg(SD)</i> 3.88 (2.20)	7.70-34.7 <i>Avg(SD)</i> 19.7 (11.2)	16.0-48.2 <i>Avg(SD)</i> 27.0 (18.3)	38.2-68.9 <i>Avg(SD)</i> 53.6 (21.8)	42.9-122 <i>Avg(SD)</i> 82.4 (55.7)	4.13-25.7 <i>Avg(SD)</i> 15.3 (9.88)	2.86-37.2 <i>Avg(SD)</i> 18.9 (13.3)	N/A	155-755 <i>Avg(SD)</i> 367 (196)	126-299 <i>Avg(SD)</i> 208 (55.5)	97.1-284 <i>Avg(SD)</i> 178 (65.9)
Rh	<i>Min-Max</i> 0.04	6.38-17.8 <i>Avg(SD)</i> 11.4 (4.71)	2.34-8.39 <i>Avg(SD)</i> 5.36 (4.27)	3.45-6.58 <i>Avg(SD)</i> 5.01 (2.21)	2.98-27.6 <i>Avg(SD)</i> 13.9 (10.3)	14.8-38.0 <i>Avg(SD)</i> 23.6 (12.5)	22.1-39.9 <i>Avg(SD)</i> 31.0 (12.6)	12.8-33.2 <i>Avg(SD)</i> 23.0 (14.4)	0.26-17.0 <i>Avg(SD)</i> 5.80 (7.60)	6.50-44.9 <i>Avg(SD)</i> 20.9 (15.6)	N/A	74.6 (21.4) <i>Avg(SD)</i> 149-1356	24.5-70.1 <i>Avg(SD)</i> 215-604	32.7-154 <i>Avg(SD)</i> 56.1 (37.5)
Pt	<i>Min-Max</i> 0.17	31.5-312 <i>Avg(SD)</i> 104 (83.9)	14.2-46.5 <i>Avg(SD)</i> 30.4 (22.8)	3.20-74.0 <i>Avg(SD)</i> 26.0 (33.3)	1.72-353 <i>Avg(SD)</i> 52.0 (41.4)	34.7-544 <i>Avg(SD)</i> 167 (156)	66.4-464 <i>Avg(SD)</i> 276 (228)	66.4-746 <i>Avg(SD)</i> 171 (284)	0.58-113 <i>Avg(SD)</i> 18.2 (26.9)	1.04-396 <i>Avg(SD)</i> 64.7 (48.9)	76.6-193 <i>Avg(SD)</i> 135 (82.3)	149-1356 <i>Avg(SD)</i> 440 (426)	215-604 <i>Avg(SD)</i> 39.9 (134)	4.57-2658 <i>Avg(SD)</i> 660 (779)
Pd	<i>Min-Max</i> 0.12	30.9-254 <i>Avg(SD)</i> 112 (105)	18.6-223 <i>Avg(SD)</i> 121 (144)	3.11-64.2 <i>Avg(SD)</i> 29.7 (38.6)	1.51-110 <i>Avg(SD)</i> 159 (134)	98.8-491 <i>Avg(SD)</i> 297 (164)	176-266 <i>Avg(SD)</i> 368 (166)	159-284 <i>Avg(SD)</i> 438 (294)	0.58-76.2 <i>Avg(SD)</i> 13.7 (8.2)	0.58-134 <i>Avg(SD)</i> 120 (131)	35.7-60.3 <i>Avg(SD)</i> 48.0 (17.3)	131-458 <i>Avg(SD)</i> 306 (97.3)	97.9-312 <i>Avg(SD)</i> 194 (74.0)	44.8-758 <i>Avg(SD)</i> 232 (204)
Au	<i>Min-Max</i> 0.4	3.49-11.6 <i>Avg(SD)</i> 7.13 (2.88)	20.6-77.3 <i>Avg(SD)</i> 48.9 (40.0)	1.23-9.97 <i>Avg(SD)</i> 5.08 (4.46)	2.00-26.6 <i>Avg(SD)</i> 6.90 (9.70)	3.08-35.7 <i>Avg(SD)</i> 16.5 (12.6)	7.92-65.4 <i>Avg(SD)</i> 32.9 (29.4)	3.72-46.5 <i>Avg(SD)</i> 18.4 (24.3)	1.14-10.3 <i>Avg(SD)</i> 3.11 (2.62)	1.14-13.4 <i>Avg(SD)</i> 4.46 (4.37)	5.40-6.70 <i>Avg(SD)</i> 6.10 (0.91)	1.73-13.3 <i>Avg(SD)</i> 6.81 (4.42)	1.91-57.5 <i>Avg(SD)</i> 16.8 (17.1)	1.78-32.1 <i>Avg(SD)</i> 15.3 (11.0)

Table 3 Continued.

2.14 Figure Captions

Fig. 1. Geological map of the McFaulds Lake greenstone belt showing felsic to ultramafic intrusive suites, supracrustal rocks, and mineralization showings (after Metsaranta et al., 2015).

Fig. 2. Simplified geological map of the southern Ring of Fire Intrusive Suite showing felsic to ultramafic intrusive and supracrustal rocks, including the Black Thor Intrusive Complex (BTIC), Double Eagle Intrusive Complex (DEIC), and significant chromite, sulfide and vanadium showings. Lithologies and abbreviations not seen correspond to Figure 1 legend (after Metsaranta and Houlé, 2017).

Fig. 3. Detailed geological map of the BTIC and surrounding footwall, hanging wall, and felsic to mafic intrusive rocks. Labeled are 39 logged and/or sampled diamond drill holes, and mineralization, including the Black Thor Chromite Zone (BTCZ), Black Label Chromite Zone (BLCZ), Contact Zone (CONT), Blue Jay Extension (BJ EXT), Blue Jay (BJ), NEBZ (Northeast Brecciated Zone), CBZ (Central Brecciated Zone), and SWBZ (Southwest Brecciated Zone). Modified after Carson et al. (2015) and Spath et al. (2015).

Fig. 4. Schematic stratigraphic section through the BTIC, and adjacent hanging and footwall rocks. Displayed are transgressive bodies (biotite gabbro, ferrogabbro and LWI), and zones of sulfide (red) and chromite mineralization (black). Modified after Carson et al. (*in prep*) and Weston and Shinkle (2013). References for the geochronology: ¹ Mungall et al., 2010 and ² Rayner and Stott, 2005.

Fig. 5. Slab scans of NQ (47.6 mm diameter) drill core displaying lithologies of the Lower and Middle Ultramafic Series, and BLCZ: A) Medium-grained, serpentinized dunite (Dun; black variety) cross-cut by small (<2 cm) websterite diklets (Web) with talc-magnesite (Tlc-Mgs) veinlets (<2mm) and hybrid olivine websterite (H-Ol web) present at margin (BT-09-98/190). B) Serpentinized black dunite interlayered with grey lherzolite (Lherz; BT-11-191/75). C) Medium to coarse-grained poikilitic basal lherzolite with chalcopyrite veinlet (Cpy; BT-09-98/113). D) Typical medium-grained olivine pyroxenite (BT-12-210/24). E) Medium-grained pyroxenite with clinopyroxene oikocrysts (Cpx oiko) and talc-magnesite veinlets (BT-09-29/183). F) Semi-massive chromitite with clinopyroxene oikocrysts (BT-11-177/146). G) Layered chromitite composed of intercalation of cm-scale massive chromitite (Mass chrmt), and mm- to cm-scale chromite-bearing talc-altered dunite with serpentinite (Srp) veinlets throughout (BT-12-206/143). H) Normal grading of massive chromitite to semi-massive (Semi chrmt) to matrix (Mat chrmt) to net-textured chromitite (Net chrmt; BT-09-104/239). Pyroxene is typically altered to a beige color, whereas olivine is altered to dull black. All drill core are younging to the right.

Fig. 6. Slab scans of NQ and HQ (E-G, 63.5 mm diameter) drill core showing clast-free and -bearing UWZ lithologies. A) Accumulate, medium-grained, homogeneous ('typical') websterite (BT-09-25/435). B) Coarse-grained feldspathic websterite (Fsp web) in gradational contact with medium-grained gabbro (Gabbro; BT-09-98/211). C) Pegmatitic gabbro with sulfide blebs (Sul; BT-09-98/243). D) Sulfide-bearing pegmatitic, gabbroic dikelet cross-cutting BTIC lherzolite (BT-09-100/67). E) 'Typical' websterite containing a dunite clast; note serpentine veinlets originating from dunite clast (BT-11-199A/34). F) Websterite dike containing small chromitite and dunite clasts injected at the contact between layers of dunite and massive chromitite; note sharp contact with chromitite and diffuse contact with dunite (GT-13-13/212). G) Coarse-grained, clast-free websterite injected at the contact between layers of dunite

and massive chromitite (GT-13-13/251). Serpentinite veinlets are present in almost all olivine-bearing samples. Clasts outlined in dashed lines. All drill core is younging to the right.

Fig. 7. Slab scans of NQ and HQ (G) drill core showing BLHZ lithologies A) Sulfide-bearing, hybrid olivine websterite containing several rounded, serpentinized dunite and lherzolite clasts (BT-08-06/293). B) Sulfide-bearing hybrid olivine websterite with wispy/amoeboidal dunite clasts showing preferred direction; note sulfide is localized at the margins of dunite clasts (BT-09-29/314). C) Hybrid harzburgite (H-harz) containing one large subrounded dunite clast showing entrainment of olivine (Ol) xenocrysts into the hybrid matrix at margin (BT-09-46/212). D) Sulfide-bearing hybrid harzburgite containing subangular dunite and lherzolite clasts and olivine xenocrysts (BT-09-95/329). E) Margin of semi-massive chromitite showing the injection of sulfide-bearing hybrid chromite olivine websterite (H-Chr Ol web); note the olivine and chromite chadacrysts enclosed in pyroxene oikocrysts (BT-11-182/276). F) Sulfide-bearing (~5%), coarse-grained websterite with wispy clasts (relict beds) of dunite and semi-massive chromitite (BT-11-177/107). G) Hybrid chromite harzburgite (H-Chr harz) containing a subangular clast of massive chromitite with sharp contacts and layering (pseudomorphed black olivine) parallel to core axis (GT-13-13/217). H) Diffuse margin of a rounded, semi-massive chromitite showing the injection of hybrid chromite harzburgite at bottom (BT-11-179/307). Serpentinite veinlets are present in almost all olivine-bearing samples. Clasts outlined in dashed lines. All drill core is younging to the right.

Fig. 8. Typical intervals (HQ core size) showing the macroscale textural variations within the BLHZ. A) Dominantly hybrid olivine websterite containing abundant rounded dunite-lherzolite clasts with websterite dikes between interbedded massive chromitite clasts (GT-13-13/229-234). B) Dominantly hybrid chromite harzburgite containing subrounded massive to matrix-textured chromitite, minor rounded dunite clasts and local intervals of other hybrid lithologies (GT-13-13/220-226). Outlines of lherzolite (purple), dunite (green), and chromitite (black) clasts are shown as dashed lines with white dashed lines showing orientation of layering *within* clasts; pink solid lines show intrusion of unhybridized websterite dikes. Larger clasts and appropriate hybrid matrix lithologies are labeled. See Figures 5 and 6 for abbreviations.

Fig. 9. Schematic geological map of the BTIC showing UWZ, BLHZ, and mineralization (Modified after Carson et al., 2015 and Spath et al., 2015). Chromite mineralization: BLCZ (Black Label Chromite Zone) and BTCZ (Black Thor Chromite Zone). Sulfide mineralization: NEBZ (Northeast Brecciated Zone), CBZ (Central Brecciated Zone), SWBZ (Southwest Brecciated Zone), BJ (Blue Jay Zone), and BJ EXT (Blue Jay Extension). Geology projected from logged diamond drill core; drill hole traces correspond to stratigraphic columns in Figures 10 and 11.

Fig. 10. Lithostratigraphy across the BTIC showing major lithologies and main characteristics of clasts (lithology, size, shape) at A) the west margin of the LWI (BT-09-26) and B) within the core of the LWI (GT-13-13). All drill holes young toward top of page and are shown in true-thickness. Possible clasts >1m are displayed as BTIC lithologies, whereas smaller are displayed as clasts (see legend). Descriptions in bold refer to slab scans displayed in Figure 5 and 6. Refer to Figure 8 for drill core intervals (GT-13-13/220-226 and 229-234).

Fig. 11. Lithostratigraphy across the BTIC showing major lithologies and main characteristics of clasts (lithology, size, shape) within A) the feeder zone of the BTIC (BT-09-98) and B) a marginal dike of the LWI (BT-09-95). All drill holes young toward top of page and are

shown in true-thickness. Possible clasts >1m are displayed as BTIC lithologies, whereas smaller are displayed as clasts (see legend). Descriptions in red refer to sulfide mineralization, whereas in bold refer to slab scans displayed in Figure 5 and 6. See Figure 10 for abbreviations.

Fig. 12. Quadrilateral plot of plagioclase (Pl) – orthopyroxene (Opx) – clinopyroxene (Cpx) – olivine (Ol) showing the UWZ, hybrid rocks, and silicate-chromitite clast mineralogy. All calculated chromite-free to represent only the silicate component(s). Circled numbers correspond to classification scheme after Le Maitre et al. (1989): (1) Anorthosite, (2) gabbro, (3) gabbronorite, (4) norite, (5) feldspathic websterite, (6) clinopyroxenite, (7) websterite, (8) orthopyroxenite, (9) olivine clinopyroxenite, (10) olivine websterite, (11) olivine orthopyroxenite, (12) wehrlite, (13) lherzolite, (14) harzburgite, and (15) dunite. Normative calculations of whole rock geochemistry from this study (symbols), Carson et al., *in prep* (silicate clast field) and Mehermenesh et al., *in prep* (chromitite clast field).

Fig. 13. Least-altered examples of the UWZ and the BLHZ in thin section, A) websterite exhibiting adcumulate texture with Opx euhedral and Cpx interstitial in cross-polarized light (BT-09-25/435). B) Hybrid Ol websterite showing the removal and impingement of Ol xenocrysts from a dunite clast in plane polarized (BT-11-179/87). C) Hybrid harzburgite with serpentinized dunite clasts enclosed by poikilitic Opx in cross-polarized light; note sulfide mineralization (Po) adjacent to dunite clasts (BT-11-179/128). D) Hybrid chromite (Chr) Ol websterite with abundant chromitite clasts and Chr xenocrysts in plane polarized (GT-13-13/212). See Figures 5 and 6 for clast abbreviations, and Figure 12 for mineral abbreviations.

Fig. 14. Photomicrographs of the UWZ (A-D) and BTIC (E-H) in cross-polarized light (XPL). A) Typical hypidiomorphic websterite with sub-euhedral orthopyroxene and oikocrystic clinopyroxene (BT-09-34/69). B) UWZ websterite depicting textural relationships between cumulus Opx, and intercumulus Cpx and plagioclase (BT-11-177/107). C) Orthocumulate feldspathic websterite shows an increase in Pl and Cpx compared to A (BT-09-34/121). D) Pegmatitic gabbronoritic dike (Gabbro dike) intruding BTIC lherzolite (BT-11-177/97). E) Typical BTIC lherzolite showing pervasive serpentinization producing secondary magnetite (Mgt) (BT-12-210/50). F) Net-textured chromitite with oikocrystic Cpx enveloping fine-grained Chr that is locally more abundant between Cpx oikocrysts giving a patchy texture (BT-08-08/217). G) Adcumulate dunite clast with an inequigranular and panidiomorphic texture (BT-09-32/129). H) Sharp contact between chromitite and dunite beds within the BLCZ showing both monomineralic (adcumulate; Ol *or* Chr) and polymineralic (heteroadcumulate; Ol *and* Chr) layering (GT-13-13/212). See previous figures for abbreviations.

Fig. 15. Photomicrographs of Chr-free hybrid lithologies and associated dunite-lherzolite clasts: A) Diffuse dunite clast margin with interfingering poikilitic Opx enveloping detached Ol; note gradational increase in Ol toward clast (XPL) (BT-09-101/407). B) Margin of dunite clast showing blebby, corroded Ol chadacrysts showing with various levels of digestion (XPL) (BT-11-179/128). C) Dunite clast margin showing euhedral UWZ Opx embaying contact and ‘plucking’ Ol (PPL) (BT-11-179/87). D) Poly-grain Ol aggregate from a dunite clast showing corrosion by UWZ Opx, note ‘pinching’ in Ol at left (XPL) (same location as C). E) Sharp dunite clast showing little Ol removed (XPL at 1X; BT-11-199A/34). F) Dunite clast showing Ol removal and entrainment with sharp contact (PPL) (BT-09-34/120.5). See previous figures for abbreviations.

Fig. 16. Photomicrographs of Chr-rich hybrid lithologies and associated chromitite-dunite-lherzolite clasts. A) Heavily disseminated chromitite clast with diffuse margin exhibiting a gradation from hybrid Chr harzburgite to websterite (XPL) (BT-11-177/108). B) Net-textured chromitite clast showing characteristic Chr-free halo of oikocrystic Opx surrounding consumed Ol (XPL) (BT-09-34/60.7). C) Semi-massive chromitite clast in diffuse contact with BLHZ Chr harzburgite (PPL; GT-13-13/224). D) Massive chromitite clast with sharp, embayed margin showing removal and replacement of Ol by UWZ Opx; note interstitial Chr being incorporated into the websterite matrix (PPL) (BT-09-32/122). E) Massive chromitite clast in sharp contact with coarse-grained websterite in PPL; white box denotes inset view that depicts a coarse-grained chromitite clast that has fractured along margin to form very fine-grained Chr (XPL) (BT-11-184/170). F) Margin of dunite clast showing patchy pyrrhotite (Po)-pentlandite (Pn)-chalcopyrite (Ccp) mineralization with preferential adhesion to Ol (now Srp) (BT-09-29/314). Dashed lines indicate clast boundaries. See previous figures for abbreviations.

Fig. 17. Bivariate plots of Ni versus Forsterite content of olivine (A) and Cr_2O_3 versus MgO of chromite (B) from the UWZ, BLHZ, and BTIC clast lithologies. For the same sample the plots show clast grains as closed and matrix (xenocrystic) grains as open; same colors indicate analyses were taken from the equivalent samples. Fractional crystallization (FC) and sulfide accumulation trends displayed as gray arrows.

Fig. 18. Wollastonite (Wo) – enstatite (En) – ferrosilite (Fs) ternary plots showing A) BTIC, B) BLHZ, and C) UWZ pyroxene; inset D (red outline) displays all rock types for comparison. Clinopyroxene (Cpx) is shown as upward triangles and orthopyroxene (Opx) as downward with color denoting lithology. Samples from this study: BT-09-34/121, BT-11-199A/46, BT-09-32/119, BT-09-32/129, BT-11-180/171, BT-11-177/97, BT-11-177/108, and BT-11-179/87. Pyroxene abbreviations: ferrosilite (Fs), hypersthene (Hyp), augite (Aug), diopside (Di), pigeonite (Pgt), and hedenbergite (Hd).

Fig. 19. V_2O_3 – ZnO – TiO_2 ternary plots displaying EPMA analyses of chromites from BLHZ (A), BLCZ (B), and BTCZ (C). Inset D (red outline) shows fields and averages corresponding to the lithologies of A-C. Samples from this study: BT-11-180/171, BT-11-177/108, BT-11-179/87, BT-11-182/276, and BT-11-179/176. Data are from this study (BLHZ chromite), Carson et al., *in prep*, (BTCZ chromite) and Mehermenesh et al. *in prep* (BLCZ chromite)

Fig. 20. MgO variation diagrams showing whole rock geochemistry from UWZ, BTIC, BLHZ and analyzed minerals: (A) SiO_2 versus MgO, (B) TiO_2 versus MgO, (C) Al_2O_3 versus MgO, (D) Cr_2O_3 versus MgO, (E) FeO_t versus MgO, (F) CaO versus MgO, (G) NiO versus MgO, and (H) CoO versus MgO. UWZ and BLHZ samples are displayed as larger triangles, BTIC samples as small circles, and mineral nodes as open diamonds; Ol fractionation line is shown for reference (A, F). Pl not analyzed for NiO, Cr_2O_3 , CoO, and FeO_t; Chr for SiO_2 ; and Ol and Px for Cr_2O_3 . Abbreviations: Mass=massive, Mx=matrix-textured, and Net=net-textured. Data plotted is from this study, Cliffs Natural Resources Inc. database (grey crosses), Carson et al., *in prep* (dunite/lherzolite/olivine websterite, n=17) and Mehermenesh et al., *in prep* (chromitites, n=21).

Fig. 21. Sulfur versus Au (A), Pd (B), Pt (C), Rh (D), Ru (E), and Ir (F) of UWZ, BTIC, and BLHZ (large triangles) lithologies. Plots exclude outliers. Data plotted is from this study,

Cliffs Natural Resources Inc. database (grey crosses), Carson et al., *in prep* (dunite/lherzolite/olivine websterite, n=12) and Mehermenesh et al., *in prep* (chromitites, n=18).

Fig. 22. Extended trace and rare earth element diagrams of A) UWZ, B) BTIC Chr-poor clast, C) BTIC Chr-rich clast, D) BLHZ harzburgite, and E) BLHZ Chr harzburgite lithologies. Averages of major lithologies are shown (F); symbols, color and totals used to calculate mean are displayed in plot legends. Shaded regions in E-D show fields of precursor clasts (dunite, lherzolite and chromitite) and UWZ websterite; hatched regions show overlapping fields; yellow regions show lower limit of detection. Data calculated volatile-free and normalized to primitive mantle (McDonough and Sun, 1995). Data plotted is from this study, Carson et al., *in prep* (dunite/lherzolite/olivine websterite, n=12), Mehermenesh et al., *in prep* (chromitites, n=18) and Goa (2003).

Fig. 23. Schematic cross-section (A) through the central part of the BTIC showing macroscale intrusion. B) Slab showing the formation of chromitite clasts through brecciation of a single bed; note location of red inset corresponding to C (GT-13-13/248). C) Scanned thin section (PL) showing a websterite dike (altered) intruding a bedding plane between a chromitiferous dunite bed and massive chromitite clast; note the sharp, embayed contact of the chromitite clast and the diffuse, irregular contact with the overlying dunite bed (BT-11-182/158m). D) Slab scan showing an interbedded chromitite clast created through the removal of an adjacent composite bed (GT-13-13/211). Lithology colors in A correspond to Figure 4; scan abbreviations in B-D correspond to Figures 15 and 16.

Fig. 24. Progressive physical and chemical assimilation of clast resulting in complete hybridization. A T1) Initial entrainment of clast from wall rocks results in thermal anisotropies and mechanical disaggregation into continent xenocrysts. A1) Shows a dunite clast mechanically disaggregating into Ol xenocrysts and clots to hybridize the originally websteritic matrix. B T2) Clast undergoes partial melting resulting in mixing with websterite melt to crystallize discrete hybrid crystals. B1) Shows the mixing of nascent clast partial melt with LWI melt at clast/melt interface. C T3) Further disintegration of clasts progresses to point where it is only vaguely recognizable. C1) Chromitite clast-margin Ol reacts with silicic melt to form hybrid overgrowths of oikocrystic Opx, in the process entraining 'framework' chromite. D T4) Swarms or patches of disaggregated clasts merge resulting in complete hybridization. D1) Chemical re-equilibration takes place between xenocrystic phases (Chr and Ol) and the LWI melt. A is digitized scan (BT-09-46/212), and C is a digitized photomicrograph (BT-09-32/121.5m). B1 is after Perugini and Poli (2012) and T1A-T4D after Beard et al. (2005).

Fig. 25. Th/Yb versus Nb/Yb bivariate plot showing UWZ, BLHZ and BTIC samples, and their mean values with one standard deviation. Sample analysis from this study, Heather et al., *in prep*, and Mehmenesh et al. *in prep*. Reference magmas plotted as cross symbols: Alexo komatiite (AK), the predicted parental komatiite of Eagles Nest (EK; Mungall et al., 2010), N-MORB, E-MORB, and OIB (McDonough and Sun, 1989); Reservoirs plotted as large open circles: Archean (AC; Rudnick and Fountain, 1995), lower (LC), middle (MC), and upper crust (UC; Rudnick and Goa, 2003).

Fig. 26. Proposed model for the emplacement of LWI and the genesis of the BLHZ.

2.15 Figures

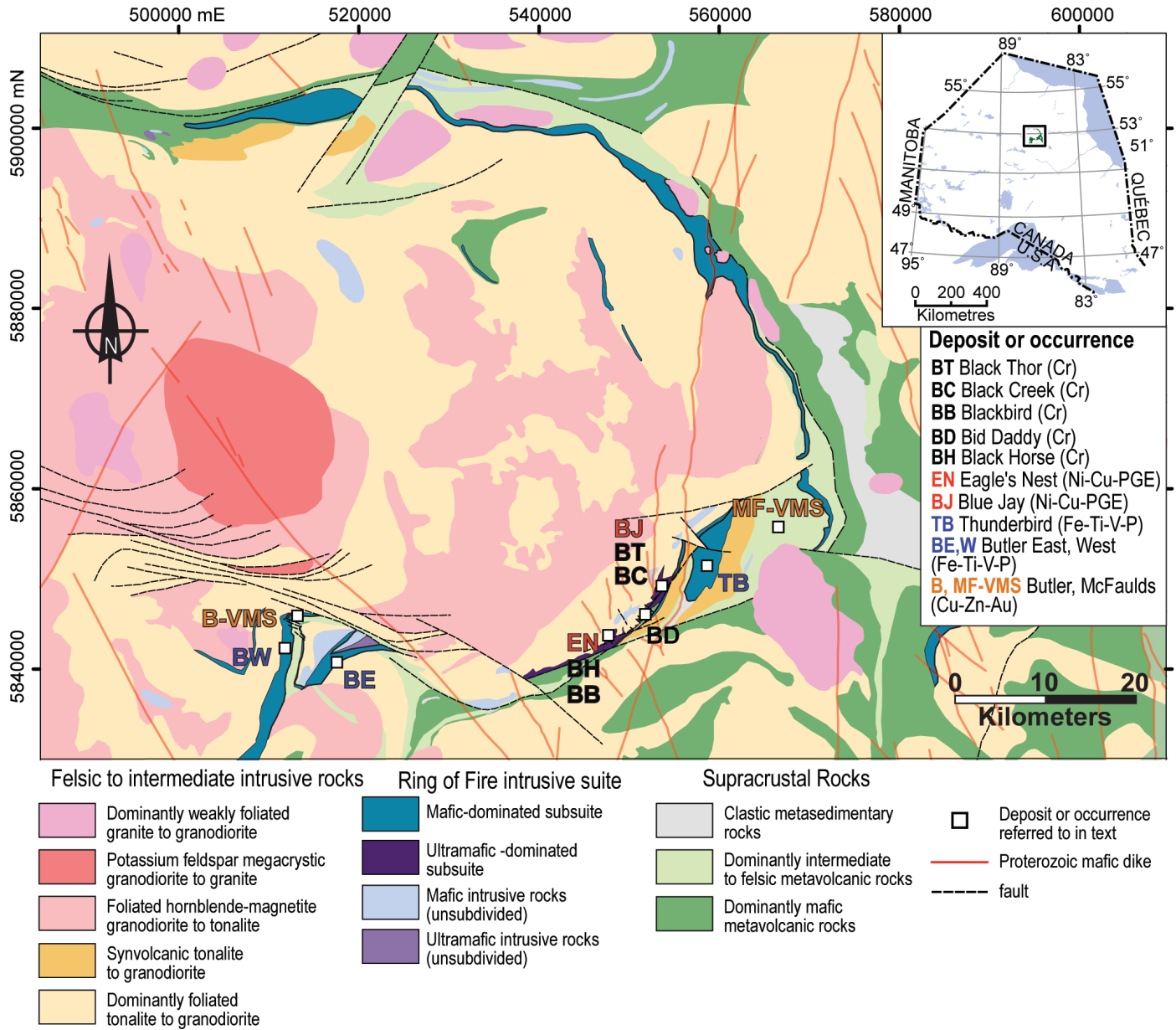


Figure 1.

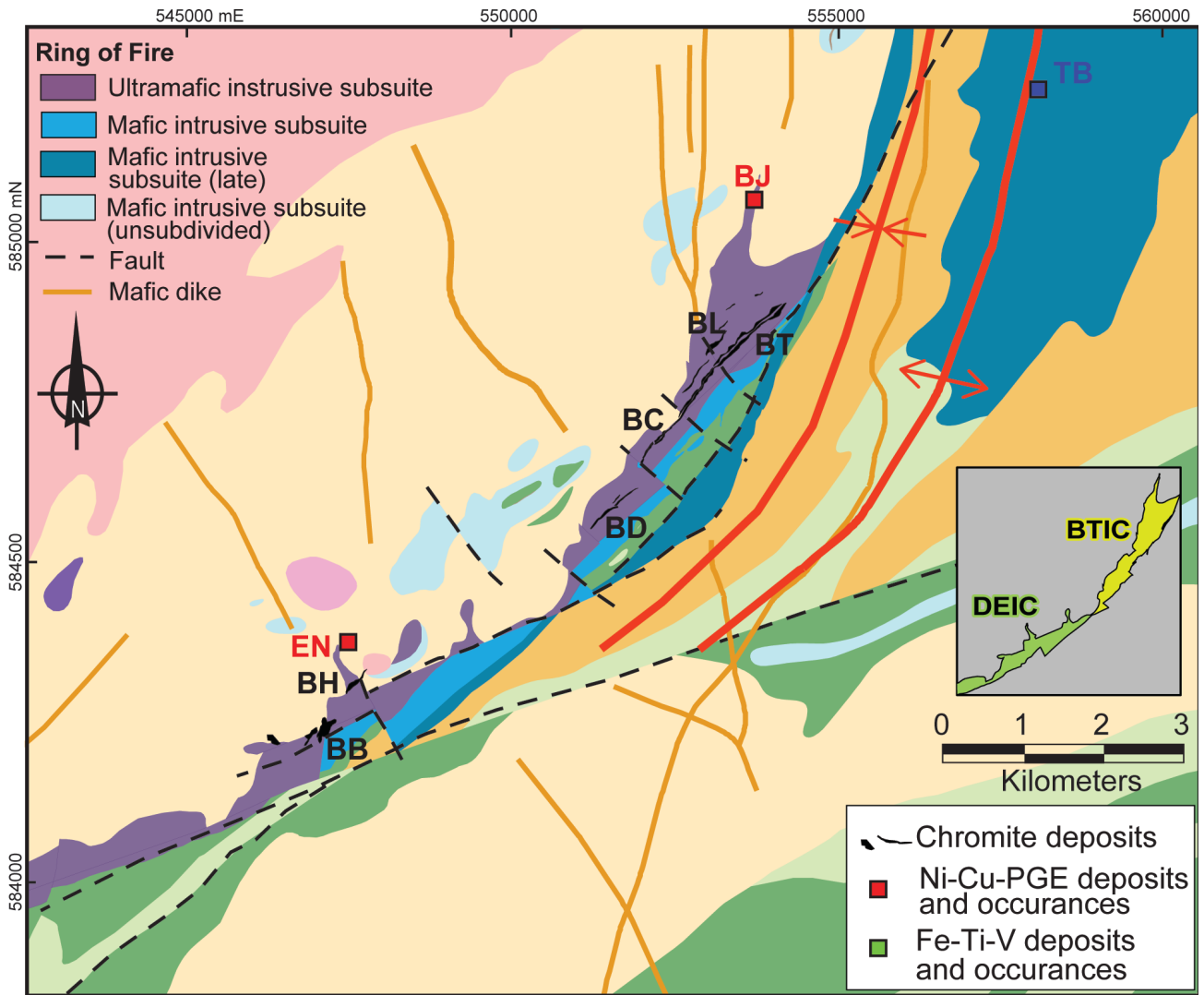
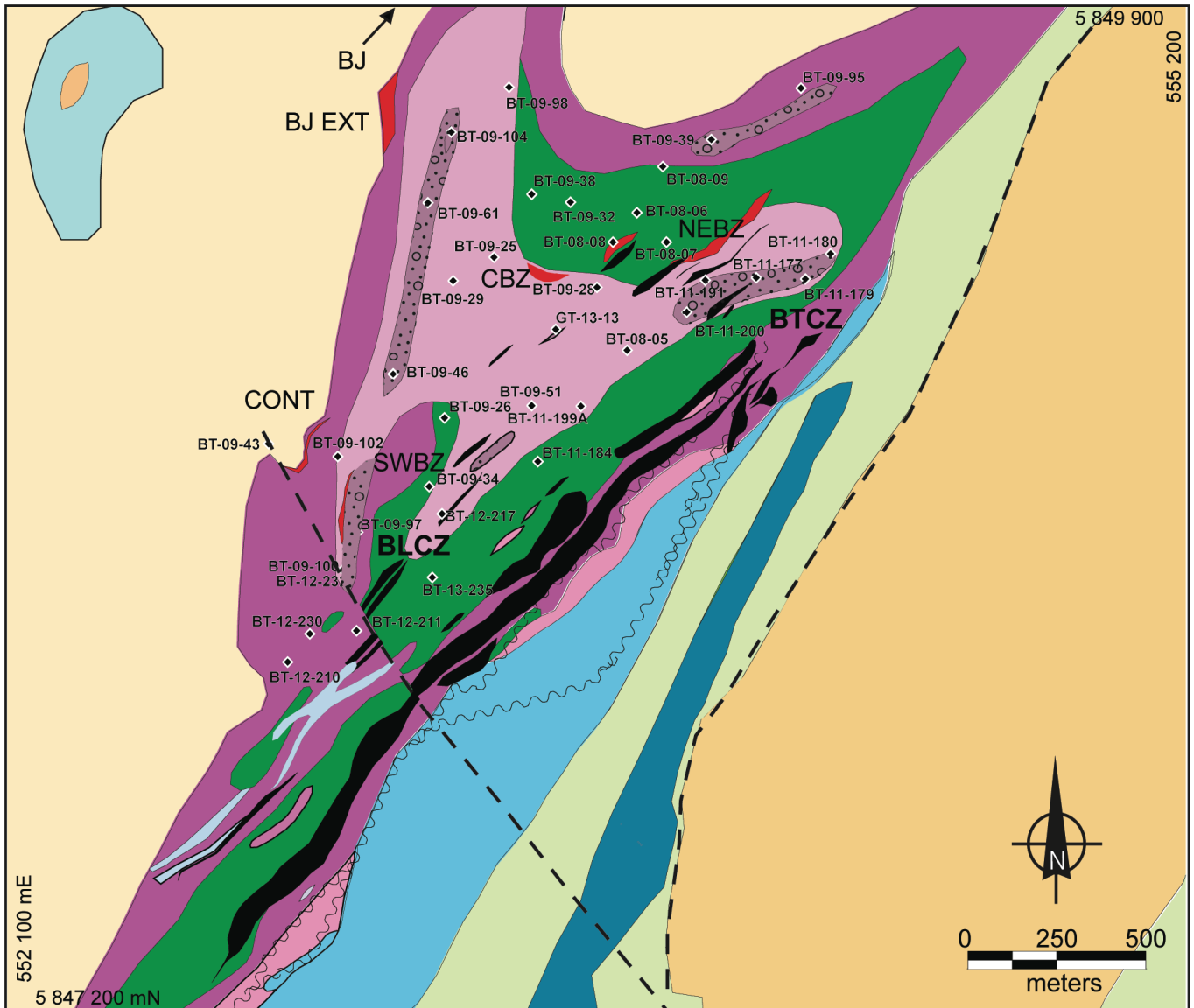


Figure 2.



Footwall Rocks	LWI	BTIC	Felsic-Mafic Intrusive Rocks
Granodiorite	Websterite to gabbronorite	Melano-anorthositic gabbro	Biotite gabbro
Synvolcanic gabbro	Hybrid rocks	Pyroxenite	Ferrogabbro
Iron formation		Lherzolite	Tonalite
Hangingwall Rocks	Chromite mineralization	Dunite	Shear zone
Mafic to intermediate metavolcanic rocks	Sulfide mineralization	Drill hole collar	Fault

Figure 3.

McFaulds Lake Greenstone Belt	Hanging Wall		Basalt, Andesite, Rhyolite		
			Granodiorite		
	Mafic Intrusive		Ferrogabbro (2734.5 ± 1 Ma) ¹		
	Hanging Wall		Basalt, Rhyolite (2737 ± 7 Ma) ²		
	Black Thor Intrusive Complex	Mafic		Mela-leuo-anorthostitic Gabbro	
		Ultramafic	Upper	Websterite	
				Black Thor Chromitite Zone	
			Middle	Dunite ± Lherzolite, Harzburgite, Olivine Websterite, Websterite	
		(Biotite)-Websterite, Lherzolite Black Label Chromitite Zone			
		Lower	Dunite ± Lherzolite, Harzburgite, Olivine Websterite, Websterite		
Basal	Marginal	Olivine Websterite, Lherzolite	Late Websterite		
	Feeder	Websterite Feeder			
Footwall		Granodiorite, Tonalite (2773 ± 1 Ma) ¹ Iron Formation, Basalt, Gabbro			

Figure 4.

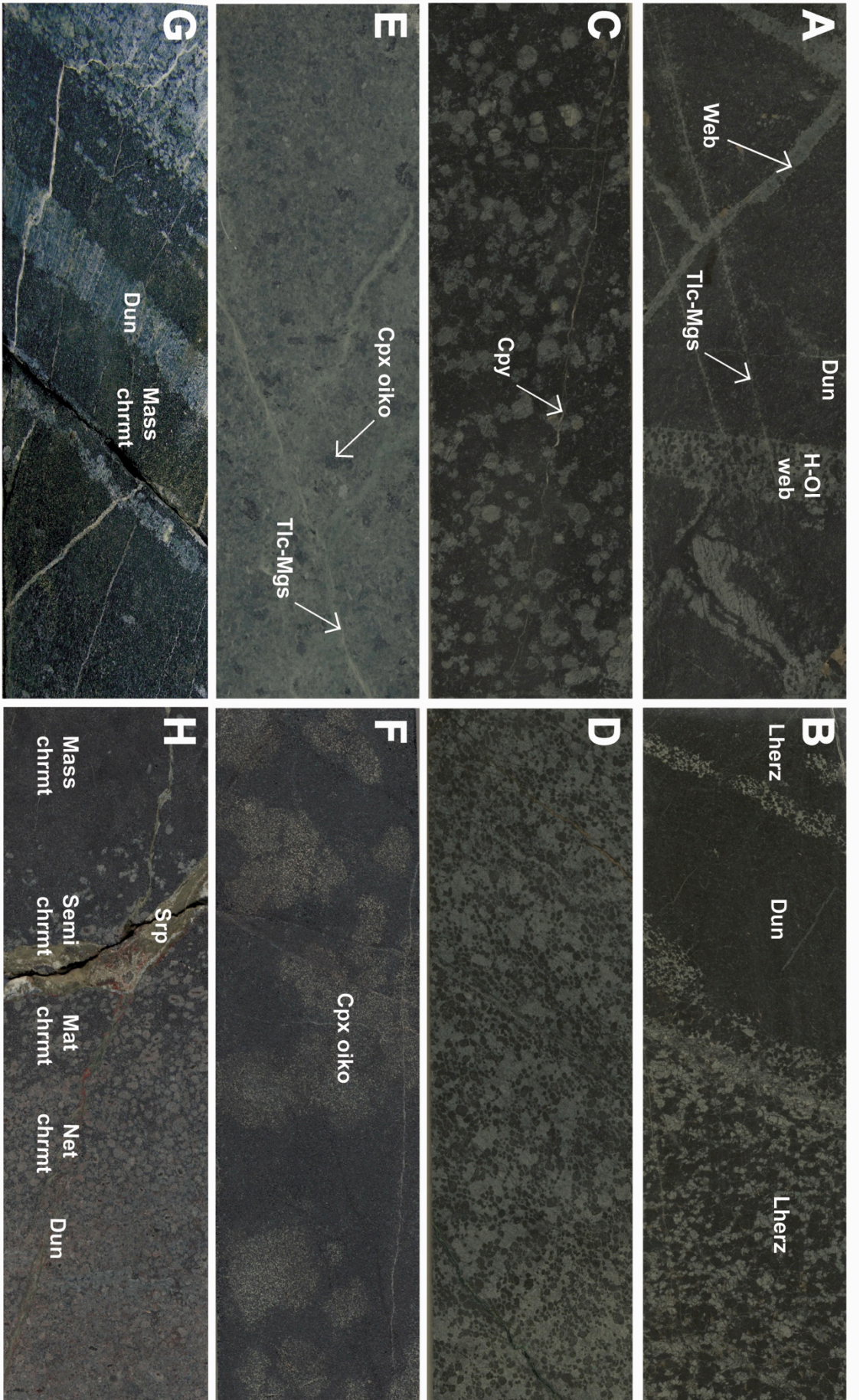


Figure 5.

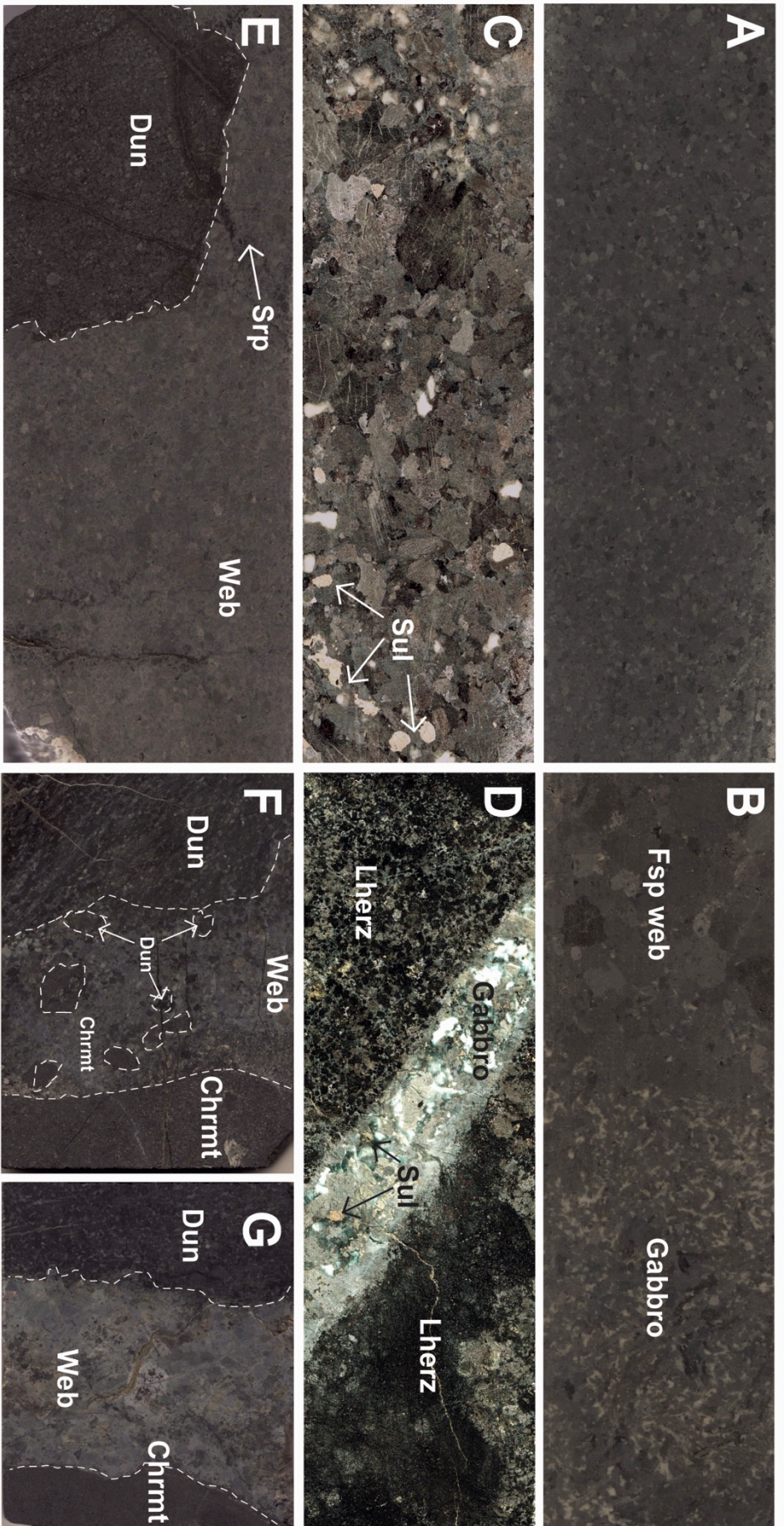


Figure 6.

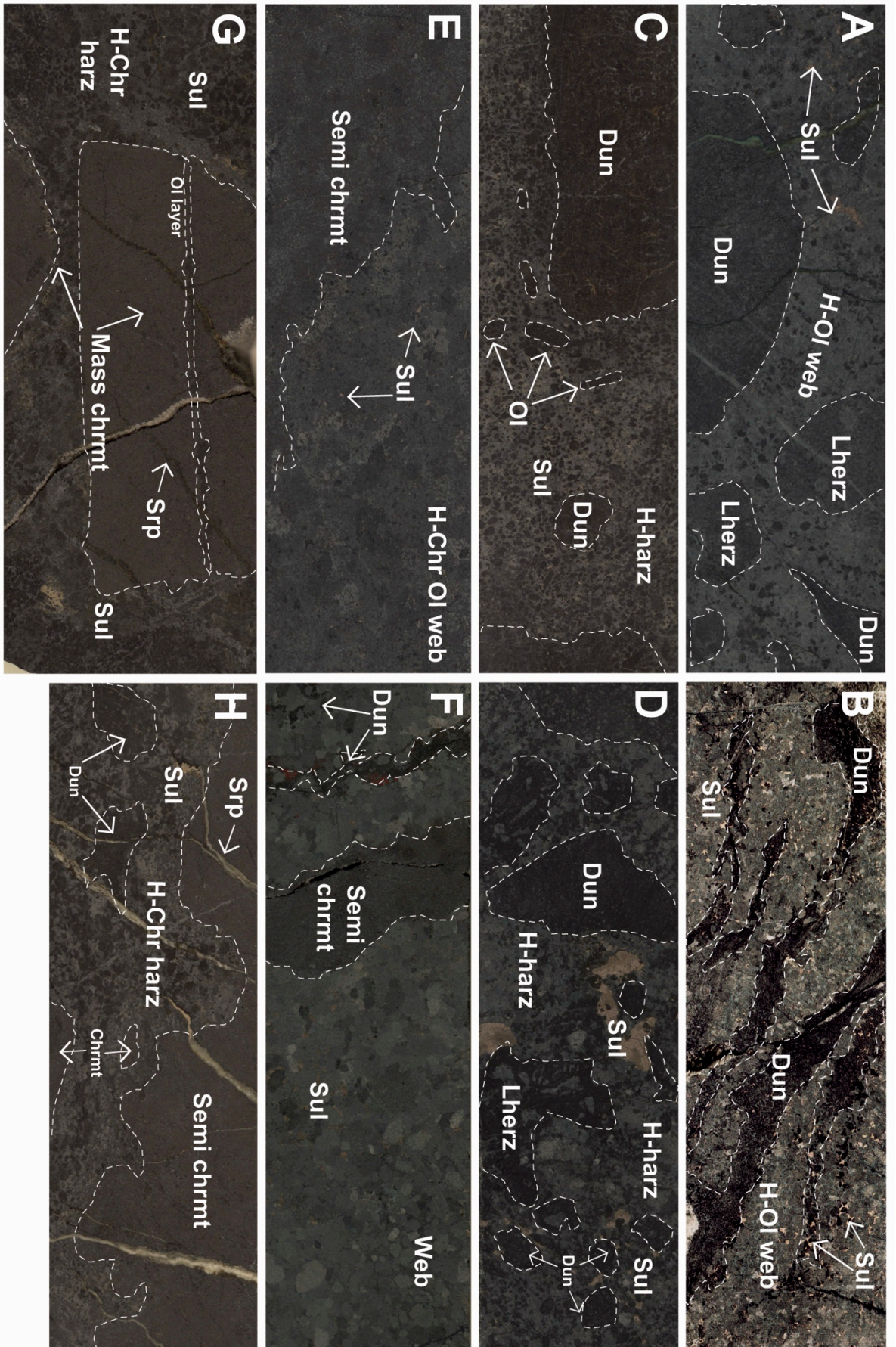


Figure 7.



Figure 8.
69

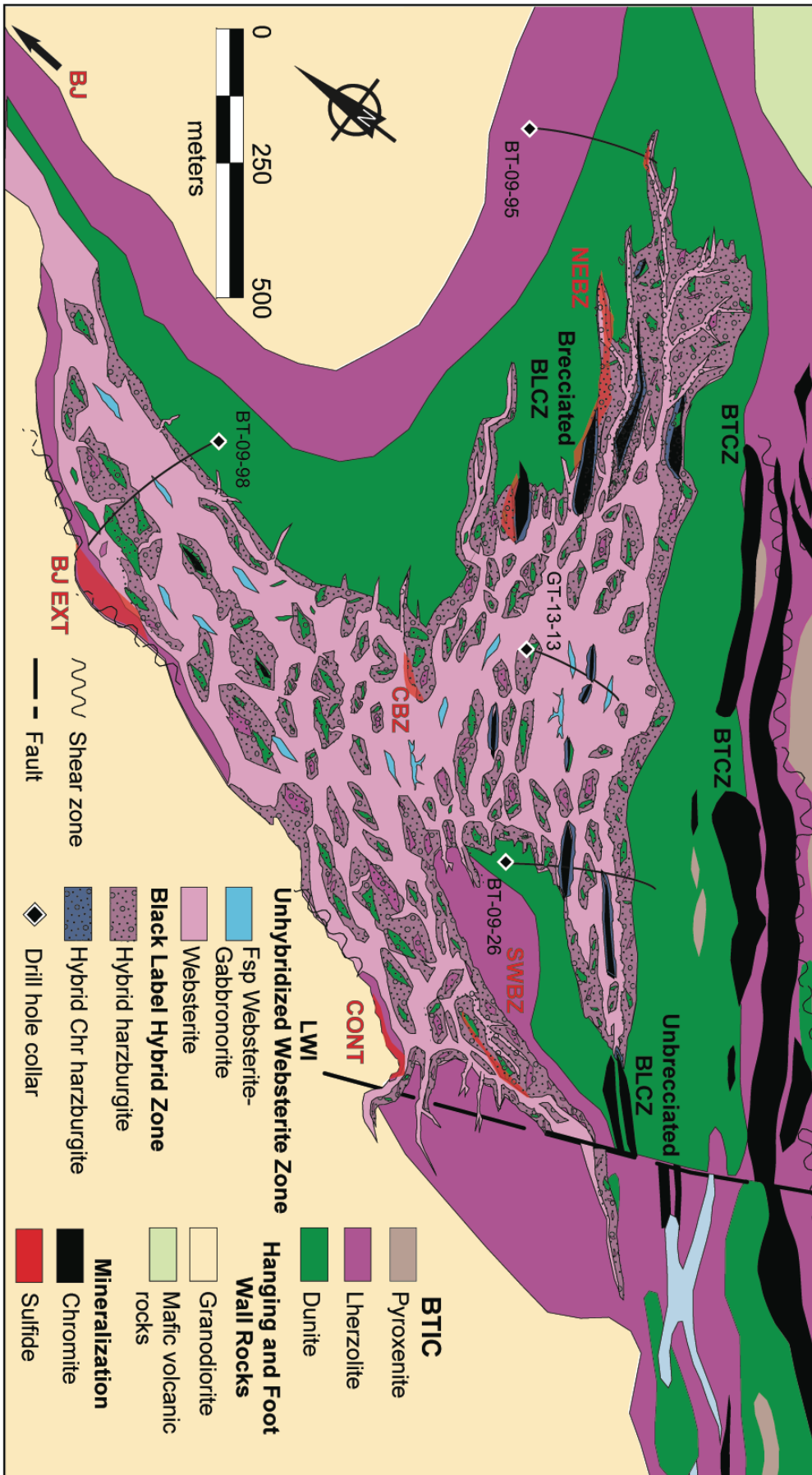
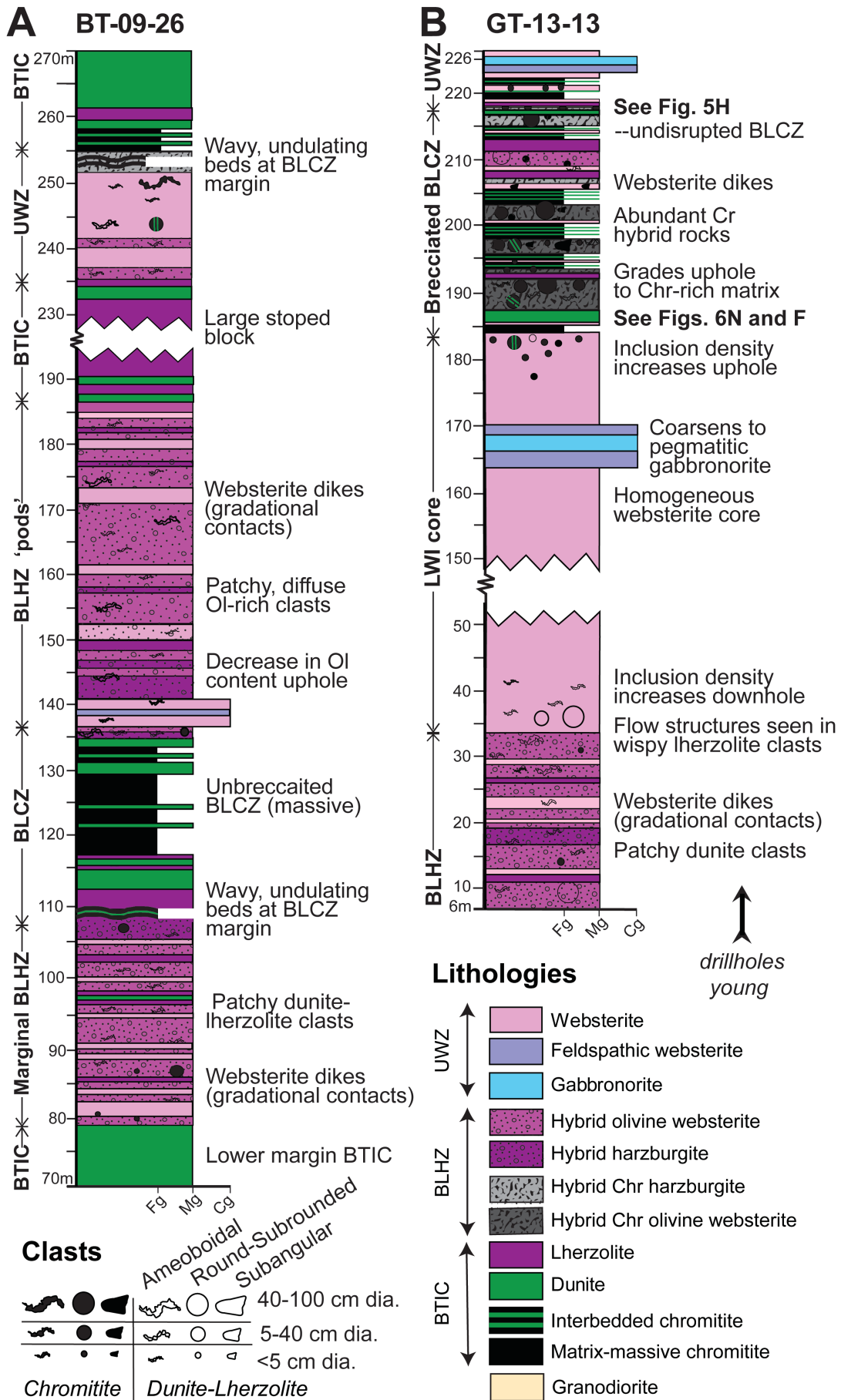


Figure 9.



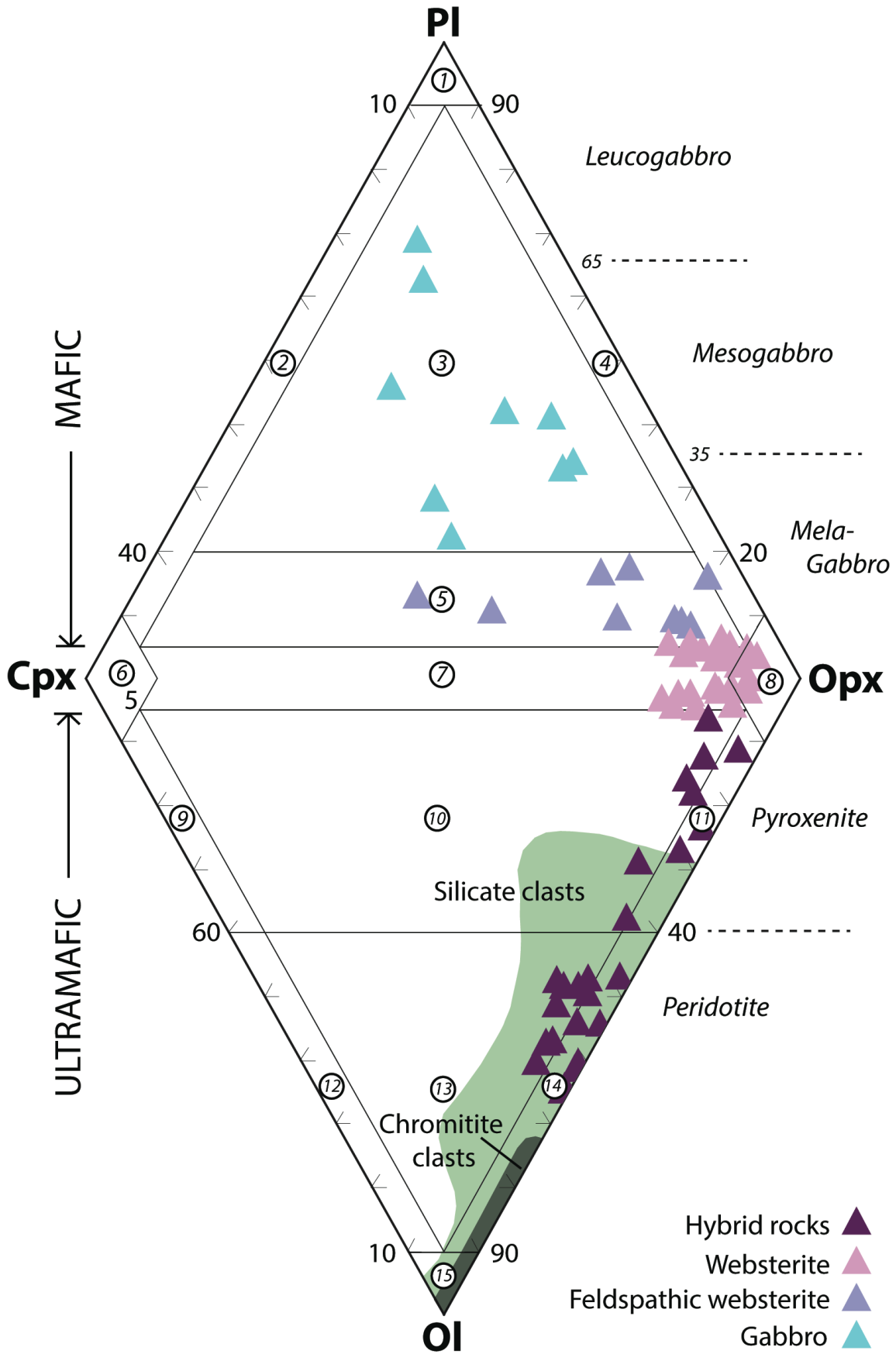


Figure 12.

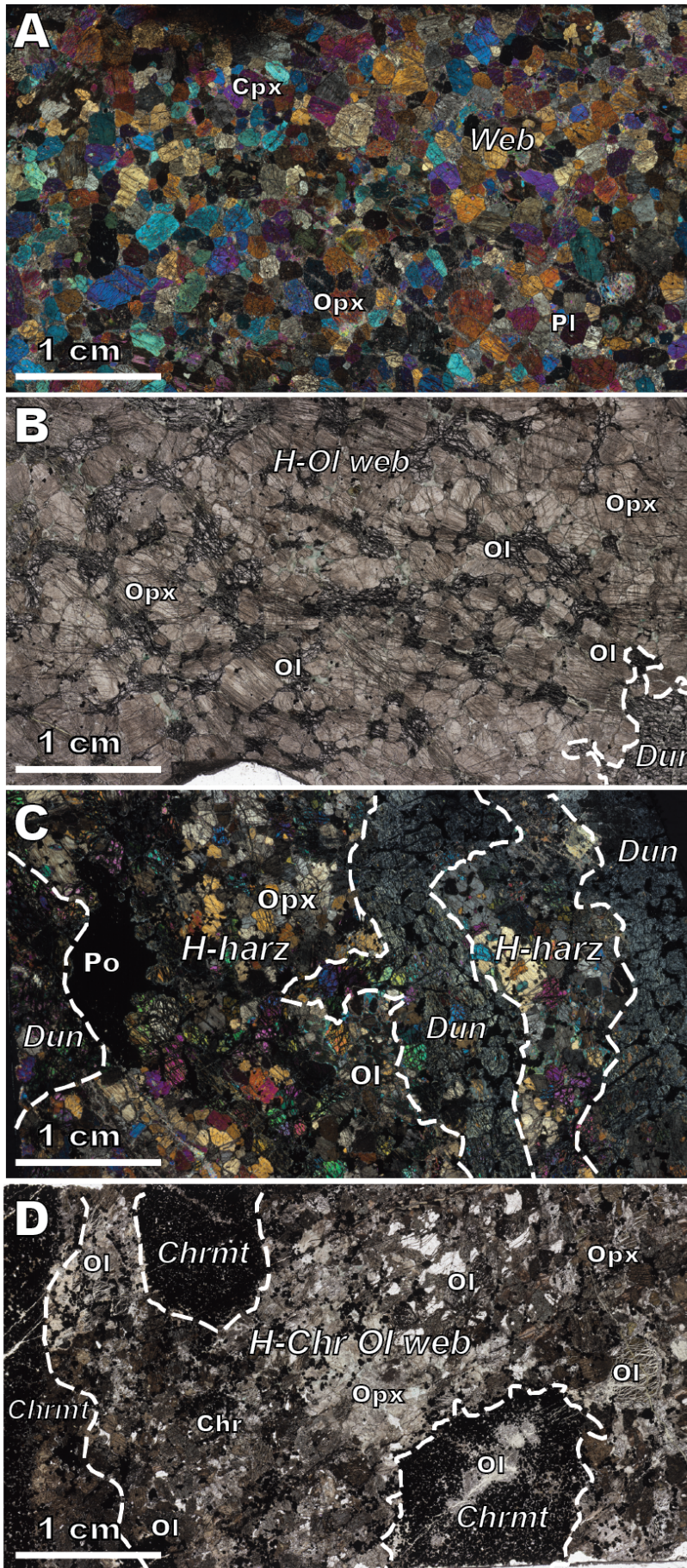


Figure 13.

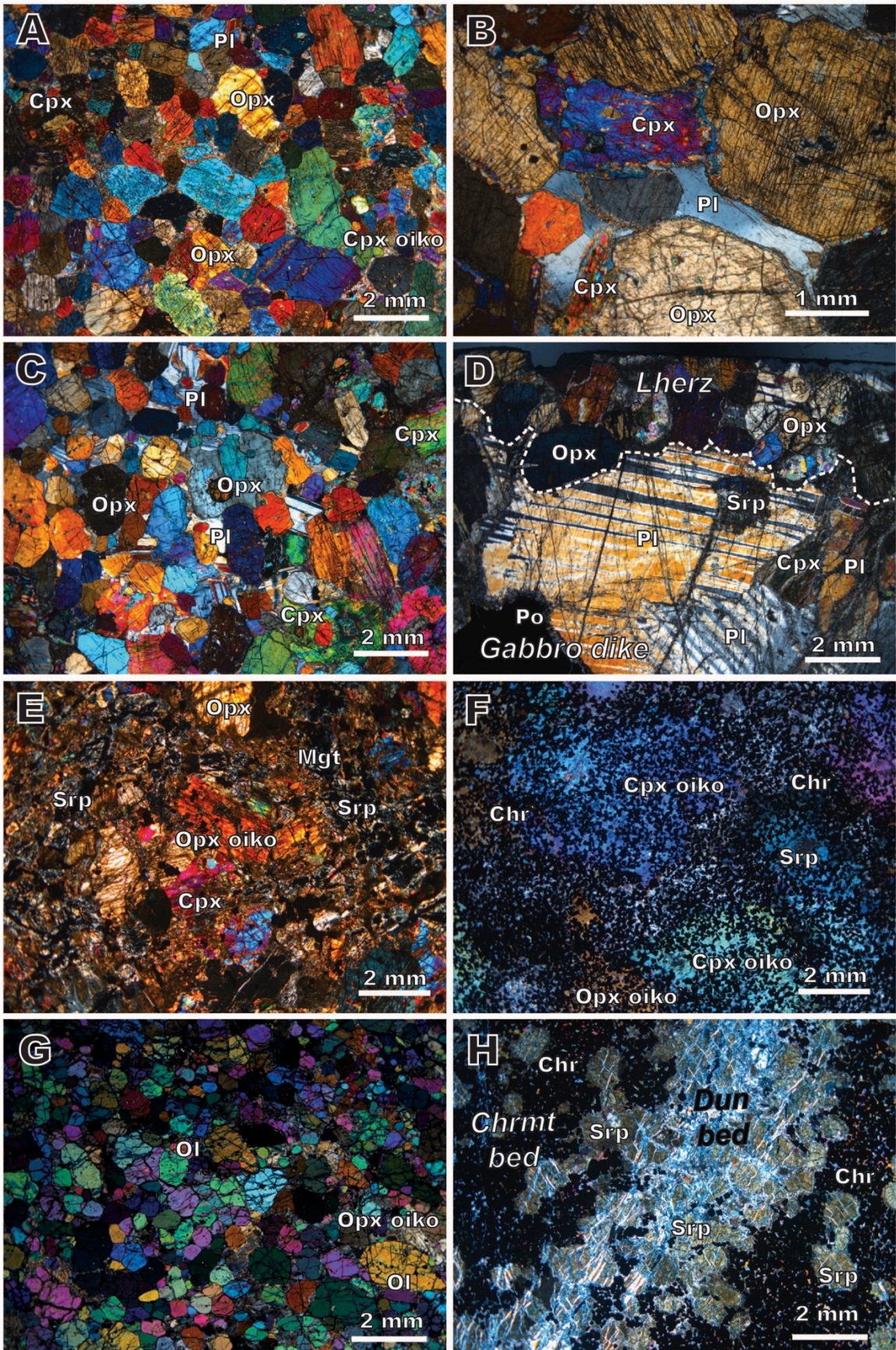


Figure 14.

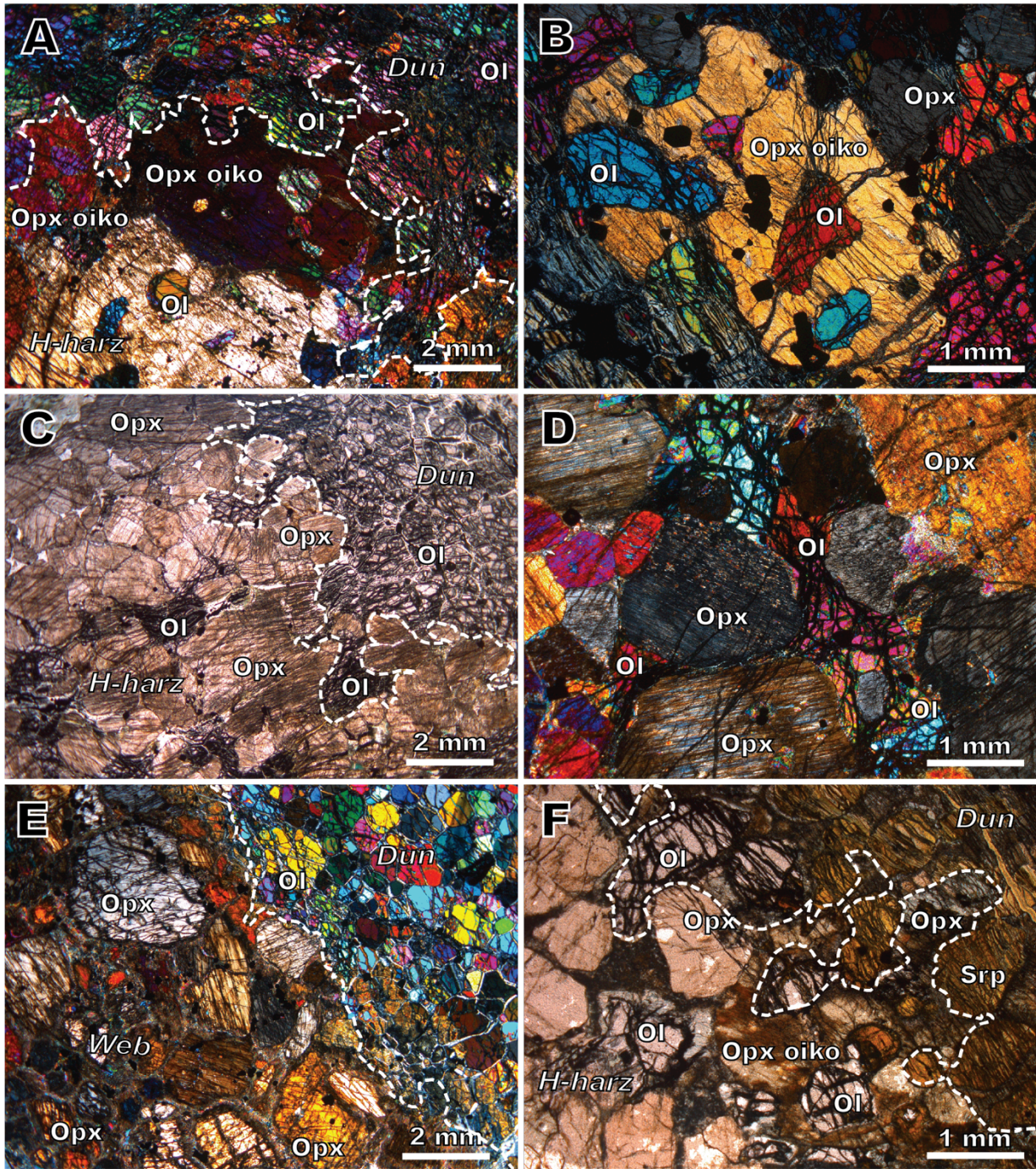


Figure 15.

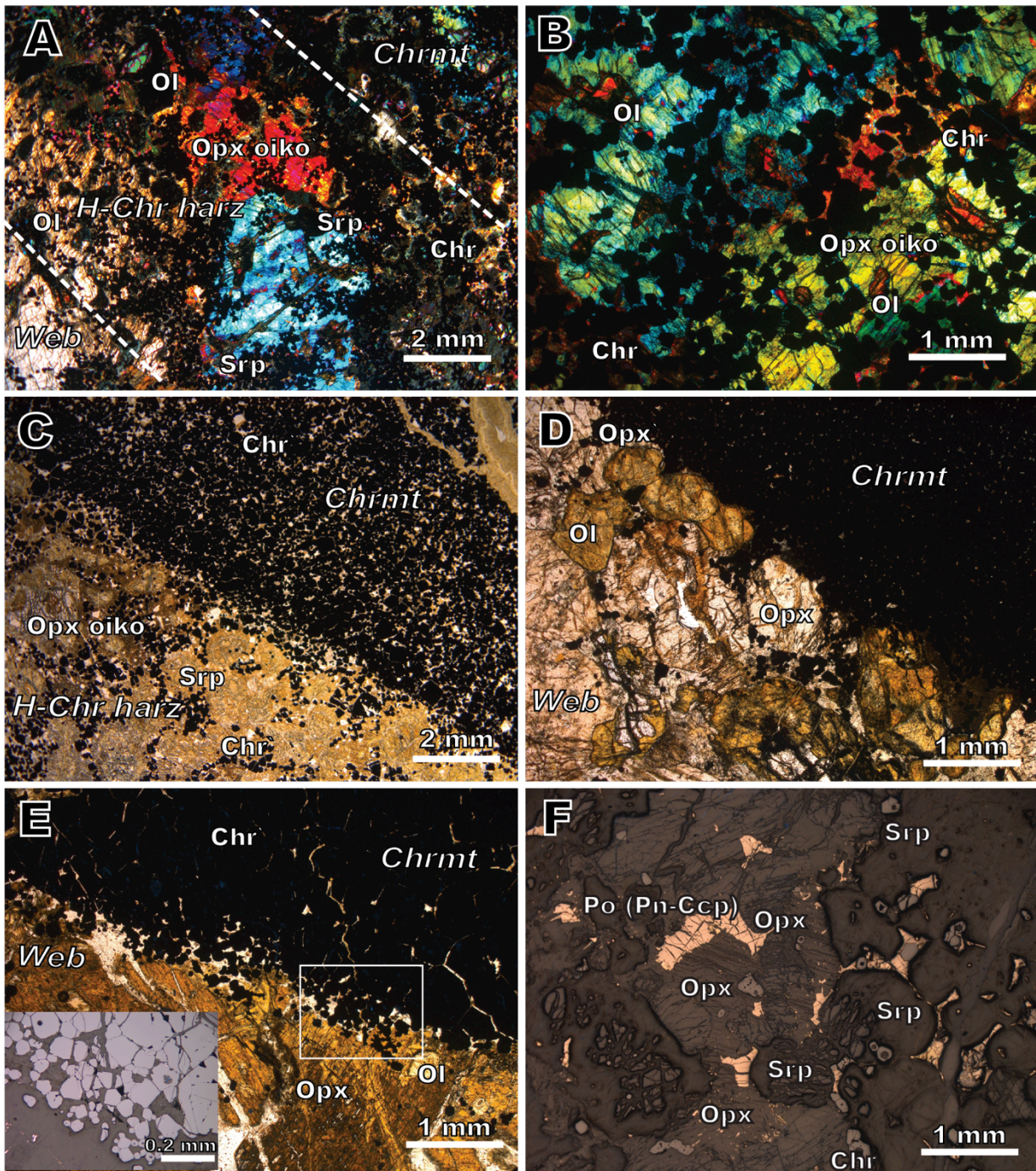


Figure 16.

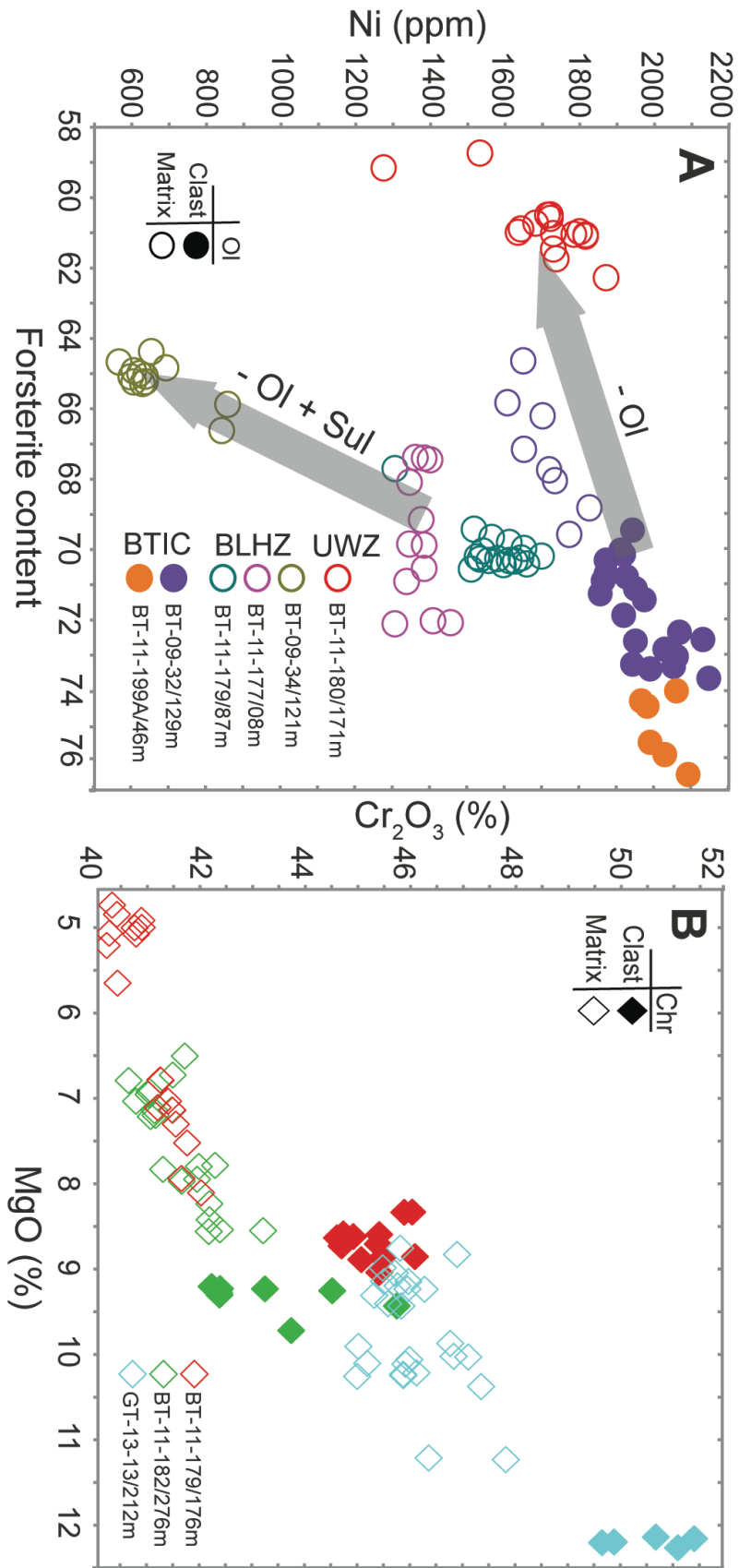


Figure 17.

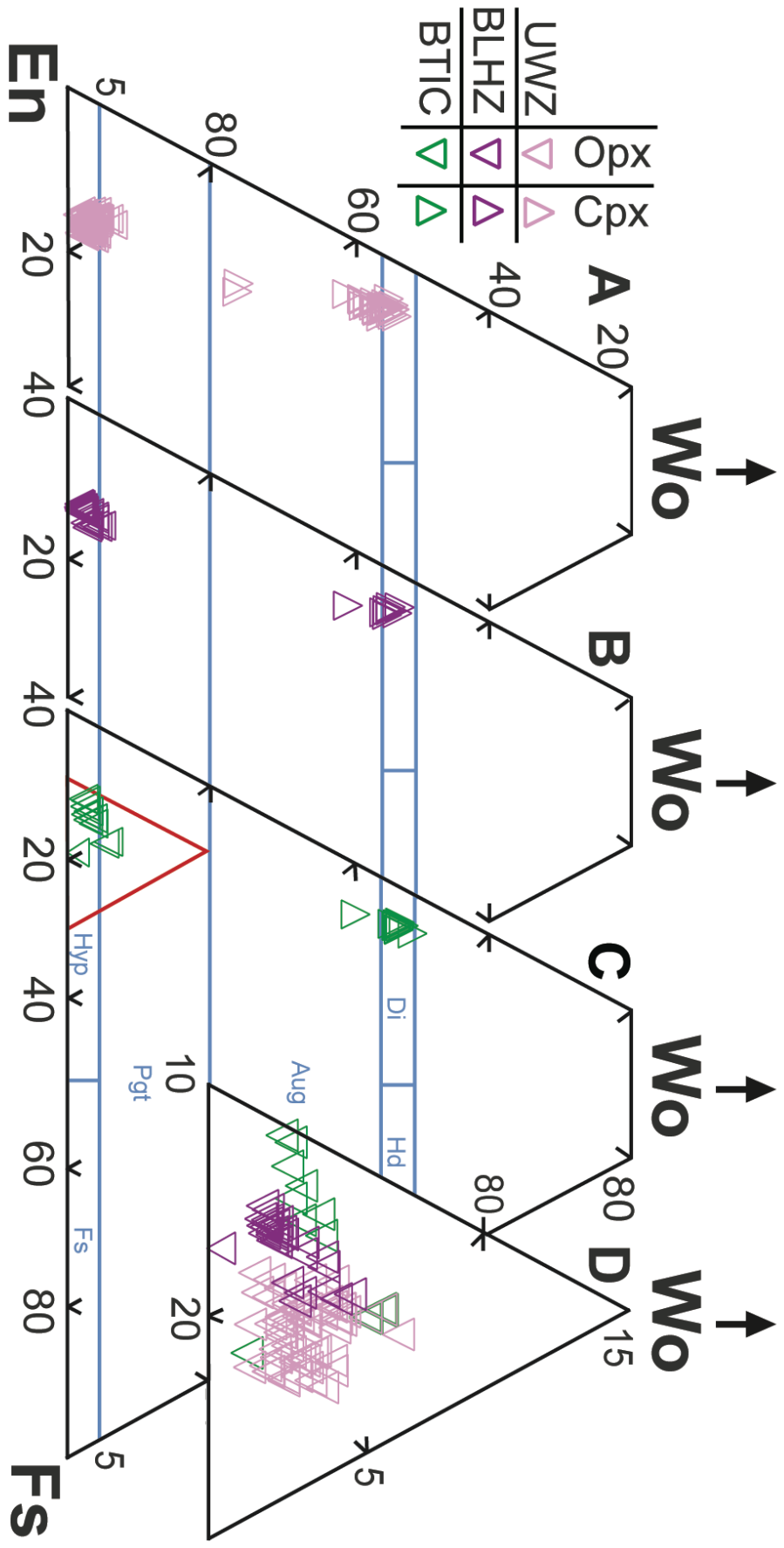


Figure 18.

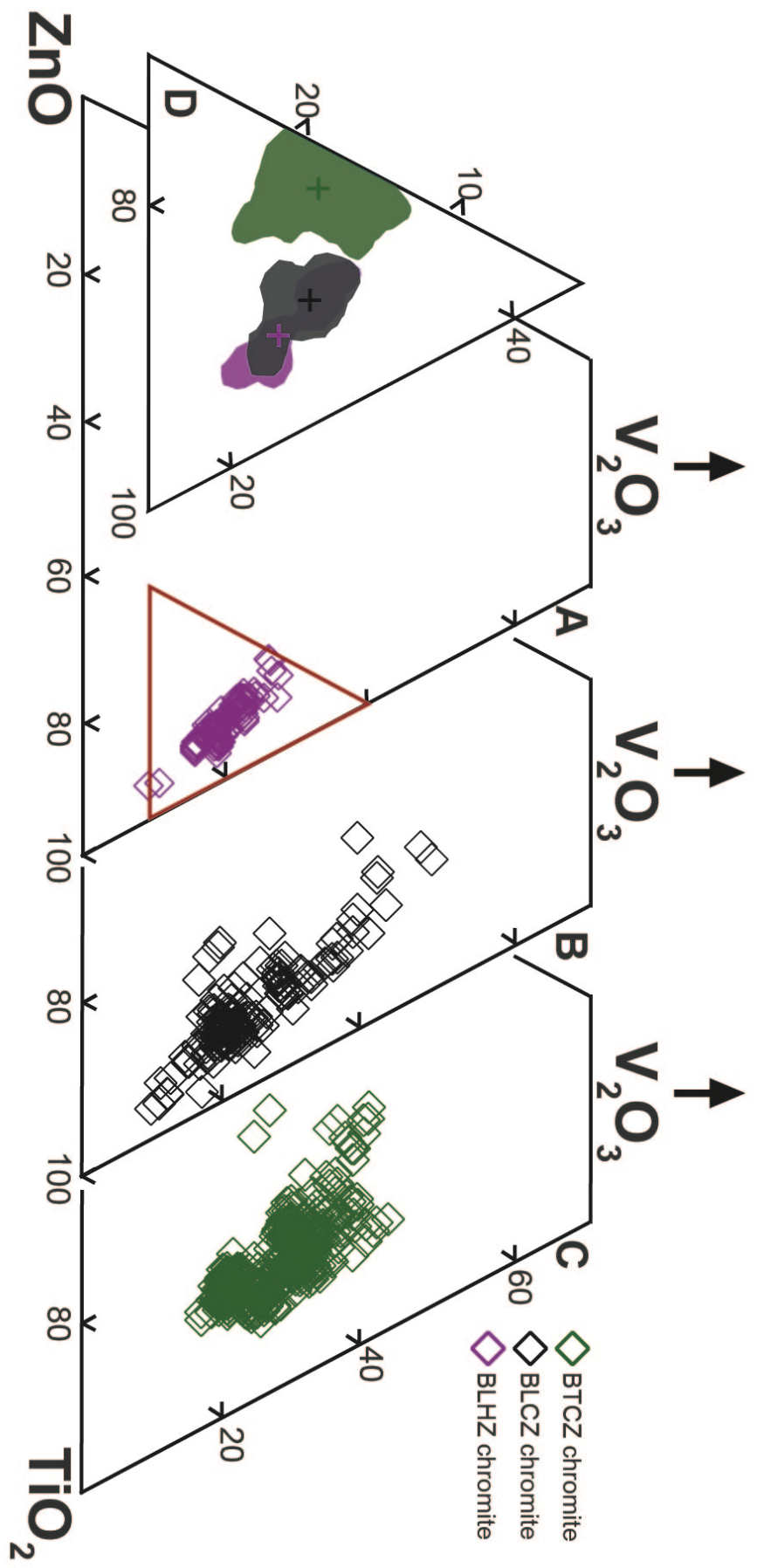


Figure 19.

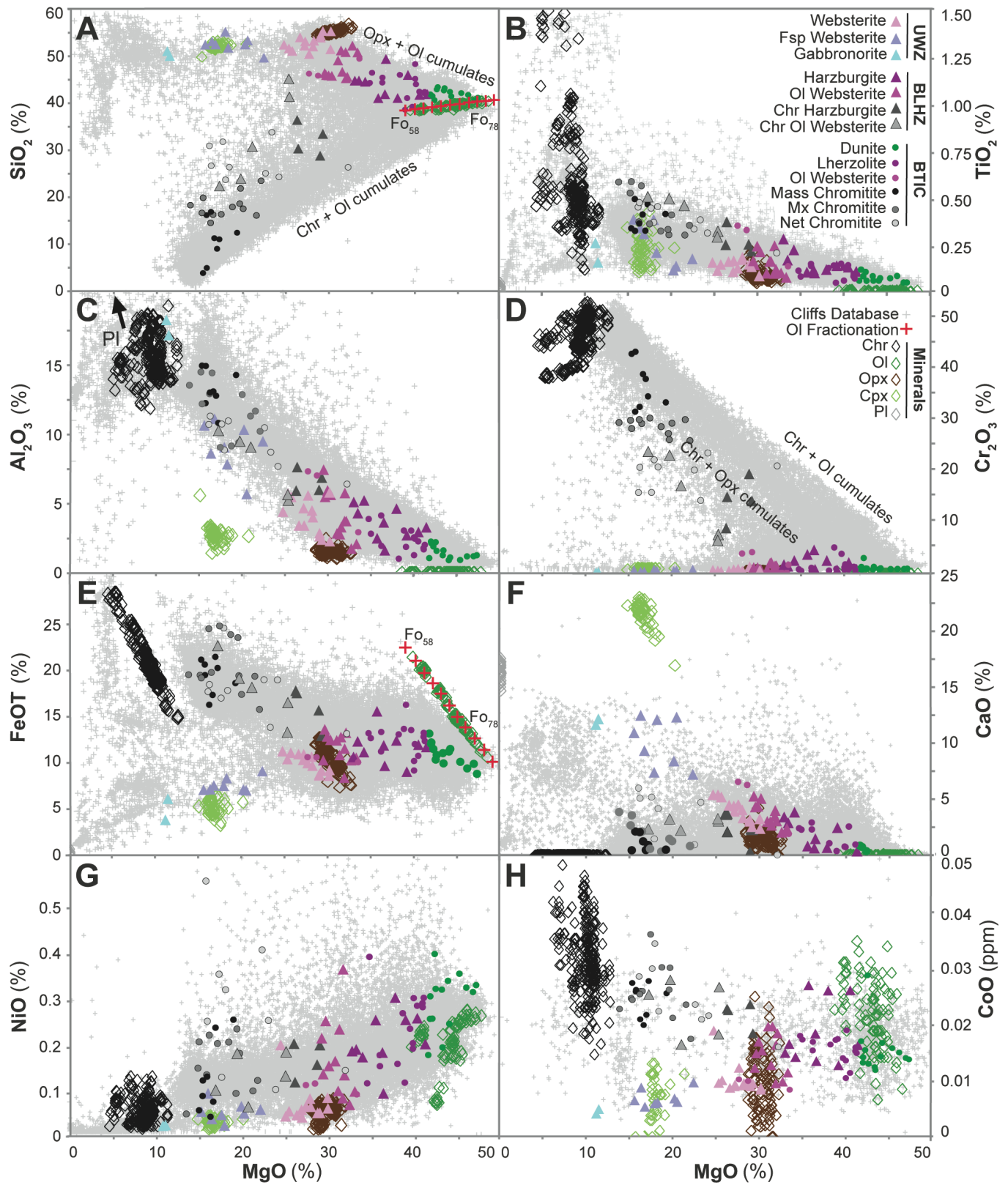


Figure 20.

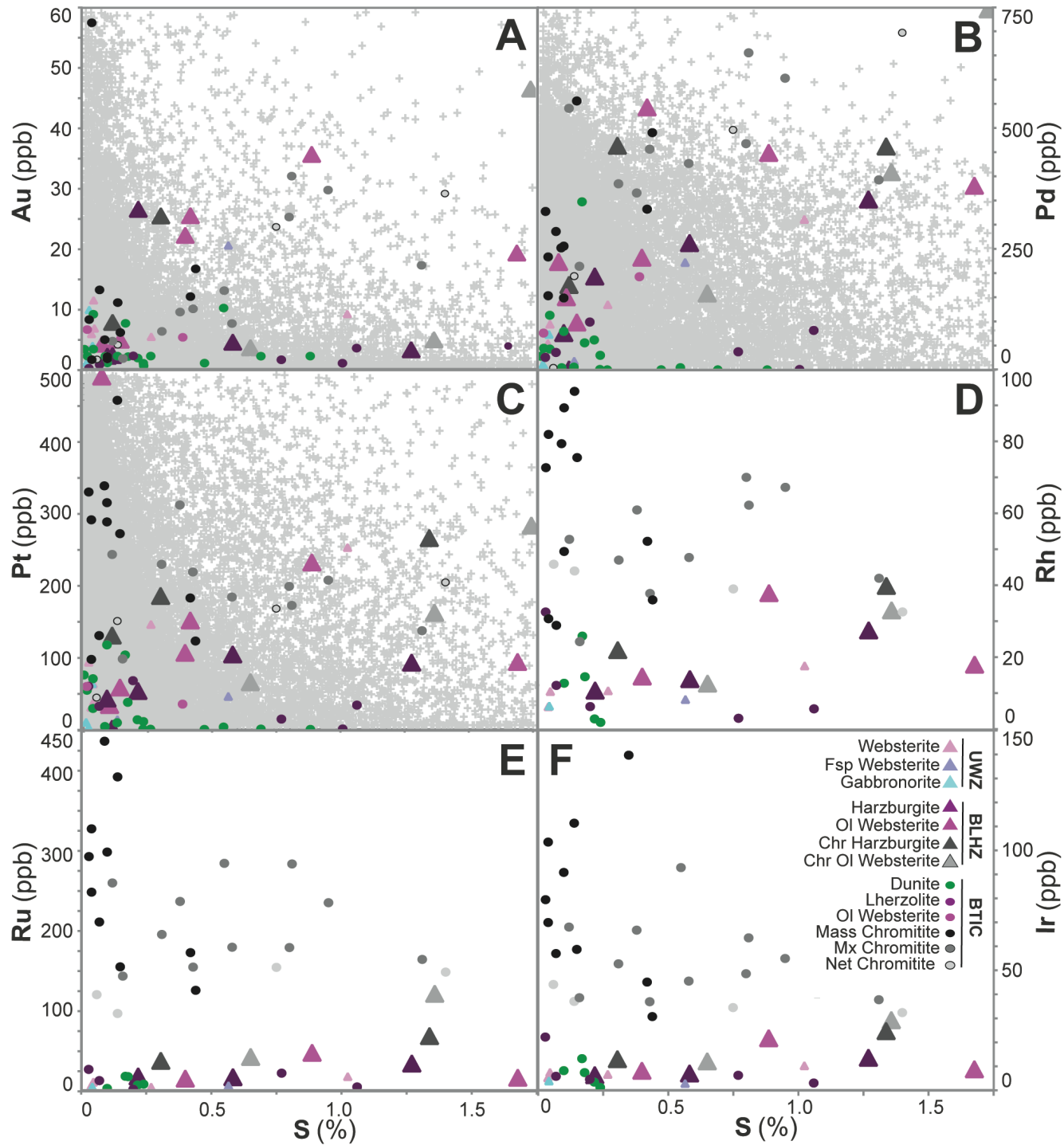


Figure 21.

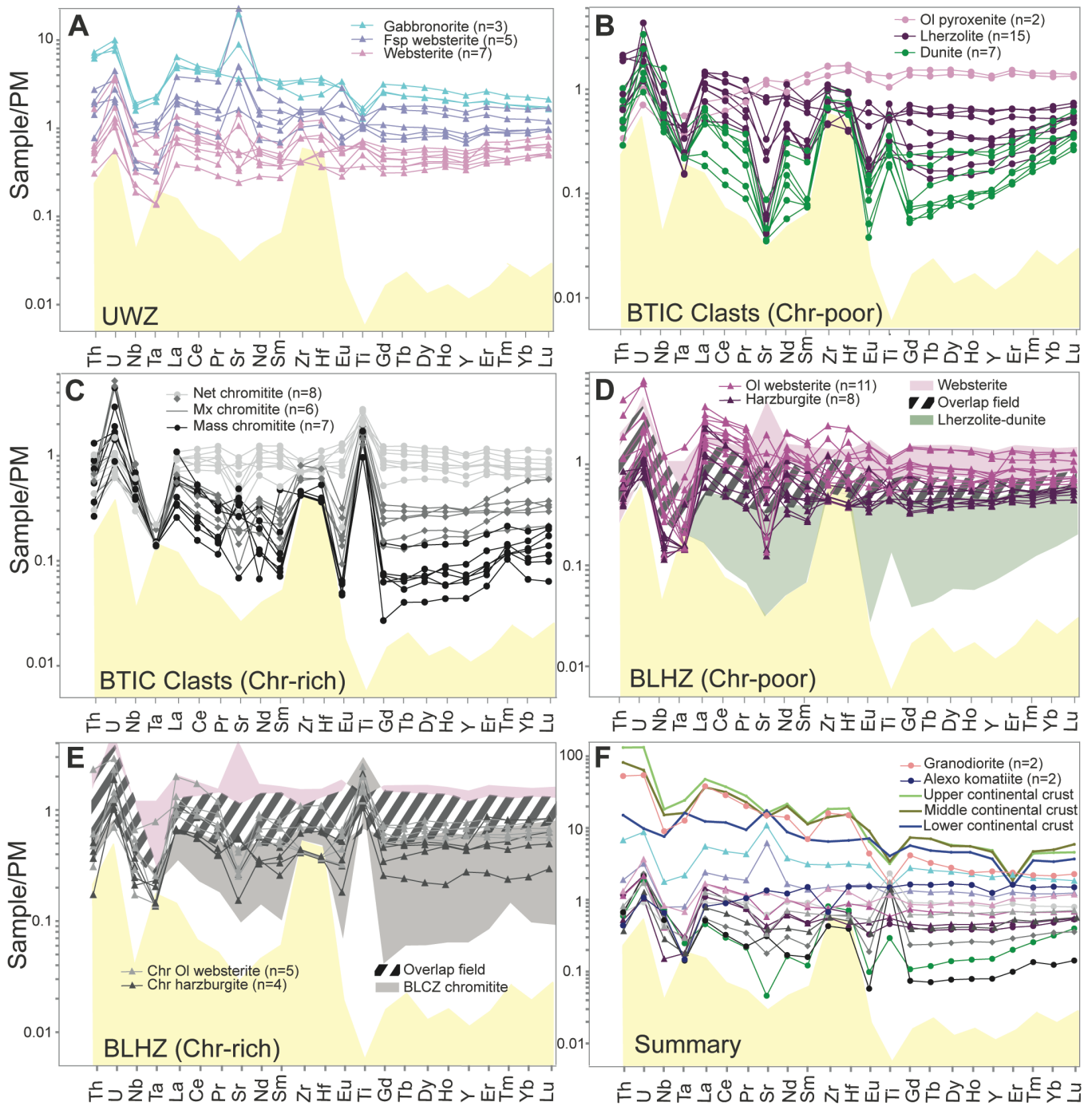


Figure 22.

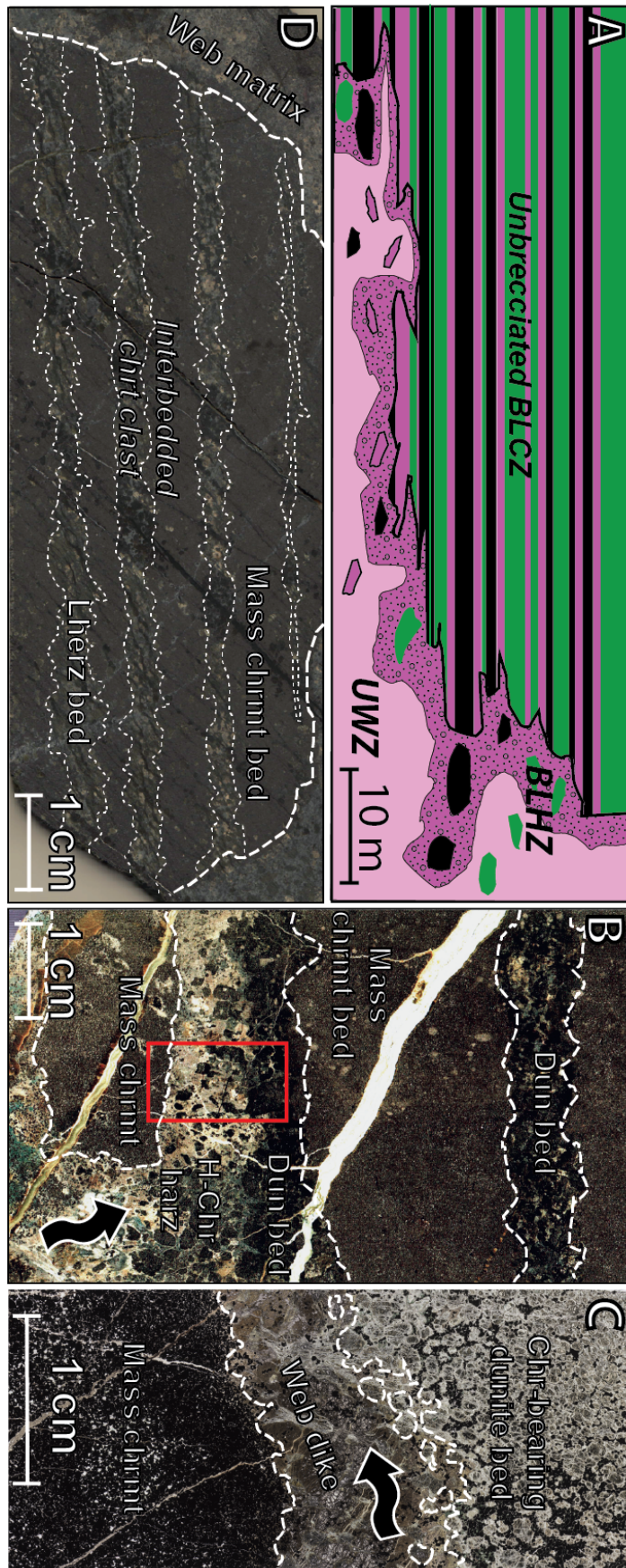


Figure 23.

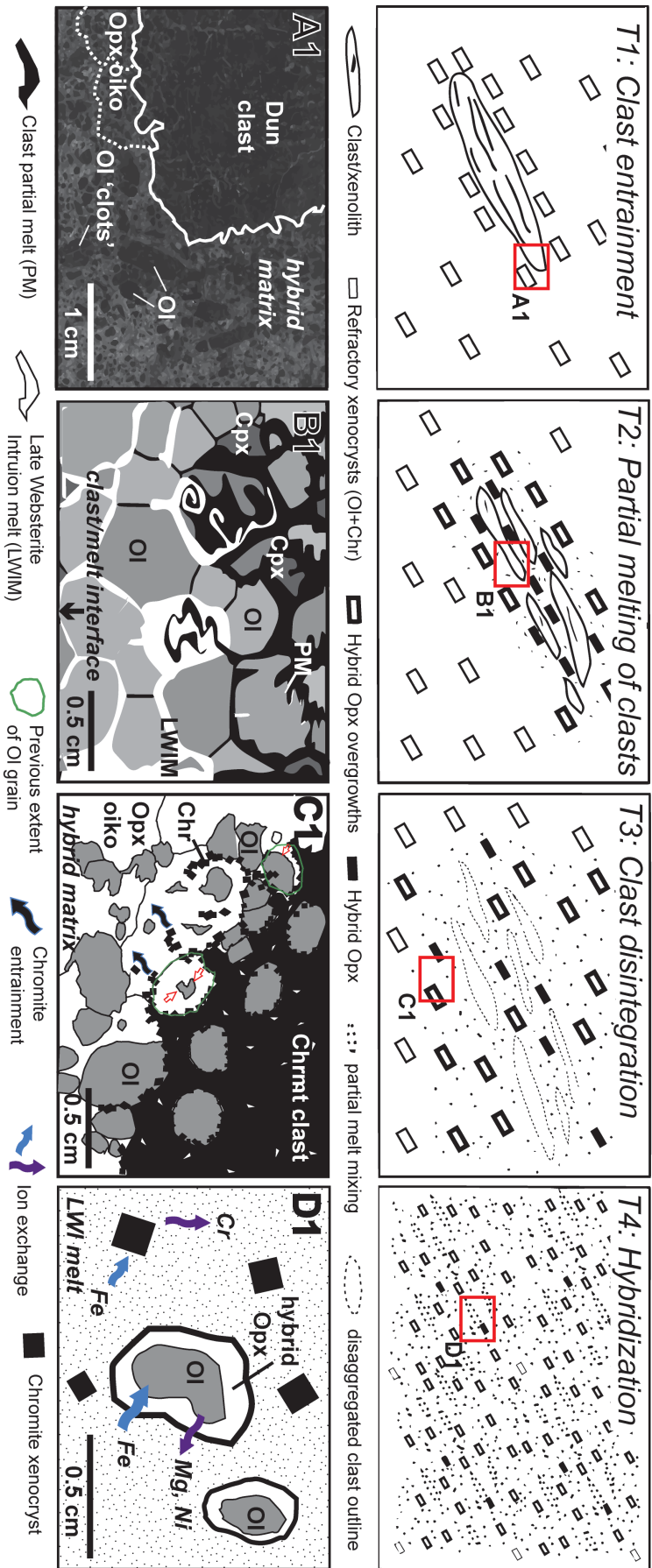


Figure 24.

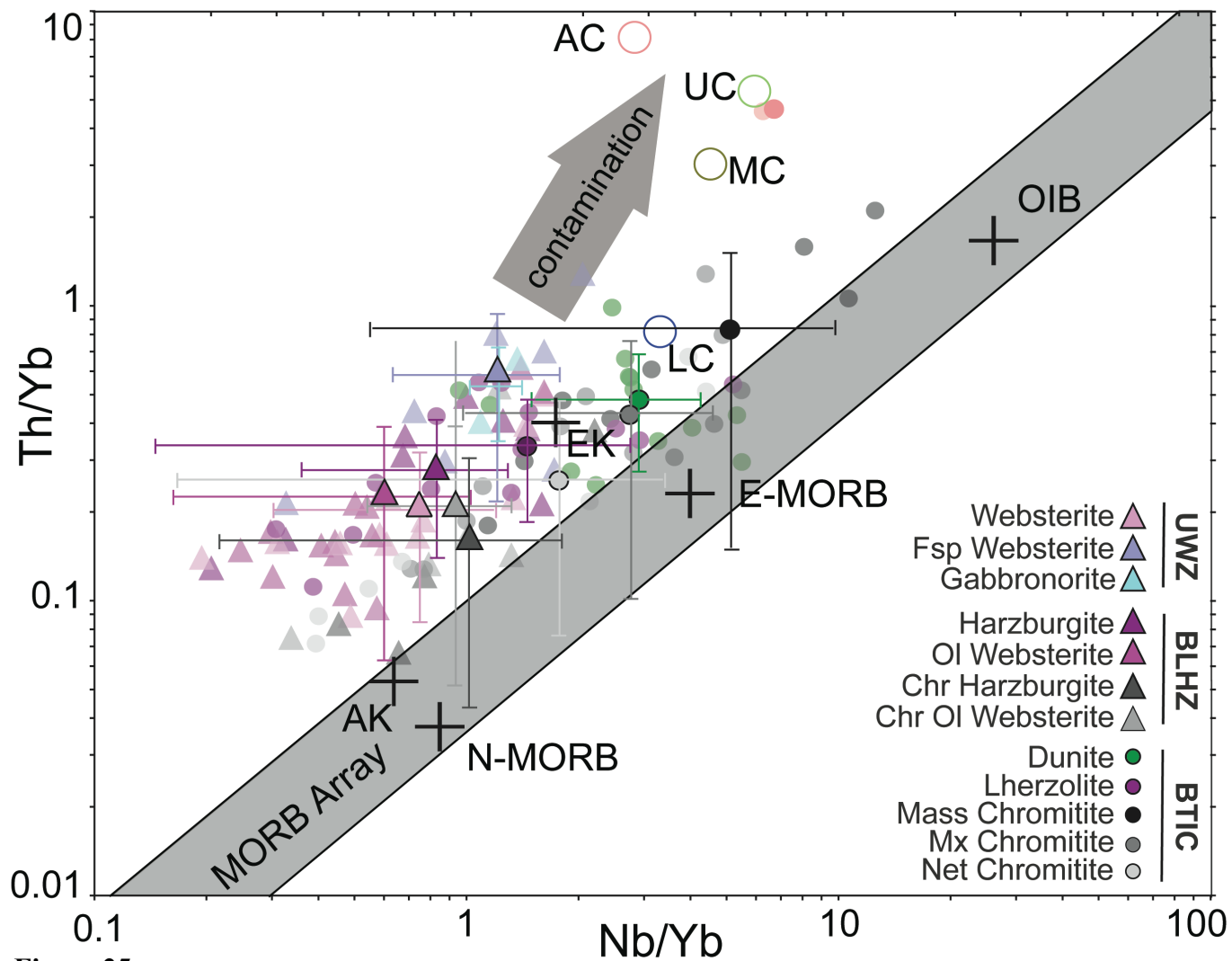


Figure 25.

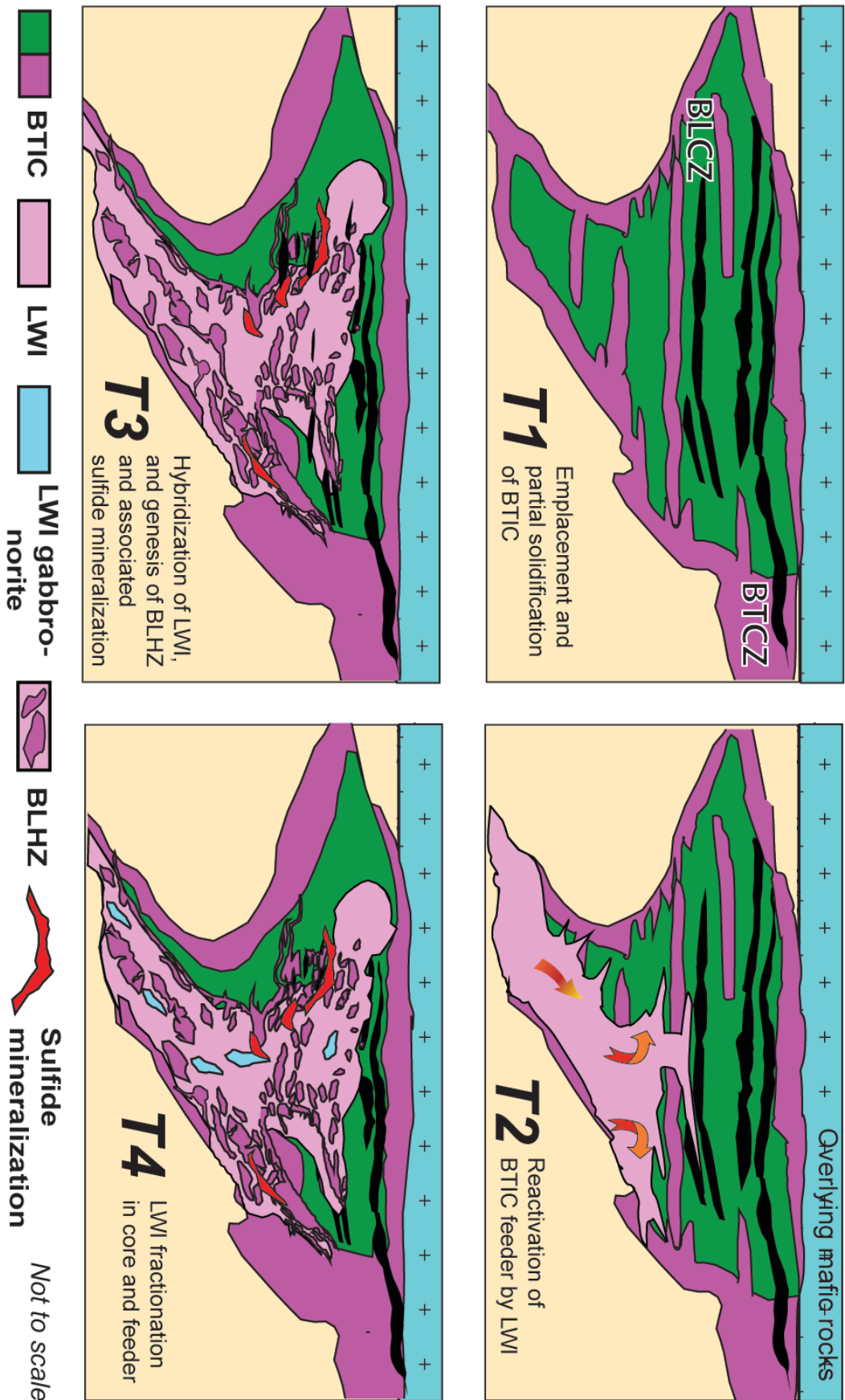


Figure 26.

Sample ID	Mineral	DDH	Depth(m)	SiO2	TiO2	Al2O3	Cr2O3	FeO(T)	MnO	CaO	NiO	MgO	CaO	Na2O	K2O	Total
Unit				wt %	wt %	wt %	wt %	wt %	wt %	wt %	wt %	wt %	wt %	wt %	wt %	wt %
Detection Limit																
110071 OI	BT-09-32		129.00	39.973	<0.007	<0.006	0.008	0.032	0.012	0.012	0.008	0.012	0.005	0.005	0.012	100.14
110071 OI	BT-09-32		129.00	39.861	0.008	0.017	0.008	14.799	0.220	0.016	0.232	44.862	0.018	<0.005	<0.012	100.08
110071 OI	BT-09-32		129.00	39.854	<0.007	<0.006	0.012	15.247	0.216	0.027	0.232	44.819	0.009	<0.005	<0.012	100.12
110071 OI	BT-09-32		129.00	39.854	<0.007	<0.006	0.013	17.220	0.228	0.016	0.231	43.419	0.009	<0.005	<0.012	100.04
110071 OI	BT-09-32		129.00	39.843	<0.007	<0.006	0.013	15.201	0.222	0.016	0.247	45.204	0.016	<0.005	<0.012	100.05
110071 OI	BT-09-32		129.00	39.740	<0.007	<0.006	0.006	14.870	0.232	0.024	0.238	45.284	0.024	<0.005	<0.012	100.52
110071 OI	BT-09-32		129.00	39.6918	<0.007	<0.006	0.016	14.483	0.243	0.021	0.238	45.200	0.016	<0.005	<0.012	99.97
110071 OI	BT-09-32		129.00	39.662	<0.007	<0.006	0.008	14.483	0.227	0.025	0.238	45.266	0.009	<0.005	<0.012	99.96
110071 OI	BT-09-32		129.00	40.079	<0.007	<0.006	0.013	14.362	0.230	0.025	0.237	45.121	0.009	<0.005	<0.012	100.06
110071 OI	BT-09-32		129.00	39.860	<0.007	<0.006	0.009	15.425	0.225	0.025	0.234	45.591	0.009	<0.005	<0.012	100.31
110071 OI	BT-09-32		129.00	40.171	<0.007	<0.006	0.010	14.148	0.229	0.021	0.238	45.405	0.019	<0.005	<0.012	100.22
110071 OI	BT-09-32		129.00	40.144	<0.007	<0.006	0.009	14.511	0.218	0.030	0.251	45.356	0.011	<0.005	<0.012	100.21
110071 OI	BT-09-32		129.00	40.143	<0.007	<0.006	0.012	13.350	0.219	0.020	0.251	46.359	0.019	<0.005	<0.012	100.23
110071 OI	BT-09-32		129.00	40.013	<0.007	<0.006	0.023	13.350	0.219	0.020	0.251	46.359	0.019	<0.005	<0.012	100.30
110071 OI	BT-09-32		129.00	40.293	0.008	0.006	<0.008	12.904	0.203	0.028	0.253	46.344	0.022	<0.005	<0.012	100.07
110071 OI	BT-09-32		129.00	40.427	<0.007	<0.006	0.010	12.748	0.206	0.025	0.273	46.577	0.014	0.005	<0.012	100.29
110071 OI	BT-09-32		129.00	40.334	0.013	0.010	0.009	13.108	0.214	0.019	0.262	46.497	0.016	0.005	<0.012	100.49
110071 OI	BT-09-32		129.00	40.351	<0.007	<0.006	0.015	12.946	0.209	0.016	0.261	46.469	0.008	<0.005	<0.012	100.28
110071 OI	BT-09-32		129.00	40.158	<0.007	<0.006	0.008	12.983	0.194	0.037	0.247	46.427	0.016	<0.005	<0.012	100.07
110071 OI	BT-09-32		129.00	40.246	<0.007	<0.006	0.008	13.363	0.213	0.029	0.246	46.081	0.012	<0.005	<0.012	100.26
110071 OI	BT-09-32		129.00	39.871	<0.007	<0.006	0.020	14.230	0.218	0.016	0.246	45.525	0.022	<0.005	<0.012	100.65
110071 OI	BT-09-32		129.00	39.858	0.007	0.012	0.020	14.276	0.215	0.032	0.246	45.746	0.010	<0.005	<0.012	100.20
110071 OI	BT-09-32		129.00	39.871	<0.007	<0.006	0.008	19.379	0.225	0.021	0.258	45.746	0.010	<0.005	<0.012	100.56
110071 OI	BT-09-32		129.00	39.858	<0.007	<0.006	0.008	18.853	0.221	0.032	0.246	45.525	0.022	<0.005	<0.012	100.65
110071 OI	BT-09-32		129.00	38.726	<0.007	<0.006	0.008	16.662	0.222	0.026	0.221	40.619	<LLD	<0.005	<0.012	99.95
110071 OI	BT-09-32		129.00	38.820	0.008	<0.006	<0.008	19.852	0.221	0.032	0.246	45.746	0.010	<0.005	<0.012	99.96
110071 OI	BT-09-32		129.00	38.757	<0.007	<0.006	0.008	20.087	0.227	0.033	0.231	40.619	<LLD	<0.005	<0.012	100.34
110071 OI	BT-09-32		129.00	39.068	<0.007	<0.006	0.008	19.379	0.225	0.021	0.258	45.746	0.010	<0.005	<0.012	100.56
110071 OI	BT-09-32		129.00	38.726	<0.007	<0.006	0.008	18.853	0.221	0.032	0.246	45.525	0.022	<0.005	<0.012	99.95
110071 OI	BT-09-32		129.00	38.820	0.008	<0.006	<0.008	20.087	0.227	0.033	0.231	40.619	<LLD	<0.005	<0.012	100.34
110071 OI	BT-09-32		129.00	39.110	<0.007	<0.006	0.008	20.087	0.227	0.033	0.231	40.619	<LLD	<0.005	<0.012	100.34
110071 OI	BT-09-32		129.00	38.757	<0.007	<0.006	0.008	20.419	0.221	0.034	0.219	40.534	0.022	<0.005	<0.012	100.26
110071 OI	BT-09-32		129.00	38.844	<0.007	<0.006	0.008	20.281	0.268	0.034	0.214	40.533	0.022	<0.005	<0.012	100.50
110071 OI	BT-09-32		129.00	38.788	0.011	<0.006	0.008	20.140	0.277	0.022	0.228	40.533	0.022	<0.005	<0.012	100.32
110071 OI	BT-09-32		129.00	38.806	0.010	0.013	0.010	20.413	0.272	0.030	0.220	40.587	0.027	<0.005	<0.012	100.26
110071 OI	BT-09-32		129.00	38.739	<0.007	<0.006	0.008	20.088	0.264	0.028	0.227	40.476	0.030	<0.005	<0.012	99.88
110071 OI	BT-09-32		129.00	38.509	<0.007	<0.006	0.010	20.361	0.291	0.025	0.219	40.375	0.030	<0.005	<0.012	99.82
110071 OI	BT-09-32		129.00	38.819	<0.007	<0.006	0.005	20.109	0.284	0.032	0.220	40.338	0.018	<0.005	<0.012	100.43
110071 OI	BT-09-32		129.00	38.616	<0.007	<0.006	0.008	21.441	0.269	0.025	0.195	39.344	0.008	<0.005	<0.012	99.90
110071 OI	BT-09-32		129.00	38.701	0.008	<0.006	0.008	20.130	0.276	0.031	0.208	40.195	0.029	0.011	<0.012	99.59
110071 OI	BT-09-32		129.00	38.978	0.009	<0.006	0.008	20.186	0.263	0.027	0.200	40.569	0.020	<0.005	<0.012	100.29
110071 OI	BT-09-32		129.00	40.535	<0.007	0.013	0.018	11.657	0.175	0.028	0.267	47.687	0.026	<0.005	<0.012	100.41
110071 OI	BT-09-32		129.00	40.338	<0.007	0.013	<0.008	12.288	0.201	0.032	0.252	47.002	0.037	<0.005	<0.012	100.34
110071 OI	BT-09-32		129.00	40.311	<0.007	0.008	<0.008	12.374	0.190	0.027	0.250	47.068	0.021	<0.005	<0.012	100.13
110071 OI	BT-09-32		129.00	40.146	<0.007	<0.006	<0.008	11.689	0.179	0.015	0.255	47.682	0.030	<0.005	<0.012	99.85
110071 OI	BT-09-32		129.00	40.041	0.006	<0.006	0.025	10.842	0.157	<LLD	0.261	48.427	0.030	<0.005	<0.012	100.11
110071 OI	BT-09-32		129.00	40.568	<0.007	0.014	<0.008	14.486	0.186	<LLD	0.258	47.583	0.015	<0.005	<0.012	100.11
110071 OI	BT-09-32		129.00	39.455	<0.007	<0.006	<0.008	14.759	0.229	0.027	0.194	44.576	0.015	<0.005	<0.012	99.26
110071 OI	BT-09-32		129.00	38.685	0.008	0.005	<0.008	14.997	0.225	0.032	0.205	44.395	0.017	0.019	0.032	98.73
110071 OI	BT-09-32		129.00	38.475	<0.007	<0.006	0.007	14.771	0.221	0.030	0.216	44.565	0.019	<0.005	<0.012	99.63
110071 OI	BT-09-32		129.00	38.654	<0.007	<0.006	0.010	14.690	0.226	0.019	0.207	44.542	0.022	<0.005	<0.012	99.92
110071 OI	BT-09-32		129.00	38.730	<0.007	<0.006	0.011	14.642	0.225	0.024	0.211	44.513	0.026	<0.005	<0.012	99.87
110071 OI	BT-09-32		129.00	38.686	<0.007	<0.006	0.008	14.888	0.223	0.029	0.208	44.568	0.028	<0.005	<0.012	99.74
110071 OI	BT-09-32		129.00	38.750	<0.007	<0.006	0.008	14.888	0.223	0.029	0.208	44.568	0.028	<0.005	<0.012	99.74
110071 OI	BT-09-32		129.00	38.686	<0.007	<0.006	0.008	14.888	0.223	0.029	0.208	44.568	0.028	<0.005	<0.012	99.74
110071 OI	BT-09-32		129.00	38.686	<0.007	<0.006	0.008	14.888	0.223	0.029	0.208	44.568	0.028	<0.005	<0.012	99.74
110071 OI	BT-09-32		129.00	38.686	<0.007	<0.006	0.008	14.888	0.223	0.029	0.208	44.568	0.028	<0.005	<0.012	99.74
110071 OI	BT-09-32		129.00	38.686	<0.007	<0.006	0.008	14.888	0.223	0.029	0.208	44.568	0.028	<0.005	<0.012	99.74
110071 OI	BT-09-32		129.00	38.686	<0.007	<0.006										

Sample ID	Mineral	DDH	Depth(m)	SiO2	TI02	Al2O3	FeO(T)	MnO	MgO	CaO	SrO	Na2O	K2O	Total
Unit				wt %	wt %	wt %	wt %							
110194 PI		BT-11-177	97.00	47.932	0.035	32.572	0.273	<0.027	<0.029	16.082	<0.157	2.424	0.040	99.75
110194 PI		BT-11-177	97.00	47.297	<0.034	33.111	0.371	<0.027	<0.029	16.902	<0.157	2.347	0.036	99.78
110194 PI		BT-11-177	97.00	48.058	0.035	32.630	0.379	<0.027	<0.029	16.292	<0.157	2.472	0.029	99.80
110194 PI		BT-11-177	97.00	47.835	<0.034	32.738	0.431	<0.027	0.025	16.406	<0.157	2.279	0.060	99.59
110194 PI		BT-11-177	97.00	49.749	<0.034	31.479	0.276	<0.027	0.052	14.674	<0.157	2.897	0.428	99.64
110194 PI		BT-11-177	97.00	48.011	<0.034	32.466	0.410	0.030	0.031	16.245	<0.157	2.908	0.050	100.05
110194 PI		BT-11-177	97.00	47.755	<0.034	32.923	0.410	<0.027	0.034	16.725	<0.157	2.103	0.030	99.80
110194 PI		BT-11-177	97.00	46.357	<0.034	32.837	0.218	<0.027	<0.029	16.113	<0.157	2.533	<0.020	99.98
110194 PI		BT-11-177	97.00	49.055	<0.034	32.054	0.350	<0.027	0.053	15.590	<0.157	2.890	0.040	99.91
110194 PI		BT-11-177	97.00	48.854	<0.034	31.890	0.289	<0.027	<0.029	15.308	<0.157	2.831	0.074	99.23
110223 PI		BT-09-34	120.50	48.707	<0.034	32.159	0.364	<0.027	<0.029	15.384	<0.157	2.790	0.055	99.25
110223 PI		BT-09-34	120.50	47.582	<0.034	32.630	0.364	<0.027	0.033	16.281	<0.157	2.312	0.039	99.95
110223 PI		BT-09-34	120.50	46.179	<0.034	32.737	0.290	<0.027	0.025	16.332	<0.157	2.282	0.030	99.58
110223 PI		BT-09-34	120.50	47.725	<0.034	32.791	0.300	<0.027	<0.029	16.342	<0.157	2.328	0.050	99.78
110223 PI		BT-09-34	120.50	47.629	<0.034	32.278	0.281	<0.027	<0.029	15.873	<0.157	2.608	0.066	99.54
110223 PI		BT-09-34	120.50	49.351	<0.034	31.766	0.216	<0.027	<0.029	15.020	<0.157	3.115	<0.020	100.06
110223 PI		BT-09-34	120.50	48.630	<0.034	32.573	0.177	<0.027	<0.029	16.032	<0.157	2.606	<0.020	99.93
110223 PI		BT-09-34	120.50	47.518	<0.034	33.069	0.285	<0.027	<0.029	16.801	<0.157	2.451	0.025	99.90
110223 PI		BT-09-34	120.50	46.480	<0.034	32.536	0.244	<0.027	<0.029	16.053	<0.157	2.550	0.029	100.07
110223 PI		BT-09-34	120.50	48.380	<0.034	32.578	0.258	<0.027	<0.029	16.228	<0.157	2.489	0.031	100.25
110223 PI		BT-09-34	120.50	48.217	<0.034	32.833	0.310	0.027	<0.029	16.312	<0.157	2.363	0.042	99.80
110223 PI		BT-09-34	120.50	48.055	<0.034	32.576	0.323	0.027	<0.029	16.360	<0.157	2.362	0.033	99.91
110223 PI		BT-09-34	120.50	47.142	<0.034	32.458	0.156	<0.027	<0.029	17.152	<0.157	1.956	<0.020	99.80
110069 PI		BT-09-98	403.40	47.983	<0.034	32.918	0.209	<0.027	0.066	16.248	<0.157	2.306	<0.020	100.03
110069 PI		BT-09-98	403.40	47.373	<0.034	33.404	0.170	<0.027	0.028	16.936	<0.157	1.868	0.028	99.72
110069 PI		BT-09-98	403.40	46.734	<0.034	33.649	0.121	<0.027	<0.029	17.306	<0.157	1.822	<0.020	99.52
110069 PI		BT-09-98	403.40	47.098	<0.034	33.331	0.057	<0.027	<0.029	17.031	<0.157	1.942	<0.020	99.33
110069 PI		BT-09-98	403.40	46.424	<0.034	33.514	0.262	<0.027	0.048	17.276	<0.157	1.750	0.043	99.36
110069 PI		BT-09-98	403.40	46.906	<0.034	33.382	0.183	<0.027	<0.029	16.964	<0.157	1.864	0.029	100.07
110069 PI		BT-09-98	403.40	47.513	0.046	33.356	0.202	<0.027	<0.029	16.774	<0.157	2.071	<0.020	99.81
110069 PI		BT-09-98	403.40	46.649	<0.034	33.616	0.168	<0.027	<0.029	17.545	<0.157	1.715	0.029	100.01
110069 PI		BT-09-98	403.40	47.339	<0.034	33.478	0.138	<0.027	<0.029	17.031	<0.157	1.956	<0.020	99.82
110069 PI		BT-09-98	403.40	46.132	<0.034	32.679	0.191	<0.027	<0.029	16.392	<0.157	2.355	0.025	99.64
110069 PI		BT-09-98	403.40	46.704	<0.034	33.693	0.148	<0.027	<0.029	17.184	<0.157	1.805	<0.020	99.53

Sample ID	Mineral	DDH	Depth(m)	SiO2	TI02	Al2O3	FeO(T)	MnO	MgO	CaO	SrO	Na2O	K2O	Total
Unit				wt %	wt %	wt %	wt %	wt %	wt %	wt %	wt %	wt %	wt %	wt %
	Standards:													
	alBF			86.527	0.014	19.603	0.000	0.000	0.000	0.104	0.000	11.870	0.099	100.22
	alBF			88.959	0.008	19.626	0.000	0.000	0.000	0.082	0.000	11.811	0.076	100.56
	Alb			68.784	0.006	19.541	0.005	0.008	0.000	0.094	0.000	11.839	0.089	100.37
	alBF			68.516	0.004	19.481	0.008	0.000	0.001	0.086	0.000	11.763	0.090	99.95
	Alb			68.613	0.016	19.509	0.000	0.000	0.002	0.055	0.028	11.751	0.077	100.05
	alBF			68.705	0.003	19.525	0.032	0.000	0.000	0.076	0.035	11.736	0.080	100.19
	ansMT			44.09	0.014	34.788	0.458	0.001	0.038	19.405	0.000	0.546	0.012	99.35
	ansMT			44.014	0.000	34.887	0.458	0.007	0.050	19.134	0.067	0.529	0.017	99.14
	ansMT			64.124	0.000	35.030	0.455	0.000	0.050	19.406	0.067	0.539	0.009	99.68
	Or-1			64.57	0.000	18.284	0.000	0.000	0.003	0.000	0.000	1.066	15.324	99.25
	Or-1			64.428	0.000	18.382	0.000	0.004	0.000	0.012	0.040	1.084	15.280	98.23
	Or-1			64.357	0.000	18.326	0.008	0.000	0.000	0.008	0.000	1.063	15.289	98.03
	Accuracy:													
	Standard													
	Average wt%			alBF		alBF		alBF		alBF		alBF		Or-1
	Expected wt%*			68.684	LOD	19.548	LOD	LOD	LOD	0.083	LOD	11.795	15.291	
	Accuracy % rel.			68.74	n.d.	19.440	n.d.	n.d.	n.d.	n.d.	n.d.	11.820	15.120	
	Precision % rel.			-0.0815	n.d.	0.553	n.d.	n.d.	n.d.	n.d.	n.d.	-0.21	1.13	
	Standard Dev.			0.1170	0.0054	0.056	0.0125	0.0037	0.0008	0.0168	0.0164	0.0534	0.0291	
	Perscion % rel.			0.002	n.d.	0.0029	n.d.	n.d.	n.d.	n.d.	n.d.	0.0045	0.0019	

Sample ID	Mineral	DDH	Depth(m)	SiO2	TiO2	Al2O3	Cr2O3	FeO(T)	MnO	CoO	NiO	MgO	CaO	Na2O	K2O	Total
Limit				wt. %	wt. %	wt. %	wt. %	wt. %	wt. %	wt. %	wt. %	wt. %				
110023 CPX	BT-09-34	120.50	51.917	0.032	0.007	0.156	0.035	1.104	0.028	0.012	0.012	0.019	17.219	0.842	0.336	99.55
110023 CPX	BT-09-34	120.50	52.459	0.287	0.240	0.980	0.530	5.530	0.147	<0.012	0.021	16.464	21.073	0.373	<0.005	100.12
110023 CPX	BT-09-34	120.50	52.211	0.116	0.303	1.133	1.154	5.271	0.163	<0.012	0.019	16.406	21.210	0.371	<0.005	100.05
110023 CPX	BT-09-34	120.50	51.866	0.108	0.272	1.133	1.133	5.249	0.158	<0.012	0.019	16.215	21.345	0.413	0.007	99.74
110023 CPX	BT-09-34	120.50	51.966	0.269	0.308	0.957	0.549	0.170	<0.012	0.009	16.280	21.355	0.374	<0.005	99.31	
110023 CPX	BT-09-34	120.50	51.452	0.129	0.314	1.124	1.124	5.152	0.166	<0.012	0.013	16.407	21.419	0.346	<0.005	99.31
110023 CPX	BT-09-34	120.50	51.960	0.129	0.302	1.078	1.078	5.393	0.168	<0.012	0.015	16.111	21.469	0.380	<0.005	99.31
110023 CPX	BT-09-34	120.50	52.252	0.124	0.321	1.132	1.132	5.321	0.157	<0.012	0.017	16.311	21.619	0.374	<0.005	100.21
110023 CPX	BT-09-34	120.50	52.073	0.106	0.329	1.104	1.104	5.222	0.165	<0.012	0.020	16.163	21.969	0.363	<0.005	99.57
110023 CPX	BT-09-34	120.50	52.046	0.161	0.357	1.098	1.098	5.166	<0.012	0.010	15.628	21.825	0.377	<0.005	99.98	
110037 CPX	BT-11-199A	46.20	52.928	0.118	0.215	1.101	1.101	3.448	0.113	<0.012	0.034	17.566	21.719	0.352	<0.005	99.62
110037 CPX	BT-11-199A	46.20	52.551	0.104	0.286	1.071	1.071	3.883	0.106	<0.012	0.041	16.340	22.330	0.450	<0.005	99.99
110068 CPX	BT-09-98	403.40	52.900	0.144	0.290	1.150	1.150	3.954	0.131	<0.012	0.030	16.424	22.324	0.391	<0.005	99.64
110068 CPX	BT-09-98	403.40	52.242	0.135	0.282	1.167	1.167	4.293	0.139	<0.012	0.037	16.244	22.221	0.416	<0.005	99.02
110068 CPX	BT-09-98	403.40	49.961	0.343	0.251	0.861	0.861	4.923	0.146	<0.015	0.036	15.964	22.224	0.391	<0.005	99.81
110068 CPX	BT-09-98	403.40	52.153	0.226	0.312	1.234	1.234	4.227	0.130	<0.012	0.033	15.934	22.323	0.416	<0.005	99.81
110068 CPX	BT-09-98	403.40	51.804	0.259	0.278	1.102	1.102	4.371	0.144	<0.012	0.036	16.135	22.349	0.378	<0.005	99.08
110068 CPX	BT-09-98	403.40	52.034	0.147	0.274	1.110	1.110	4.459	0.146	<0.012	0.040	16.035	22.384	0.322	<0.005	99.76
110068 CPX	BT-09-98	403.40	52.037	0.368	0.266	0.488	0.488	4.351	0.146	<0.012	0.028	16.281	22.394	0.322	<0.005	99.56
110071 CPX	BT-09-32	129.00	51.721	0.384	0.273	0.658	0.658	4.468	0.145	<0.012	0.030	16.383	22.412	0.324	<0.005	99.53
110071 CPX	BT-09-32	129.00	51.731	0.383	0.294	0.658	0.658	4.452	0.158	<0.012	0.033	16.346	22.237	0.324	<0.005	99.74
110071 CPX	BT-09-32	129.00	52.365	0.304	0.292	0.843	0.843	4.489	0.129	<0.012	0.033	16.953	22.678	0.333	<0.005	100.00
110100 CPX	BT-11-180	171.00	44.083	1.856	1.226	1.181	1.181	8.101	0.080	<0.012	0.061	15.978	11.952	2.198	0.820	97.54
110100 CPX	BT-11-180	171.00	52.620	0.316	0.266	0.759	0.759	5.973	0.159	<0.012	0.030	17.114	20.248	0.354	<0.005	99.97
110100 CPX	BT-11-180	171.00	51.965	0.281	0.286	0.784	0.784	5.832	0.185	<0.012	0.038	16.345	20.778	0.368	<0.010	99.19
110100 CPX	BT-11-180	171.00	52.335	0.242	0.276	0.889	0.889	5.631	0.165	<0.013	0.041	16.890	22.119	0.374	<0.005	100.01
110100 CPX	BT-11-180	171.00	52.019	0.236	0.282	0.859	0.859	5.656	0.171	<0.012	0.032	15.890	22.028	0.388	<0.005	99.88
110100 CPX	BT-11-180	171.00	53.257	0.201	0.207	0.637	0.637	5.613	0.173	<0.013	0.033	16.132	22.962	0.225	<0.005	100.16
110100 CPX	BT-11-180	171.00	53.257	0.236	0.279	1.088	1.088	4.931	0.148	<0.012	0.036	20.268	16.883	0.286	<0.005	99.87
110166 CPX	BT-09-98	249.55	52.780	0.236	0.279	1.088	1.088	4.931	0.148	<0.012	0.036	20.268	16.883	0.286	<0.005	99.87
110166 CPX	BT-09-98	249.55	52.538	0.236	0.279	1.088	1.088	4.931	0.148	<0.012	0.036	20.268	16.883	0.286	<0.005	99.87
110166 CPX	BT-09-98	249.55	52.765	0.326	0.266	1.001	1.001	4.346	0.142	<0.013	0.030	18.419	19.489	0.311	<0.005	99.80
110166 CPX	BT-09-98	249.55	52.479	0.245	0.288	1.113	1.113	4.431	0.147	<0.012	0.031	17.302	20.668	0.338	<0.005	99.66
110166 CPX	BT-09-98	249.55	51.900	0.275	0.308	1.117	1.117	4.501	0.151	<0.012	0.029	17.071	21.182	0.351	<0.005	99.67
110166 CPX	BT-09-98	249.55	52.720	0.430	0.218	0.981	0.981	4.199	0.146	<0.012	0.032	17.345	21.449	0.338	<0.005	100.06
110166 CPX	BT-09-98	249.55	52.342	0.252	0.263	0.468	0.468	5.098	0.147	<0.012	0.020	16.389	21.725	0.250	<0.005	99.25
110166 CPX	BT-09-98	249.55	52.572	0.281	0.263	1.035	1.035	4.108	0.145	<0.012	0.029	16.889	21.902	0.366	<0.005	100.00
110166 CPX	BT-09-98	249.55	52.579	0.239	0.234	0.693	0.693	4.456	0.134	<0.012	0.023	16.732	22.961	0.257	<0.005	99.85
110166 CPX	BT-09-98	249.55	52.865	0.160	0.220	0.372	0.372	4.499	0.144	<0.012	0.021	16.388	22.789	0.236	<0.005	99.72
110194 CPX	BT-11-177	97.00	55.291	0.177	0.213	0.855	0.855	4.349	0.113	<0.015	0.024	21.577	12.062	0.655	0.027	97.33
110194 CPX	BT-11-177	97.00	55.129	0.138	0.231	0.951	0.951	4.111	0.118	<0.012	0.034	21.822	12.085	0.653	0.025	97.33
110194 CPX	BT-11-177	97.00	51.872	0.204	0.286	0.959	0.959	5.829	0.175	<0.012	0.035	16.866	20.264	0.298	<0.005	99.39
110194 CPX	BT-11-177	97.00	51.688	0.227	0.291	0.950	0.950	5.261	0.162	<0.012	0.036	16.381	21.441	0.307	<0.005	99.25
110194 CPX	BT-11-177	97.00	51.837	0.196	0.210	0.941	0.941	5.338	0.173	<0.012	0.023	16.233	21.719	0.310	<0.005	99.59
110196 CPX	BT-11-177	107.60	52.242	0.228	0.222	1.037	1.037	5.565	0.169	<0.012	0.024	16.600	21.119	0.272	<0.005	99.38
110196 CPX	BT-11-177	107.60	51.949	0.231	0.276	0.927	0.927	4.921	0.142	<0.012	0.025	16.630	21.441	0.285	<0.005	99.37
110196 CPX	BT-11-177	107.60	51.775	0.204	0.243	1.075	1.075	5.140	0.168	<0.012	0.025	16.388	21.516	0.304	<0.005	99.54
110380 CPX	BT-11-179	86.70	52.774	0.222	0.268	1.048	1.048	4.569	0.158	<0.012	0.020	16.791	21.949	0.304	<0.005	100.05
110380 CPX	BT-11-179	86.70	52.774	0.222	0.268	1.048	1.048	4.569	0.158	<0.012	0.020	16.791	21.949	0.304	<0.005	100.05
110380 CPX	BT-11-179	86.70	52.559	0.179	0.261	1.076	1.076	4.238	0.131	<0.012	0.033	16.807	21.884	0.428	<0.005	99.85
110380 CPX	BT-11-179	86.70	52.708	0.223	0.268	1.094	1.094	4.160	0.146	<0.012	0.031	16.386	22.485	0.408	<0.005	100.12
110380 CPX	BT-11-179	86.70	53.417	0.135	1.909	0.677	0.677	3.950	0.131	<0.012	0.022	16.711	18.826	0.492	<0.005	99.59

Sample ID	Mineral	DDH	Depth(m)	SiO2	TiO2	Al2O3	Cr2O3	FeO(T)	MnO	CoO	NiO	MgO	CaO	Na2O	K2O	Total
Limit				wt. %	wt. %	wt. %	wt. %	wt. %	wt. %	wt. %	wt. %	wt. %	wt. %	wt. %	wt. %	wt. %
Standards:																
diopAST Cpx				55.163	0.064	0.082	0.000	0.067	0.047	0.000	0.000	18.483	26.088	0.005	0.000	99.98
diopAST Cpx				55.177	0.064	0.084	0.000	0.054	0.045	0.000	0.000	18.528	25.978	0.004	0.000	99.94
diopAST Cpx				55.185	0.063	0.086	0.000	0.040	0.040	0.001	0.004	18.589	25.832	0.008	0.000	99.83
diopAST Cpx				55.243	0.064	0.081	0.004	0.077	0.043	0.001	0.000	18.650	26.059	0.009	0.000	100.23
diopAST Cpx				55.389	0.061	0.088	0.004	0.065	0.046	0.000	0.000	18.601	26.020	0.008	0.001	100.27
diopAST Cpx				55.401	0.067	0.077	0.001	0.053	0.030	0.016	0.001	18.581	26.272	0.008	0.000	100.49
diopAST Cpx				55.406	0.063	0.074	0.000	0.065	0.038	0.000	0.000	18.589	26.070	0.007	0.000	100.30
diopAST Cpx				55.468	0.063	0.072	0.000	0.067	0.050	0.000	0.000	18.536	26.030	0.007	0.000	100.32
diopAST Cpx				55.500	0.075	0.085	0.000	0.049	0.032	0.004	0.008	18.516	26.007	0.007	0.000	100.35
diopAST Cpx				55.609	0.065	0.084	0.002	0.037	0.043	0.000	0.009	18.564	26.250	0.007	0.000	100.76
diopAST Cpx				55.699	0.065	0.070	0.001	0.057	0.057	0.000	0.009	18.564	26.250	0.005	0.000	100.76
diopAST Cpx				50.146	0.473	7.674	0.887	4.682	0.124</							

Sample ID	Lithology	DDH	Depth(m)	Ga	Sr	Y	Ba	Zr	Nb	Mo	Hf	Ta	W	Ti	Pb	Th	U	Cd	Li	In	Sn	Sb	Rb	Cs	Bi	La	Ce	Pr	Nd	Sm	Eu	Gd	Tb	Dy	Ho	Er	Tm	Yb		
Unit			ppm	ppm	ppm	ppm	ppm	ppm	ppm	ppm	ppm	ppm	ppm	ppm	ppm	ppm	ppm	ppm	ppm	ppm	ppm	ppm	ppm	ppm	ppm	ppm	ppm	ppm	ppm	ppm	ppm	ppm	ppm	ppm	ppm	ppm	ppm	ppm	ppm	ppm
Method			MC-100	MC-100	MC-100	MC-100	MC-100	MC-100	MC-100	MC-100	MC-100	MC-100	MC-100	MC-100	MC-100	MC-100	MC-100	MC-100	MC-100	MC-100	MC-100	MC-100	MC-100	MC-100	MC-100	MC-100	MC-100	MC-100	MC-100	MC-100	MC-100	MC-100	MC-100	MC-100	MC-100	MC-100	MC-100	MC-100	MC-100	
Detection Limit			0.04	0.6	0.05	0.8	6	0.028	0.08	0.14	0.007	0.05	0.002	0.18	0.018	0.021	0.013	0.4	0.0018	0.0018	0.16	0.04	0.11	0.013	0.47	0.1	0.12	0.014	0.06	0.026	0.0031	0.009	0.023	0.008	0.0028	0.0045	0.012	0.038	0.05	0.035
110198	Black Label Chromite	BT-11-177	145.5	34.340	4.900	1.250	6.300	7.000	0.376	0.610	0.170	0.008	0.354	0.010	0.600	0.056	0.020	0.017	10.100	0.032	-0.2	0.200	1.900	0.363	-0.5	0.750	1.900	0.102	0.480	0.121	0.047	0.047	0.031	0.203	0.048	0.142	0.023	0.195		
110005	Black Label Chromite	BT-08-25	63.8	21.580	3.000	3.700	5.200	11.000	0.419	0.310	0.017	0.050	0.510	0.002	1.600	0.027	0.020	0.027	4.800	0.028	-0.2	0.500	0.950	0.019	-0.5	0.800	1.400	0.241	0.290	0.449	0.192	0.059	0.109	0.078	0.112	0.383	0.026	0.385		
110287	Black Label Chromite	BT-08-07	153.3	32.870	8.300	4.200	1.700	-6	0.246	0.650	0.230	-0.01	0.210	0.002	2.400	0.027	0.013	0.042	5.800	0.018	-0.2	0.940	1.130	0.082	-0.5	0.250	0.400	0.251	0.260	0.449	0.182	0.069	0.109	0.072	0.142	0.462	0.065	0.403		
110097	Black Label Chromite	BT-11-199A	46.2	25.730	3.500	0.700	2.500	-6	0.231	0.620	0.210	0.007	0.050	0.005	2.200	0.025	0.012	-0.01	4.900	0.016	-0.2	0.700	0.860	0.050	-0.5	0.450	0.500	0.050	0.280	0.086	0.026	0.132	0.074	0.037	0.170	0.031	0.129	0.088		
110197	Black Label Chromite	BT-08-07	141.4	22.370	3.500	1.100	2.400	-6	0.239	0.620	0.210	0.007	0.050	0.005	2.200	0.025	0.012	-0.01	4.900	0.016	-0.2	0.700	0.860	0.050	-0.5	0.450	0.500	0.050	0.280	0.086	0.026	0.132	0.074	0.037	0.170	0.031	0.129	0.088	0.088	
110095	Black Label Chromite	BT-08-07	253.7	20.640	17.000	3.280	14.900	8.000	0.338	0.920	0.150	0.008	0.080	0.025	7.200	0.035	0.012	-0.01	8.500	0.028	-0.2	1.100	1.400	0.168	-0.5	0.300	0.340	0.178	0.560	0.314	0.098	0.142	0.025	0.075	0.530	0.117	0.350	0.050	0.316	
110211	BLZ Ch#r Hazbuqite	BT-08-32	216.5	6.510	4.900	1.740	4.100	6.000	0.199	0.870	0.250	-0.01	0.134	0.004	2.600	-0.027	0.025	0.023	6.400	0.035	-0.2	0.130	2.100	0.088	-0.5	0.670	1.200	0.333	0.660	0.525	0.241	0.075	0.254	0.144	0.064	0.156	0.537	0.028	0.198	
110211	BLZ Ch#r Hazbuqite	BT-08-32	276	22.520	11.000	1.820	14.000	-6	0.201	0.630	-0.1	-0.01	0.031	0.031	5.100	0.038	0.028	0.028	4.700	0.033	-0.2	0.940	1.160	0.058	-0.5	0.580	1.110	0.142	0.600	0.133	0.047	0.181	0.051	0.274	0.069	0.214	0.039	0.266		
110264	BLZ Ch#r Hazbuqite	BT-11-182	174.5	17.870	4.800	2.310	6.900	-6	0.176	0.370	-0.1	-0.01	-0.1	0.134	6.100	0.027	0.044	0.034	4.500	0.031	-0.2	0.900	1.150	0.094	-0.5	0.800	1.400	0.162	0.680	0.264	0.064	0.283	0.050	0.338	0.072	0.230	0.039	0.230		
110093	BLZ Ch#r Hazbuqite	BT-08-34	60.7	11.800	8.300	1.090	3.100	-6	0.222	0.740	-0.1	-0.01	0.210	0.105	3.700	0.037	0.035	0.019	3.900	0.054	-0.2	0.950	1.190	0.257	-0.5	0.800	1.400	0.162	0.680	0.264	0.064	0.283	0.050	0.338	0.072	0.230	0.039	0.230		
110199	BLZ Ch#r Hazbuqite	BT-08-34	96.3	14.530	3.900	1.090	3.100	-6	0.222	0.740	-0.1	-0.01	0.210	0.105	3.700	0.037	0.035	0.019	3.900	0.054	-0.2	0.950	1.190	0.257	-0.5	0.800	1.400	0.162	0.680	0.264	0.064	0.283	0.050	0.338	0.072	0.230	0.039	0.230		
110199	BLZ Ch#r Hazbuqite	BT-08-34	60.7	11.800	8.300	1.090	3.100	-6	0.222	0.740	-0.1	-0.01	0.210	0.105	3.700	0.037	0.035	0.019	3.900	0.054	-0.2	0.950	1.190	0.257	-0.5	0.800	1.400	0.162	0.680	0.264	0.064	0.283	0.050	0.338	0.072	0.230	0.039	0.230		
110199	BLZ Ch#r Hazbuqite	BT-08-34	60.7	11.800	8.300	1.090	3.100	-6	0.222	0.740	-0.1	-0.01	0.210	0.105	3.700	0.037	0.035	0.019	3.900	0.054	-0.2	0.950	1.190	0.257	-0.5	0.800	1.400	0.162	0.680	0.264	0.064	0.283	0.050	0.338	0.072	0.230	0.039	0.230		
110199	BLZ Ch#r Hazbuqite	BT-08-34	60.7	11.800	8.300	1.090	3.100	-6	0.222	0.740	-0.1	-0.01	0.210	0.105	3.700	0.037	0.035	0.019	3.900	0.054	-0.2	0.950	1.190	0.257	-0.5	0.800	1.400	0.162	0.680	0.264	0.064	0.283	0.050	0.338	0.072	0.230	0.039	0.230		
110199	BLZ Ch#r Hazbuqite	BT-08-34	60.7	11.800	8.300	1.090	3.100	-6	0.222	0.740	-0.1	-0.01	0.210	0.105	3.700	0.037	0.035	0.019	3.900	0.054	-0.2	0.950	1.190	0.257	-0.5	0.800	1.400	0.162	0.680	0.264	0.064	0.283	0.050	0.338	0.072	0.230	0.039	0.230		
110199	BLZ Ch#r Hazbuqite	BT-08-34	60.7	11.800	8.300	1.090	3.100	-6	0.222	0.740	-0.1	-0.01	0.210	0.105	3.700	0.037	0.035	0.019	3.900	0.054	-0.2	0.950	1.190	0.257	-0.5	0.800	1.400	0.162	0.680	0.264	0.064	0.283	0.050	0.338	0.072	0.230	0.039	0.230		
110199	BLZ Ch#r Hazbuqite	BT-08-34	60.7	11.800	8.300	1.090	3.100	-6	0.222	0.740	-0.1	-0.01	0.210	0.105	3.700	0.037	0.035	0.019	3.900	0.054	-0.2	0.950	1.190	0.257	-0.5	0.800	1.400	0.162	0.680	0.264	0.064	0.283	0.050	0.338	0.072	0.230	0.039	0.230		
110199	BLZ Ch#r Hazbuqite	BT-08-34	60.7	11.800	8.300	1.090	3.100	-6	0.222	0.740	-0.1	-0.01	0.210	0.105	3.700	0.037	0.035	0.019	3.900	0.054	-0.2	0.950	1.190	0.257	-0.5	0.800	1.400	0.162	0.680	0.264	0.064	0.283	0.050	0.338	0.072	0.230	0.039	0.230		
110199	BLZ Ch#r Hazbuqite	BT-08-34	60.7	11.800	8.300	1.090	3.100	-6	0.222	0.740	-0.1	-0.01	0.210	0.105	3.700	0.037	0.035	0.019	3.900	0.054	-0.2	0.950	1.190	0.257	-0.5	0.800	1.400	0.162	0.680	0.264	0.064	0.283	0.050	0.338	0.072	0.230	0.039	0.230		
110199	BLZ Ch#r Hazbuqite	BT-08-34	60.7	11.800	8.300	1.090	3.100	-6	0.222	0.740	-0.1	-0.01	0.210	0.105	3.700	0.037	0.035	0.019	3.900	0.054	-0.2	0.950	1.190	0.257	-0.5	0.800	1.400	0.162	0.680	0.264	0.064	0.283	0.050	0.338	0.072	0.230	0.039	0.230		
110199	BLZ Ch#r Hazbuqite	BT-08-34	60.7	11.800	8.300	1.090	3.100	-6	0.222	0.740	-0.1	-0.01	0.210	0.105	3.700	0.037	0.035	0.019	3.900	0.054	-0.2	0.950	1.190	0.257	-0.5	0.800	1.400	0.162	0.680	0.264	0.064	0.283	0.050	0.338	0.072	0.230	0.039	0.230		
110199	BLZ Ch#r Hazbuqite	BT-08-34	60.7	11.800	8.300	1.090	3.100	-6	0.222	0.740	-0.1	-0.01	0.210	0.105	3.700	0.037	0.035	0.019	3.900	0.054	-0.2	0.950	1.190	0.257	-0.5	0.800	1.400	0.162	0.680	0.264	0.064	0.283	0.050	0.338	0.072	0.230	0.039	0.230		
110199	BLZ Ch#r Hazbuqite	BT-08-34	60.7	11.800	8.300	1.090	3.100	-6	0.222	0.740	-0.1	-0.01	0.210	0.105	3.700	0.037	0.035	0.019	3.900	0.054	-0.2	0.950	1.190	0.257	-0.5	0.800	1.400	0.162	0.680	0.264	0.064	0.283	0.050	0.338	0.072	0.230	0.039	0.230		
110199	BLZ Ch#r Hazbuqite	BT-08-34	60.7	11.800	8.300	1.090	3.100	-6	0.222	0.740	-0.1	-0.01	0.210	0.105	3.700	0.037	0.035	0.019	3.900	0.054	-0.2	0.950	1.190	0.257	-0.5	0.800	1.400	0.162	0.680	0.264	0.064	0.283	0.050	0.338	0.072	0.230	0.039	0.230		
110199	BLZ Ch#r Hazbuqite	BT-08-34	60.7	11.800	8.300	1.090	3.100	-6	0.222	0.740	-0.1	-0.01	0.210	0.105	3.700	0.037	0.035	0.019	3.900	0.054	-0.2	0.950	1.190	0.257	-0.5	0.800	1.400	0.162	0.680	0.264	0.064	0.283	0.050	0.338	0.072	0.230	0.039	0.230		
110199	BLZ Ch#r Hazbuq																																							